Title

Neural representation of navigation in multi-species and solo environments in Egyptian fruit bats

Author

Snyder, Madeleine

Publication Date

2024

Peer reviewed|Thesis/dissertation

Neural Representation of Navigation in Multi-Species and Solo Environments in Egyptian Fruit Bats

by

Madeleine Corbett Snyder

A thesis submitted in partial satisfaction of the

requirements for the degree of

Joint Doctor of Philosophy

with The University of California, San Francisco

in

Bioengineering

in the

Graduate Division

of the

University of California, Berkeley

Committee in charge:

Professor Michael Yartsev, Chair

Professor Loren Frank

Professor Doris Tsao

Professor Joni Wallis

Summer 2024

Abstract

Neural Representation of Navigation in Multi-Species and Solo Environments in Egyptian Fruit Bats

by

Madeleine Corbett Snyder

Joint Doctor of Philosophy
with The University of California, San Francisco in Bioengineering

University of California, Berkeley

Professor Michael Yartsev, Chair

Many species negotiate complex spatial environments alongside other individuals and display the capacity to recall rewarding and costly locations. Prodigious navigators like the Egyptian fruit bats forage for food in convoluted aerial spaces and must account for the choices of other flying conspecifics to reach reward locations. We can simulate this challenging feat in the lab environment while using high-speed positional tracking and neural recording methods to investigate how bats solve this high-dimensional multi-agent foraging problem. However, in the lab the multi-agent foraging problem has a latent extra player: the human experimenter. While most studies involving a spatial reward task ignore the presence of the human in reporting and controls, we sought to explicitly include the experimenter in the task paradigm to test whether there is an appreciable effect of human presence on ongoing neural signal.

The first section of this thesis explores the neural representation of the human experimenter during a multi-agent foraging task. We find that a substantial amount of variance in the code for allocentric spatial representation can be accounted for simply by controlling for the identity of the human the bat lands on. This study shows, for the first time, that non-conspecifics are encoded in the canonical place cell code for spatial position. On a practical level, these findings serve as a cautionary tale to encourage future studies to limit the uncontrolled effects of human presence and intervention in behavioral neuroscience tasks.

The second section of this thesis strips down the complex foraging problem to its simplest form to study the stability of the neural code that supports flight in a familiar foraging environment. We find that, across days, the code for flight is largely stable and apparent variance may be accounted for simply by behavioral drift, not changes in the underlying neural code.

The thesis concludes with caveats of the current research, possibilities for future investigation, and avenues for combining modeling work with cross-species representation in the environment.

Dedication

To my chosen family, friends, and labmates: it takes a village and I am so grateful for your support and love.

Table of Contents

Acknowledgements

First and foremost, thank you Michael for your relentless optimism in pursuit of scientific questions. I am deeply grateful for your dynamic mentorship that enabled me to grow as a scientist in ways I did not imagine I would. Thank you for building a lab of scientifically exuberant people, all of whom make hard projects possible and collaborations easy. In particular but in no particular order, I'd like to thank Yuka for making it look trivial to manage such a dynamic and boisterous group of people; Kevin for being the sublime Experimenter #1—one of the kindest and brightest scientists I could ever hope to grow with as a graduate student; Boaz and Yuheng for their courageous spirit, absolute dedication to the practice of hard science, and terrible jokes; Angelo for being an incredible mentor and collaborator, and demonstrating that Italian design leads to meticulous science; Julie for leading by example as one of the kindest, most honest, rigorous, statistically competent and persistent scientists I have met; Tobias for teaching me literal brain surgery and leaving big shoes to fill; and Will for the hundreds of miles and lessons in fleet management. Thank you Logan for the energy you bring to lab and your combination of kindness, snark, and scientific curiosity—I hope there is a universe in which we are colleagues; thank you John for help with my flailing questions and thank you RAM for the hugs in times of need. Thank you Barbara, Alberta, Mareesa, and Sanjana for your hard work, commitment, and the joy that you bring to lab. Thank you to Drs Michael Arcaro and Marge Livingstone, without whom I would not have entered the world of research, and Dr Sam Gershman for encouraging my curiosity and directionless torrent of scientific ideas. Thank you Drs Mike Hasselmo and Chantal Stern for being role models of kind and multidimensional neuroscientists, and Simone for the photoshop skills that have carried me through my artistic endeavors in grad school. Thank you to Mr. Dunn for making me believe that consistency is key, and Camille and Jessamyn for the many miles and love that has lasted 20-some years. Thank you Willa and Madeline for being my rocks, partners in crime, and voices of reason. Thank you Rae, Justin, and Pat for being incredibly lovely housemates and bearing with me as I eat tortillas and butter over the stovetop at 10pm. Thank you Chris for the many years, many projects, love, and patience. And finally, thank you to my parents, who provided me with every opportunity to succeed and encouraged my curiosity and idiosyncrasies along the way.

Lastly, I'd like to acknowledge the bats that made this science possible.

Chapter 1: Introduction

1.1 Motivation

Animals must find and recall both resource-rich and costly locations in their environment to survive. Tolman theorized that the brain supports these behaviors by constructing a cognitive map of the environment[1]. The hippocampus and supporting neural structures, such as medial entorhinal cortex, have been proposed as the site of this cognitive map, and empirical evidence supports its role in coding the allocentric location of the animal[2,3]. The goal of investigating how the hippocampus represents the environment is to uncover the neural mechanisms that support this representation and formalize a complete model of navigation. Competing findings in the hippocampal literature have produced a complex landscape of models, and it is crucial to examine potential sources of discrepancy between studies to make progress towards a unified model. It is critical to acknowledge that the ecological niche of the animal is inextricably tied to the neural code that supports behavior, and as such, an ethological approach to behavioral neuroscience can further refine the interpretation of empirical findings of how the hippocampus represents the environment.

What follows in this thesis are two studies that leveraged spontaneous flight behavior in multi-agent and solo environments to examine the neural code in hippocampus that underlies a spatial navigation task. Each study explicitly investigated how a standard practice in the spatial behavior literature may lead to illusory instability in the hippocampal code. The first investigated the effects of human experimenter presence and behavior on spatial representation and found that a large fraction of hippocampal neurons modulated their firing around takeoff and landing depending on the identity of the human experimenter at the landing location. This study shows that the neural code for space includes information about the experimenter's location, behavior, and identity, and provides impetus to eliminate uncontrolled effects of experimenters in future behavioral neuroscience studies. The second project leveraged single photon calcium imaging to record the same neurons across many days and examined stability of place fields while the bats executed spontaneous and repeated flight motifs. This study found that the hippocampal code for space during solo navigation for reward is stable across days when controlling precisely for behavior, but illusory instability appears if behavioral drift of a flight path is not accounted for. Together, these studies demonstrate the importance of accounting for sources of variance that are baked into common task paradigms in behavioral neuroscience.

1.2 Neural activity reflects the presence and behavior of human experimenters

Human experimenters are ubiquitous in behavioral neuroscience. They control the structure and progress of the experimental paradigm, operate equipment to collect neural and behavioral data, and often administer reward to the animal performing the task. Despite the close spatiotemporal coupling of experimenter and recording animal behavior, there is little to no reporting or controls on human behavior. Implicitly, this suggests that the human has no appreciable effect on the neural data that may skew interpretation of results. However, anecdotally, many researchers

report that familiarity with their subject animals and consistent husbandry increases performance in behavioral testing and minimizes animal stress. A study on familiarity between rats and handlers confirmed this, as did a study examining preference of rats for unfamiliar versus familiar caretakers[4,5]. Further studies on the effects of female versus male experimenters found that latent neural activity and pain response behavior differed depending on whether a male or female administered a rapid-onset depressant[6–8]. Most recently, it was found that rats handled by fear-conditioned experimenters had greater expression of c-Fos in their amygdalae than rats handled by non-conditioned experimenters[9]. Together, these studies provide substantial evidence that the human experimenter has immediate and latent effects on the neural signal.

The primary goal of this project was to explicitly test whether ongoing neural activity reflects the presence or behavior of the human experimenter during a simple spatial reward task. Additionally, we sought to replicate previous findings of 'social' place cells, found to fire in response to the position of a conspecific in the environment[10,11]. The findings presented in this study first and foremost serve as a cautionary tale—if humans do impact ongoing neural signal, future data collection paradigms should account for or eliminate uncontrolled effects of experimenters. Moreover, this study is a first foray into the nascent field of cross-species neural representation. This field aims to investigate the neural code underlying cross-species representation and propose models of how animals with different affordances jointly negotiate their environment.

The results this study show that a large fraction of hippocampal neurons in flying bats were robustly modulated at takeoff and/or landing depending on the identity of the human at the landing target, suggesting a joint representation of allocentric position and context that includes information about the experimenter. In stationary bats, we found populations of neurons encoding experimenter position as they walked around the room, as well as the position of the flying conspecific. The findings from this study highlight potential uncontrolled effects of humans during behavioral experiments and open the door to discovering the neural code for cross-species representation. The first extension of this work would seek to understand how the representation of a given non-conspecific evolves as the relationship between the recording animal and experimenter change. To build a foundation for this work, a crucial first step is to understand whether the neural representation of space evolves over time without the perturbances from non-conspecifics in the environment.

1.3 Solo flight behavior is supported by a stable hippocampal code

Skilled spatial navigators like the Egyptian fruit bat exhibit spontaneous and highly reproducible flight paths in the lab environment. We sought to discover whether a stable hippocampal code underlies this robust flight behavior under the simplest condition of solo flight. This experiment was critical to understanding the hippocampal place code in fruit bats, because findings from other model organisms including rats and mice have yielded competing conclusions about the stability of the place code and do not necessarily generalize across species[12–20]. The results from this study will provide a foundation to study how the representation of non-conspecifics in the environment changes as a function of familiarity and consistent interaction.

We used wireless single photon calcium imaging to record hippocampal neurons across days as single bats flew to two distinct reward locations in a large room. The bats spontaneously developed a repertoire of several different types of flight paths to reward and roost locations. We found that neurons that could be tracked across days consistently fired in the same location on

the same flight path, even if a given flight path was not executed for days between recordings. Notably, if a flight path morphed substantially across days, different neurons were active during these flights. Thus, if flight paths were grouped according to gross spatial location instead of the precise trajectory, this could lead to illusory instability in the hippocampal code. The methods and findings from this study provide a platform to study whether the neural representation of conspecifics is also stable over time, and future experiments may help refine models of spatial representation when there are sporadic local perturbations in a familiar environment.

Chapter 2: The neural representation of human experimenters in the bat hippocampus

2.1 Introduction

Human experimenters are commonly present in laboratory environments where they interact with subject animals during experiments. Yet, the behavior of humans in such settings is rarely monitored or reported. Studies have shown that the presence, actions, and sex of humans can influence the animal's behavior[4–8], as well as volume- and time-averaged neural responses such as local field potentials[8] or immediate early gene expression[9]. However, the impact of human experimenters on the neural dynamics of single neurons in behaving animals remains entirely unknown. To address this, we focused on the dorsal hippocampus, a region known to encode positional information and environmental factors[21–23] and the study of which often involves humans actively interacting with the animal subjects[10,12,21,24–30]. We explicitly tested whether and how neural dynamics of hippocampal neurons are influenced by the presence and actions of human experimenters. We utilized the Egyptian fruit bat whose highly structured spatial behavior[31] affords a rigorous control over behavioral variability. This allowed us to disentangle the ongoing neural modulation related to the presence and behavior of human experimenters from the positional coding prevalent in hippocampus.

2.2 Stable flight behavior across experimenters during a reward task

To examine the influence of human experimenters on neural activity in the bat hippocampus, we designed a spatial reward task where pairs of bats could spontaneously fly to two experimenters standing at different locations in a room to obtain a fruit reward from their hand (Fig. 1a; Chapter 2 Supplementary Methods). To minimize variability, the experimenters' hands were rested on fixed platforms of identical heights and were covered by gloves of the same size (Chapter 2 Supplementary Methods). Every five minutes, the experimenters swapped locations with one another to allow sufficient sampling of human positions and flight behavior. To monitor the spatial behavior of both bats and humans, we used a real-time-location-system (RTLS) that recorded the 3D position of both bats and humans in the room simultaneously with high spatiotemporal precision[32] (Supplementary Fig. 1). The bats were very active during the behavioral sessions, resulting in many flights landing at the same locations but on different human experimenters (217 ± 59 total flights/session/bat, mean ± s.d., n = 4 bats; Supplementary Fig. 2a-b). Importantly, the bats spontaneously flew highly structured flight paths that were repeated at high precision towards different experimenters (Fig. 1b-c; Supplementary Fig. 2c).

This provided a natural "behavioral clamp" on the bat's spatial variability across flights, which in turn allowed rigorously assessing the modulation in the neural activity associated with a particular human experimenter at the landing location.

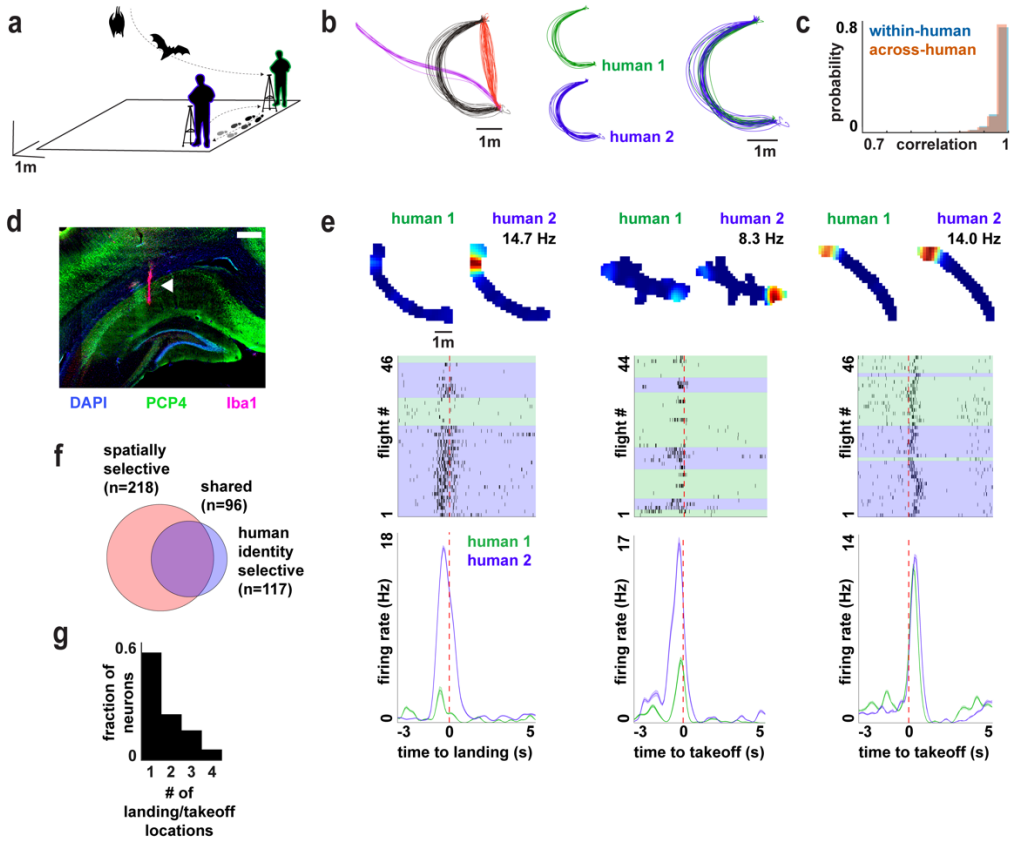

Fig. 1 | Hippocampal activity is modulated by experimenter identity during flight.
a. Experiment schematic: two bats flew for reward in a self-paced task where two human experimenters (green and blue outline) provided reward at different fixed locations around the room. Only two tripods shown for illustrative purposes; bats and humans not to scale (Chapter 2 Supplementary Methods). Scale bar refers to room dimensions. **b.** Left: Top view of the three most executed trajectories during a representative session. Colors denote different flight trajectories of one bat. Middle: example trajectory with flights colored by the identity of the human, experimenter #1 (green) or experimenter #2 (blue), at the landing target. Right: flight trajectories overlaid. **c.** Histogram of correlation values between flights of the same trajectory to the same (light blue) or different (orange) humans for all bats and all sessions (n = 18,450 within-human flight pairs, 14,572 = across-human flight pairs). **d.** Coronal section of the dorsal hippocampus from one recorded bat, stained for DAPI, PCP4 and Iba1. 14 out of a total of 16 tetrodes (across four microdrives and four bats) were successfully identified and localized in the dorsal hippocampus. White arrow denotes tetrode tracks. Scale bar: 500 µm. **e.** Three representative units, with the left and middle units showing modulation of activity depending on the identity of the human at landing and a third one (right) which does not. First row shows 2D rate maps for all flights from the same location, grouped by the identity of the human at landing. Peak firing rate is indicated. Second row shows the raster plot of that same neuron for all flights included in the 2D rate map. Background color corresponds to the identity of the experimenter at landing (green is human #1, blue is human #2). Third row shows the PSTH of the raster plot above. Color of PSTH matches color in the raster. Shaded area in PSTH denotes standard error of the mean. **f.** Number of units that carried significant spatial information about the bat's position during flight (red), and those that significantly modulated their firing rate at takeoff and/or landing according to the identity of the human at landing (blue). **g.** Number of landing/takeoff locations for which a neuron was significantly modulated depending on the identity of the human at landing. Only neurons that could be analyzed at four or more locations are included in the analysis (n = 134 cells).

2.3 Hippocampal neurons are modulated by experimenter identity in flight

We wirelessly recorded the activity of 307 dorsal CA1 hippocampal neurons from four bats engaged in the behavioral task (Fig. 1d, Chapter 2 Supplementary Methods, Supplementary Fig. 3). Most of the units that were active during flight fired primarily around take-off and landing and carried significant spatial information about the recorded bat's position (84.2% or 218 out of 259 flight-active cells when assessed in 2D, and 71.3% or 176 out of 247 flight-active cells along specific trajectories; Bonferroni corrected; Supplementary Fig. 4; Chapter 2 Supplementary Methods), consistent with an allocentric representation of self-position within the environment[21,22,33]. However, when inspecting activity of each unit across flights, we also observed substantial variability in the neural responses (Supplementary Fig. 5). We therefore asked whether the firing of hippocampal neurons might also be modulated by the spatial locations and identities of other individuals—conspecifics or humans—in the room. We found that nearly half of the neurons significantly modulated their firing rates depending on the identity of the experimenter at the landing location (48%, 117 out of 244 analyzable units; Fig. 1e-f and Supplementary Fig. 5b – left and middle examples; remapping quantified in Supplementary Fig. 6 and Supplementary Fig. 7; Chapter 2 Supplementary Methods). Changes in firing rates were stable between earlier and later parts of the session (Supplementary Fig. 8). Moreover, most neurons were significantly modulated by human identity in only one location (Fig. 1g; Chapter 2 Supplementary Methods), pointing to a possible conjunctive code for positional and experimenter-identity information during spatial movement. To further examine the extent to which human identity and location significantly contribute to modulation of firing upon landing, we used a simple linear model (Supplementary Fig. 9a). This model enabled us to disambiguate between neurons using an additive code versus a conjunctive coding for human identity and location. The results aligned with the above finding and suggested that the conjunction of human identity and location is a significant contributor to the modulation in the activity of many hippocampal neurons (n = 127 neurons; Supplementary Fig. 9b and Supplementary Fig. 10).

Consistent with previous reports[32], we also found a subpopulation of neurons that were significantly modulated by the presence or absence of a conspecific at the landing location (8.4% 16 out of 191 analyzable units; Supplementary Fig. 11). To test whether this result could account for the differences in neural responses observed during flights towards different human experimenters, we constrained our analysis to only include flights where the other bat was not present at the takeoff or landing location. Even with this additional constraint, we found that over 40% of the units (41.2% or 77 out of 187 analyzable units) had significantly different firing activity depending on the identity of the human at the landing location (Supplementary Fig. 12). Therefore, the presence of a conspecific could not fully account for the neural modulation associated with the identity of the human experimenter. Furthermore, differences in reward quantities provided by different experimenters on a subset of the sessions (Chapter 2 Supplementary Methods) also could not fully account for changes in neural modulation (Supplementary Fig. 13). Together, these findings suggest that during self-motion, information about the identity and positions of humans in the environment explains a substantial portion of variance in hippocampal activity that cannot be accounted for by changes in self-position, movement patterns, reward quantity, or the presence of conspecifics.

2.4 Hippocampal neurons informative of experimenter location and identity during rest

During many behavioral experiments, the human experimenter is 'performing a task' in parallel to the animal, such as distributing food, handling the subject(s), or moving from one location to another[10,12,24,26–28]. We therefore conducted an additional experiment to explicitly ask whether hippocampal activity in a stationary bat contains information about the position and movement of experimenters in the room (Fig. 2a). To compare movement across experimenters while controlling for the bat's position, we leveraged the bats' natural tendency to rest in self-selected, yet highly consistent, locations in the room[32] (Supplementary Fig. 14). While the bat was resting, experimenters deliberately repeated fixed traverses from a designated starting location towards the bat (Fig. 2b-c and Supplementary Fig. 15; Chapter 2 Supplementary Methods). At the resting location, the human dispensed reward or briefly handled the bat and then followed a fixed path back to the start location. Experimenters randomly took turns performing traverses. When pooling all traverses from both humans, we found that a subpopulation of neurons carried significant spatial information about the position of the experimenter moving through the room (Fig. 2d; 20.3%, 44 out of 217 analyzable units; Chapter 2 Supplementary Methods). Given our observation of neuronal selectivity for human-identity in flying bats (Fig. 1) we asked whether similar identity selectivity would also be observed in stationary bats. We therefore split the trials according to the identity of the human traversing the environment and found that over a third of the units were significantly spatially informative about the spatial position of at least one experimenter (36%, 50 out of 139 analyzable units; Fig. 2e). Intriguingly, most identity-responsive neurons carried significant spatial information exclusively for one experimenter (86%, 43 out of 50 analyzable units; Fig. 2f-g). Furthermore, there was little overlap in the subpopulations of neurons modulated by the identity of stationary humans during self-motion and those modulated by the position of moving humans while the bat was at rest (10.6%, 7 out of 66 analyzable units), pointing to largely independent populations selective for human identity depending on the bat's behavioral state. Finally, we found roughly similar proportions of neurons selective for the human dispensing the reward (46% or 23 out of 50 analyzable units) or handling the bat (40% or 20 out of 50 analyzable units), with 14% of the units responding to both humans (7 out of 50 analyzable units).

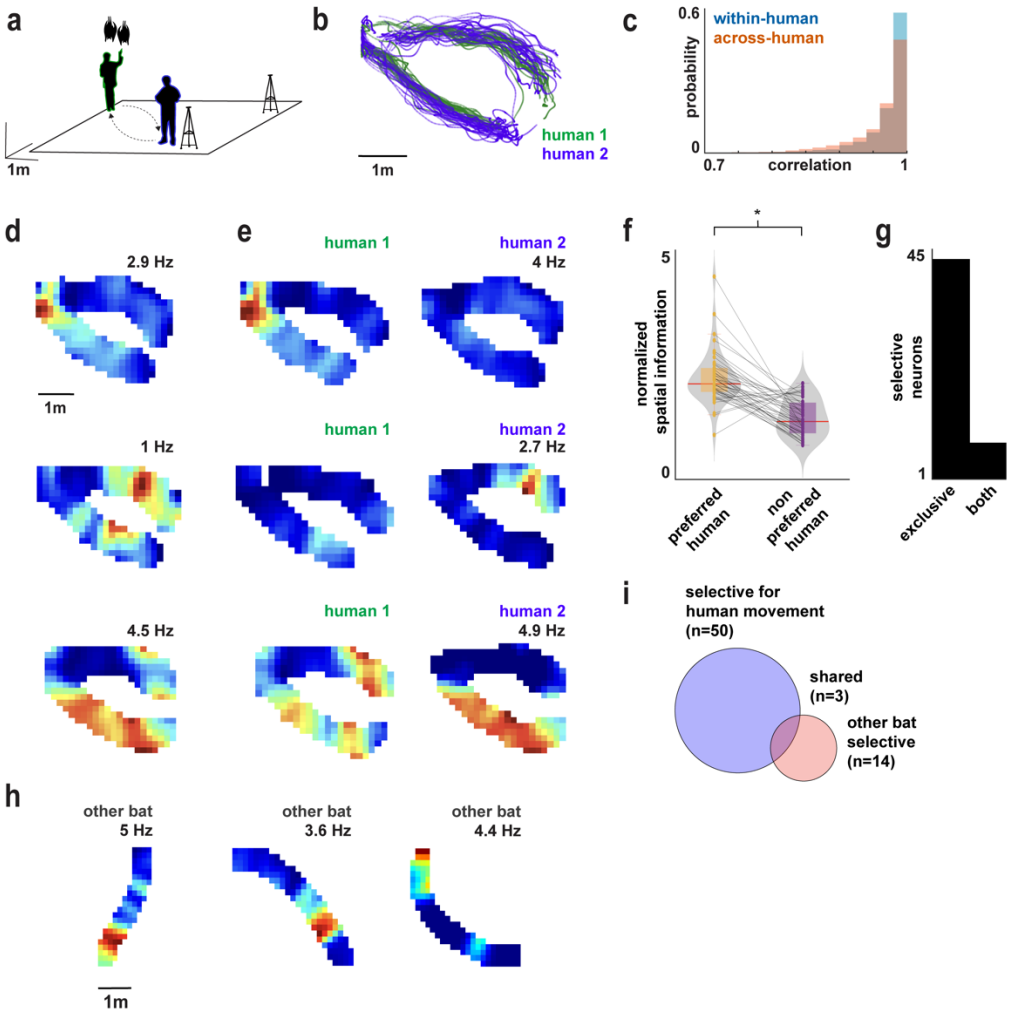

Fig. 2 | Hippocampal activity is modulated by experimenter movement and identity during rest.
a. Experiment schematic: Two human experimenters repeatedly approached the bats hanging in their preferred resting location. **b.** Top view of tracked position of both humans (human #1green, human #2 blue) performing traverses during a representative session. **c.** Histogram of correlation values between traverses within (blue), and across (orange) the different human experimenters (n = 5,904 within-human traverses, 5,829 across-human traverses). **d.** 2D rate maps of three representative units (rows) showing significant spatial selectivity for human position while the recording bat was stationary. Peak firing rate is indicated. **e.** 2D rate maps of the same three units as in panel '**d**', but split according to human identity. **f.** Normalized spatial information for the preferred human (for which a unit carried significant spatial information) and the non-preferred human (n = 43 neurons, asterisk indicates significant difference by two-sided Wilcoxon signed rank test, $p = 1.1 \times 10^{-8}$ Chapter 2 Supplementary Methods). Median indicated by thick red line on boxplot, bounds of box indicate 25th and 75th percentiles, error bars indicate minima and maxima. Violin plot shows kernel density estimate. Grey lines connect the same neuron across conditions. **g.** Numbers of neurons that carried significant spatial information for one human or for both humans (total n = 50 neurons). Note that nearly all neurons were selective for only one human. **h.** 2D rate maps of three representative units, showing significant spatial selectivity for the position of the other flying bat while the recorded bat was stationary. Peak firing rate is indicated. **i.** Number of units that carry significant spatial information about the location of either a human experimenter (blue), or the other bat in the room (red).

Previous reports suggested that the activity of hippocampal neurons in stationary animals may carry information about the position of a conspecific that is moving[10,11] (but see ref.[34]) We

therefore asked whether there was a comparable population of neurons encoding information about the position of the other bat in the room, and importantly, whether this might account for our results. We found a modest population of neurons that carried significant spatial information about the position of the other conspecific while the recording bat was at rest (Fig. 2h; 10.8%, 14 out of 130 analyzable units). Interestingly, the populations encoding conspecific and human position were minimally overlapping (4.7%, 3 out of 64 analyzable units; Fig. 2i). Finally, excluding all epochs of conspecific flight during human traverses had no significant impact on the results (Wilcoxon signed rank test $p = 0.44$; Supplementary Fig. 16). Together, these findings suggests that there are units in the dorsal CA1 region of the hippocampus with a conjunctive code for the identity and position of the experimenter traversing the environment while the animal is stationary.

2.5 Discussion

Human observation and intervention shapes animal behavior in the laboratory[4–8]. Our study aimed to ask whether experimenter presence and behavior influenced the ongoing activity of hippocampal neurons recorded from animals engaged in a spatial behavioral task. Leveraging the highly structured spatial behavior of bats we found that neural responses were robustly modulated by experimenters when bats were flying or stationary. These findings emphasize the potential gravity the human experimenter incurs on the dynamics of single neurons recorded from behaving animal subjects.

In this study we explicitly tracked the position of each human interacting with the subject animals, but this is not the case in most experiments, even those where the experimenters commonly interact with the subject animal during neural recordings. These interactions include delivering reward[10,12,30], physical relocation[24,25] and manipulating objects or barriers as part of the behavioral task[10,24–27]. In these and other cases, the human is spatiotemporally coupled with the animal's behavior in the environment. Given our findings, we encourage the neuroscience community to control, and if possible eliminate, the immediate and latent effects of experimenter behavior on neural data collected during a behavioral task.

The scope of this work was intentionally confined to a minimal number of subjects (two bats and two humans) while still providing sufficient complexity to assess whether the presence, behavior, and identities of humans impacted ongoing neural activity. Yet, further work is needed to elucidate the complex interactions that emerge between experimentalists, subjects, and other salient features of the environment. Such studies should systematically vary the number of humans, animals, and their relationship history, while controlling for behavior. Additionally, while this study focused on female Egyptian fruit bats, it would be important to further investigate experimenter representation across species and sensory modalities as well as across sexes of both experimental animals and researchers.

Our study focused on interspecies interactions in the laboratory environment. Yet, most animals navigate environments populated by members of other species, or live within demarcated territories, making interspecies interaction and representation a critical factor in shaping behavior and spatial decisions in the wild. The behavioral narrative of interactions between different species is often driven by the degree of overlap in their ecological niches, or their relationship as recognized predator and prey. For example, interspecies relationships surrounding feeding and hunting behaviors have been characterized across taxa[35] and include co-predation and competition for small prey between humans and reticulated pythons[36], cooperative

hunting amongst grouper fish and moray eels[37], domestication of aphids by ants[38], and cooperative hunting between groups of surface-hunting fish and seabirds[39]. Yet very little is known about the neural landscape during interspecies interactions. In the laboratory environment the human experimenter and the subject animal are engaged in a complex and dynamical interspecies relationship that is suitable for rigorous study of the neural basis of interspecies interactions. This line of investigation lends itself well to incorporating a diversity of animal models across a range of subdisciplines[40] and highlights the importance of eliminating the uncontrolled effects of humans on the examined neural phenomena.

2.6 Future theoretical frameworks for spatial representation in multi-species environments

A key challenge of learning how to behave in spaces with multiple animals is how to optimize actions when changes in the environment depend on others' as well as an animal's own actions. This problem can be simplified by either ignoring the other individuals or leveraging established communication protocols and behavioral narratives to make better predictions about upcoming states[41,42]. Established narratives such as predator-prey or common threat signaling are potentially fruitful platforms to study the neural mechanisms that support cross-species representation[41–44]. However, if there is no established narrative, as in the case of naïve lab animals and experimenters, the two species must build a communication protocol from scratch to successfully predict how their joint environment will evolve.

Historically, there are robust paradigms for establishing behavioral narratives across species, largely from the practices of equine and canine training[45,46]. These protocols emphasize consistency, routine, and gradual behavioral shaping as the backbone for effective training and highlight the importance of establishing rudimentary communication between the animal and the trainer. In laboratory behavioral science, these principles of consistency, routine, and behavioral shaping are practiced by experimentalists to obtain high-quality performance from subject animals[4,5], but the emphasis has shifted from establishing a behavioral narrative to executing a best practices protocol. This reductive approach to cross-species interactions in the lab obfuscates a fascinating question: what are the neural mechanisms that support establishment of a successful behavioral narrative between species with different affordances?

This question lends itself well to both a mature theoretical framework (reinforcement learning) and a practical empirical setting (any behavioral neuroscience lab). Reinforcement learning models capture how an agent constructs a behavioral policy using the values of state-actions pairs it experiences, and recently these models have been extended to multi-agent cases[47]. This framework may be further extended to capture the iterative evolution of a cross-species narrative and the biological constraints of this slow and sparse learning process. The experimental platform to test these models could be supported by any single-species behavioral neuroscience lab, or labs with multiple interacting species. A first extension of the work presented in this chapter could test whether current linear RL models (i.e. the successor representation[48,49] or default representation[50,51] capture the changes in neural representation that occur as the joint behavioral policy of two animals crystallizes. This experiment would marry the cross-species experimental paradigm from chapter 2 and the recording methodology pioneered in chapter 3 to examine the stability of neurons across days as a bat learns the role of the human experimenter in the environment.

Chapter 3: A stable hippocampal code underlies structured flight motifs during solo navigation in bats

3.1 Introduction

To tackle the question of how an animal's representation of a shared environment emerges and crystallizes over time, it is crucial to establish a method for reliable, wireless, multi-day recording, and understand the neural code that supports a solo animal's representation of the environment over time. As an author on this project, I performed data collection, preprocessing, and initial exploratory analyses. The joint first authors of the project were Tobias Schmid and William Liberti, and the other coauthor was Angelo Forli.

Neural activity in the hippocampus is believed to support spatial memory and navigation across a wide range of species[2,3,21,22,52], including in bats[33,53]. Egyptian fruit bats (*Rousettus aegyptiacus*) are renowned for their spatial memory and navigational abilities and are believed to use cognitive map-based navigation to forage in the wild[1,2,54–57]. Members of this species navigate along structured paths night after night for many months, pointing to the potential existence of a stable representation of their environment[55,56]. Early studies utilizing extracellular electrophysiological recordings in rats reported that the spatial firing of hippocampal neurons remained stable in familiar environments over days[12,13] and weeks[14], thereby supporting the existence of a stable hippocampal code[2]. In contrast, studies in mice utilizing recent advances in optical imaging methods, which overcome several of the shortcomings associated with longitudinal monitoring of individual neurons' activity using electrophysiological recordings[58,59], reported a highly dynamic code[15–20]. These studies found that, even in familiar environments, only a subset of hippocampal neurons remained spatially selective from one day to the next, yet the ones that did, maintained their original spatial preference – suggesting a temporally drifting positional code[15–20]. Therefore, the stability of the hippocampal code in familiar environments and across species remains in question.

3.2 Wireless imaging from CA1 in flying bats

Here, we used custom wireless miniature microscopes[60] to longitudinally image neural activity from the dorsal CA1 hippocampal region of Egyptian fruit bats (Fig. 3a-e; Chapter 3 Supplementary Methods) engaged in self-paced, goal-directed aerial foraging[61] (Fig. 3d, Supplementary Fig. 17). We expressed Ca^{2+} indicators (GCaMP6f) in CA1 neurons and monitored their activity through an implanted GRIN lens (Fig. 3b; Chapter 3 Supplementary Methods). This approach enabled us to track activity of the same cells over multiple days (Fig. 3c). In line with previous electrophysiological recordings from the hippocampus of freely flying bats[33,53,62], we found that individual neurons were primarily active during flight (Fig. 3e), exhibited spatial selectivity (Supplementary Fig. 18a), and combined, spanned the available environment (Supplementary Fig. 18b-c). Each bat (n = 7) developed a unique set of structured 'flight paths' that were executed with high precision (Fig. 3f; Supplementary Fig. 19a-b). Aligning neural activity to specific flight paths revealed time-locked responses in the majority of recorded neurons (494/562, or 87.9%, of regions of interest [ROIs] significantly tuned to flight; Fig. 3g;

Supplementary Fig. 19c-d; Chapter 3 Supplementary Methods). Furthermore, neural activity was largely distinct for different flight paths, with spatially overlapping portions exhibiting more similar activity (Supplementary Figs. 20) irrespective of distance or angle to goal location (Supplementary Figs. 21; but see ref.[63]).

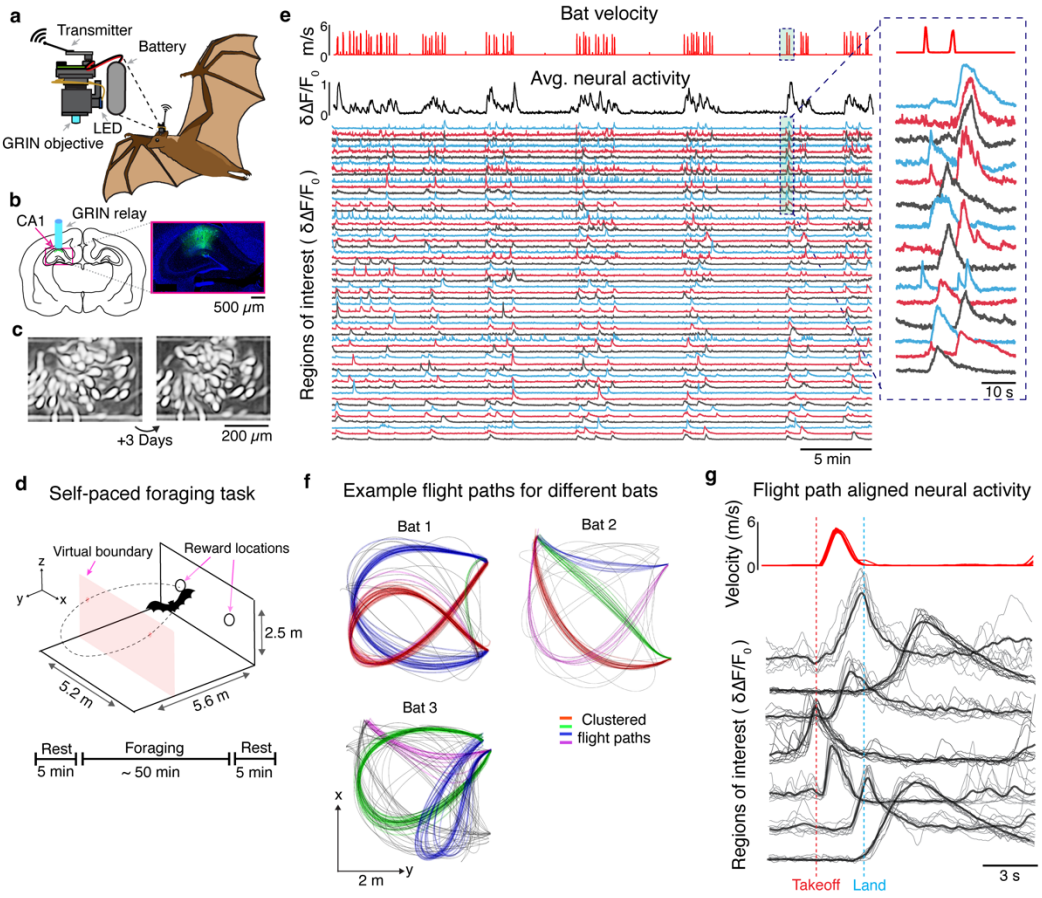

Fig. 3 | Wireless calcium imaging and spatial movement patterns in freely flying bats
a. Bats carry a wireless miniature microscope system during flight. **b.** A GRIN lens was implanted above dorsal CA1. *Inset:* Coronal section of the hippocampus with GCaMP6f stained in green and DAPI nuclear stain in blue. **c.** Two example maximum intensity projections from one animal, separated by three days. **d.** Flight room schematic and experimental paradigm. Two feeders on one wall dispensed a puréed fruit reward upon landing if a virtual boundary was crossed during the flight. *Bottom*: experimental session timeline. **e.** Experimental data from the same animal shown in (c). *Top:* bat velocity (m/s), *middle:* mean calcium activity of all regions of interest (ROI), units are normalized $\Delta f/f_0$, *bottom:* fluorescent time series of 55 ROIs over the entire foraging session. *Inset:* zoom-in on calcium activity during two flights. **f.** Representative flight paths (top view, XY projection) across a single session from three different example bats showcasing the diversity of structured routes taken by each animal. Flights for each bat are clustered by similar paths (colors). **g.** Neural responses aligned to flight activity. *Top*: bat velocity (m/s) for 15 flights along the same path, *bottom:* calcium traces from seven simultaneously recorded ROIs for flights along the same path in a single bat, aligned to flight takeoff. The mean across flights for each ROI is in black. Individual flights are in gray.

3.3 Stable hippocampal tuning during flight

Flights along the same path were highly correlated both within and across days (the mean flight correlation changed at a rate of -0.001 per day, $R^2 = 0.68$, $p = 1.6\text{x}10^{-3}$; Fig. 4a; Chapter 3

Supplementary Methods). Since hippocampal activity is known to be modulated by ongoing spatial movement[64–66], including in bats[33,53,67], we leveraged the highly structured, stable nature of the bat's flight to assess hippocampal tuning stability during a spatial behavior that exhibited low variability. We observed that spatial tuning was stable for the majority of neurons that were tracked over days (Fig. 4b-d; Supplementary Fig. 22a-h; Chapter 3 Supplementary Methods). Stability persisted even when specific paths had not been flown for several days, suggesting that stable spatial tuning may not require continuous behavioral reinforcement (Supplementary Fig. 22i-j). Only a small fraction of well-isolated ROIs (2.6%) that were clearly visible on one session could not be located on an adjacent session (Supplementary Fig. 23; Chapter 3 Supplementary Methods).

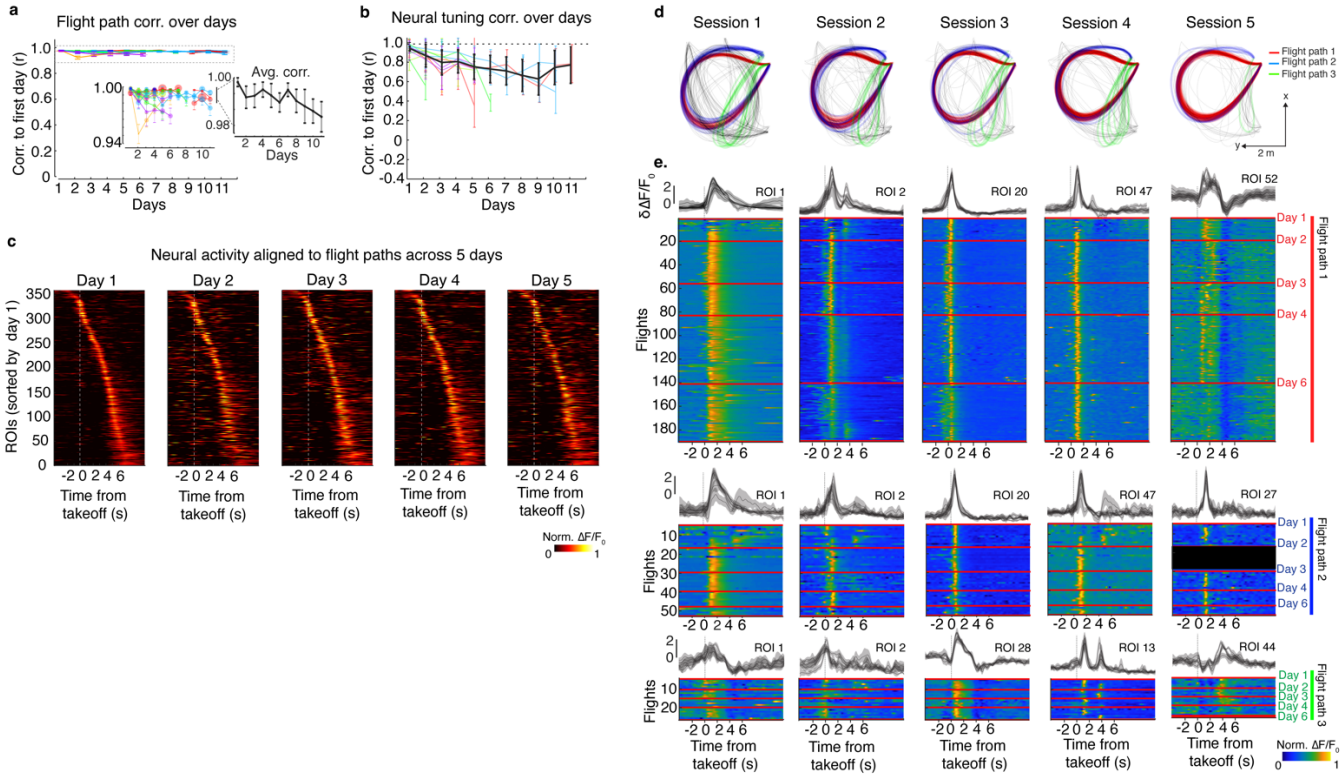

Fig. 4 | Neural tuning for stable flight paths persists across days
a. Average correlation of flights from the same cluster across different day lags, computed relative to the first day for each bat (different colors). Marker size corresponds to the relative number of flights in a session. *Inset*: zoom-in on the higher correlation values. Error bars indicate 99% confidence interval, black line indicates the mean across $n = 7$ bats. **b.** Average correlation of neural tuning to the first day across all spatial firing fields and across different day lags for each bat; each color indicates a different bat. Error bars indicate 99% confidence interval, black indicates the mean across $n = 7$ *bats*. **c.** Trial-averaged activity from all significantly flight-tuned neurons from all animals that can be tracked over a five day interval, sorted by peak activity on day one. The same sorting is maintained for all subsequent days. **d.** Example flight patterns across five sessions performed over six days. Common flight paths are colored red, green, and blue. **e.** Example ROIs (normalized $\Delta f/f_0$) aligned to takeoff (vertical gray dotted line) of the three most common flight paths. The x-axis is extended relative to (c) in order to show the calcium signals return to baseline. *Top:* mean activity trace for each day (gray); Shading represents SD. Bottom: chronological trial-by-trial responses aligned to flights (different flight paths are separated from top to bottom); red lines for each ROI separate different days. Black (in ROI 27) indicates that the ROI was not confidently identified for that session.

3.4 Illusory instability via behavioral variance

Despite the overall stability exhibited by the majority of hippocampal neurons in flying bats, there was still a quantifiable decrease in the average tuning over days relative to repeated flight paths (significant linear decrease in mean ROI tuning correlation of 0.02 per day, $R^2 = 0.54$, $p = 9.1 \times 10^{-3}$, Fig. 4b; see two examples in Fig. 5a). However, we found that even these relatively small changes in tuning were significantly correlated to flight-to-flight variability ($R^2 = 0.2$, $p = 3.2 \times 10^{-29}$; Fig. 5a-c, Supplementary Fig. 24a-b; Chapter 3 Supplementary Methods). For neurons tuned to multiple flight paths, we found that neural activity on more variable paths displayed greater variability ($p = 9.7 \times 10^{-15}$ Wilcoxon Rank Sum; Fig. 5d). Similarly, tuning stability was degraded when only considering unstructured flights (i.e., unique flight paths that do not repeat and are therefore inherently more variable) as compared to the bat's structured flights (Supplementary Fig. 24c; Chapter 3 Supplementary Methods), suggesting that stability is not an intrinsic property of individual neurons but instead reflects behavioral variance. To further understand how behavioral changes over days impact our estimation of neural tuning, we implemented a simulation in which stable spatial firing fields are convolved with the empirically observed flight paths. This allowed us to approximate a null model of a stable code that considers differences in flight patterns from day-to-day (Fig. 5e; Chapter 3 Supplementary Methods). We found that the empirically observed decrease in coding stability qualitatively matched what we would expect given behavioral drift and a stable underlying neural code (Fig. 5f).

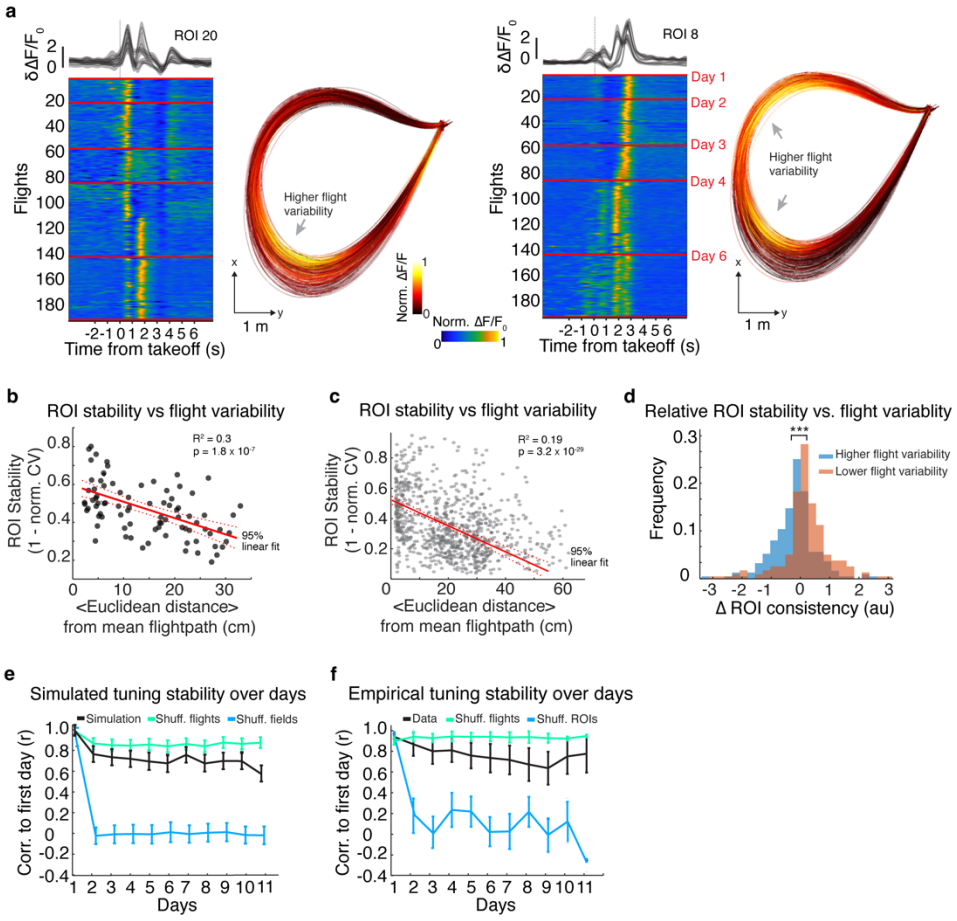

Fig. 5 | Apparent changes in neural tuning can be explained by measurable changes in flight behavior

a. Two example ROIs with apparent unstable tuning. For each example, *left top*: average calcium responses in units of normalized $\Delta f/f_0$, aligned to takeoff (vertical gray dotted line); *left bottom*: chronological flight-by-flight responses, red lines indicate day transitions, *right:* calcium $\Delta f/f_0$ superimposed as a heatmap onto an XY projection of individual flight paths. Note that the neuron is active where there is increased flight variability. **b.** Correlation of ROI stability and flight variability (Chapter 3 Supplementary Methods) for the example bat shown in (a), demonstrating that flight-flight variability is significantly correlated to the trial-trail variability seen in neural activity. **c,** Same as (b), but across all ROIs for the top three flight paths for all bats. **d.** Comparing flight-by-flight consistency for ROIs that are significantly tuned to more than one trajectory. ROI consistency is separated into two groups based on flight variability: more variable flights in blue and less variable flights in orange (i.e., a sharper distribution of Euclidean distances from the mean flight path at the deconvolved burst time). Note that there is a significant difference in the distribution of flight-by-flight consistency with lower flight variability corresponding to higher neural consistency. **e.** Average ROI correlation to day one across different lags (days) for simulated stable firing fields in black, shuffling ROI identity (blue), and shuffling flight order to eliminate behavioral drift (green). **f.** Same as (e) but with mean correlation of empirically recorded Ca^{+2} data for all ROIs across different lags for each bat in black, shuffling ROI identity (blue) and shuffling flight order to eliminate behavioral drift (green). Bars for (e-f) indicate 99% confidence intervals of the mean across n = 7 bats. *** $p < 0.001$.

3.5 Stable tuning across sensory contexts

The results presented thus far demonstrate that the hippocampal code in flying bats is highly stable, and the ability to estimate neural tuning stability can be compromised by variability in spatial behavior. This in turn suggests that greater apparent tuning instability may arise from more substantial changes in spatial movement patterns, even if the animal continues to navigate in the same environment. To explore this notion further we leveraged recent findings in bats where a comprehensive change in sensory context (turning off the lights) appeared to induce a significant changes in hippocampal spatial tuning[28]. We therefore asked whether greater changes in neural tuning could also be accounted for by altered behavior between different contexts. To address this question, we conducted an additional set of longitudinal calcium imaging experiments during which the lights alternated on for 20 minutes (lights-on), off for 20 minutes (lights-off), and on again for 20 minutes (lights-on') during each foraging session (Chapter 3 Supplementary Methods). When comparing two-dimensional (2D) rate maps across conditions we observed what appeared to be condition specific sensory remapping, in agreement with previous electrophysiological findings in bats[28] (Fig. 6a; and Supplementary Fig. 25). However, a closer examination of the bats' spatial movements patterns revealed that while flight behavior was highly similar within a given contextual condition (lights-on or lights-off) it was highly dissimilar across conditions (10 sessions per bat for $n = 2$ bats; Fig. 6b; Supplementary Fig. 26). The bats still flew along structured paths in both conditions, but many paths were flown disproportionately more often in either the lights-on or the lights-off condition (Fig. 6b, Supplementary Fig. 26a-g). Taking advantage of both the stability of the bats' flight behavior and our ability to longitudinally track individual neurons over days, we were able to accumulate many examples of trajectories that occurred across both conditions (Supplementary Fig. 26h-i). When restricting our analysis to these flight trajectories, stable neural tuning persisted (Fig. 6c-e) and we found no statistical difference in population tuning stability when comparing within or across conditions (Fig. 6f). To further address if differences in flight behavior may account for perceived changes in spatial tuning, we compared 2D rate maps of simulated stable tuning fields for all flights across both lights-on conditions, and between lights-on and lights-off conditions. Similar to what we observed empirically (Fig. 6f), we found that illumination-dependent changes in flight variability gave the appearance of stability within lights-on conditions but instability when comparing across conditions (Fig. 6g). Taken together, these findings demonstrate that condition-dependent changes

in behavior can lead to the illusion of tuning instability, even when the underlying neural code remains highly stable.

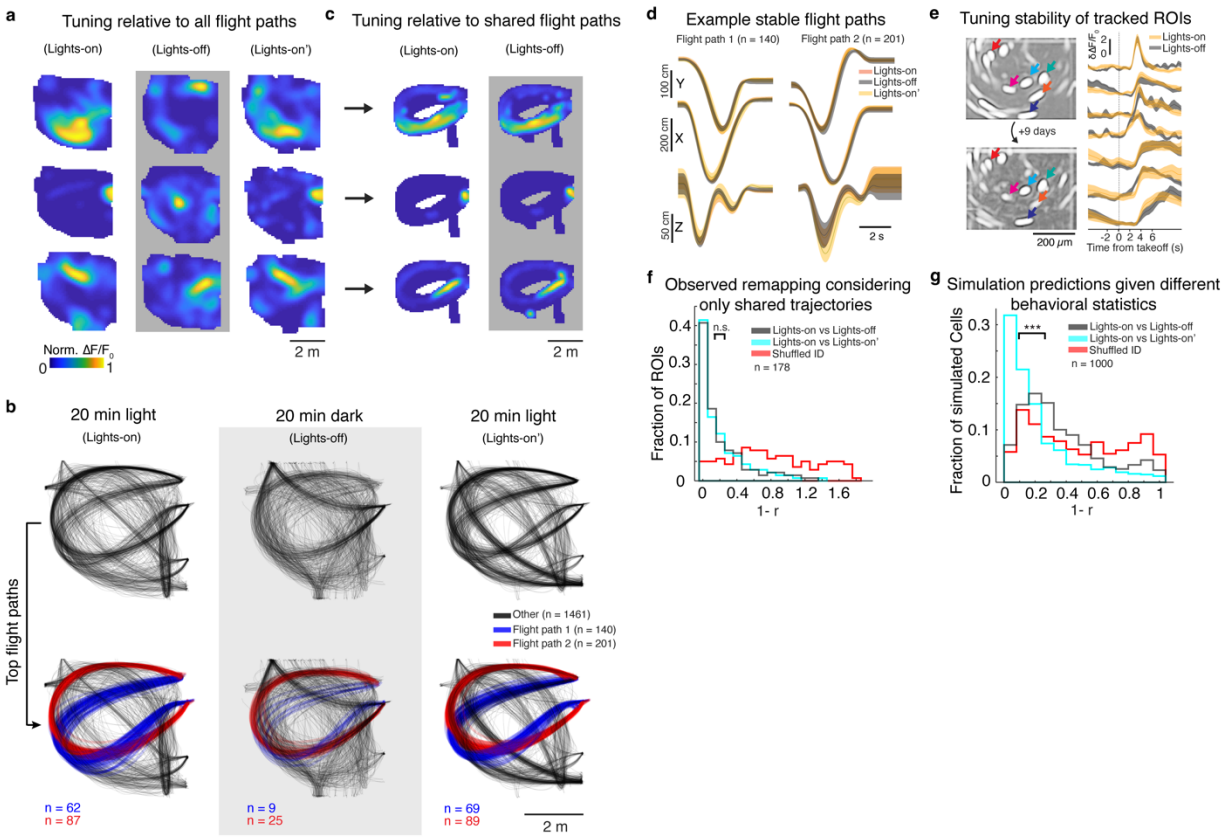

Fig. 6 | Neural tuning persists despite a change in sensory context
a. 2D firing maps for three example ROIs in lights-on vs. lights-off cue conditions when considering all flights in each condition. **b.** *Top:* all flight paths that occurred across 10 consecutive days for one example bat, divided into successive lights-on, lights-off, and lights-on' periods (ordered from left to right, respectively). Bottom: two routes that persisted across all conditions, clustered in red and blue. Number of flights for each route in each condition are indicated. **c.** 2D firing maps for the same three ROIs shown in (a), only considering the same spatial trajectories exhibited in both conditions. **d.** Change in X, Y and Z position over time and across lighting conditions for the two conserved routes taken in the lights-on and lights-off periods shown in (a). Shading represents 2x STD. **e.** Left: maximum intensity projection of the calcium activity in a single foraging session from one bat, separated by nine days, with a subset of tracked ROIs labeled with colored arrows. Mean $\Delta f/f_0$ calcium responses aligned to the same path in the lights-on (yellow) and lights-off (gray) conditions. Shading indicates standard deviation. **f.** Distribution of ROI tuning changes of 2D firing rate maps across the lights-on vs. lights-on' conditions (teal), and lights-on vs. lights-off (gray) conditions are not significantly different (n = 178 fields, $p > 0.05$, two-tailed Wilcoxon Rank Sum Test). **g.** The correlation of 2D firing rate maps of simulated stable tuning fields is significantly different when comparing across the lights-on vs. lights-on' conditions (teal), and lights-on vs. lights-off conditions (gray). Both are significantly different from shuffling the field identity (red). *** $p < 0.001$.

3.6 Discussion

By imaging neural activity from flying bats, we found that hippocampal spatial tuning for the same movements in a familiar environment is highly stable. Furthermore, most of the neurons that were reliably tracked over days remained active and spatially selective when bats flew the same

trajectories, suggesting a stable participation of individual neurons in representing spatial movements through a familiar environment, even after dramatic changes in sensory context. These findings support earlier electrophysiological studies in rats that posited a stable hippocampal code as a substrate for the stable spatial representation of a familiar environment[1,2,14]. However, our findings differ from imaging studies in head-restrained or freely moving mice over the past decade that showed large fractions of hippocampal neurons can change their responsiveness from one day to the next[15–18]. We hypothesize that these differences could arise from several sources. One possibility is that the stability of spatial representation varies between species, where mice may generally have a less stable hippocampal code. Indeed, electrophysiological studies in mice revealed drifting spatial representations even within a single foraging session[68], whereas rats exhibit more stable spatial neural activity[12]. Yet, factors such as task engagement, goal-directed behavior and attentional demands have been shown to account for some of the observed differences[68,69]. On the other hand, it may be that the estimation of spatial tuning stability is impacted by movement repertoires exhibited by different species. For bats, flight can result in a highly structured, homogenous behavior. The spatiotemporal consistency of the bats' flight allowed us to repeatedly sample the same behavior in a given location across time and cue conditions, which in turn enabled us to make straightforward, statistically rigorous comparisons between behavioral and neural variability. To this end, we have shown that relatively subtle changes in spatial movement patterns across days or contexts can lead to challenges in accurately assessing the stability of firing fields. A prediction arising from these findings is that a stable hippocampal code may be observed across species when neural tuning is assessed relative to a more structured navigational behaviour[70,71] that allows simultaneous control over multiple factors that are known to modulate hippocampal activity such as position, velocity, movement direction and time[64,65].

The neurophysiological findings presented here support a model where the spatial representation of stable movement patterns through a familiar environment remains largely unchanged[2,14]. While such a stable neural code might facilitate the stable navigation behavior exhibited by Egyptian fruit bats[54–57], a direct causal role of the bat hippocampus in aerial navigation remains to be demonstrated. Combined, our findings highlight the importance of using a comparative approach that leverages the specialized behaviors of different species to investigate how conserved circuits, such as the hippocampus, enable neural computations that subserve navigation and spatial memory[40,72].

Chapter 4: Conclusion

The findings presented in this dissertation underscore the importance of mitigating sources of uncontrolled variance when interpreting neural data and demonstrate the advantages of leveraging spontaneous behavior to investigate the neural code that supports a particular species' abilities. We found that the hippocampus discriminately represents individual non-conspecifics and conspecifics, using a joint code for allocentric position and context. Furthermore, the allocentric positional code for solo navigation was stable across days for repeated flight motifs. The immediate next step to deepen this line of work is to investigate whether the neural responses to conspecifics and non-conspecifics are flexibly or stably represented across days, and whether changes in the behavioral narrative between individuals in the environment shapes this representation over time.

Importantly, these two studies come with caveats and opportunities for empirical clarification. While the second study found that the hippocampal code was stable across days, it is unclear whether this stability would hold in tasks that demand more complicated and flexible navigation. Paradigms with larger spaces and changing barriers, which are commonly found in the rat literature on hippocampus, may provide a more convincing environment to test the stability of the code over time[73]. As a first step it would be valuable to investigate whether replay around barriers exists in the bat, considering the differences in locomotion and trajectory planning between the two species.

The primary caveat of the first study is that the task structure explicitly encouraged the bats to attend to the positions and movement of non-conspecifics, but not necessarily the conspecifics. This may account for the discrepancy in the number of neurons encoding the position of the human compared to the number encoding the position of the other bat. Other studies have found greater numbers of place cells representing the position of conspecifics in tasks that encouraged attending to the other conspecific[10,11]. An alternative paradigm to test the influence of task structure on relative representation of conspecifics and non-conspecifics is to implement a teacher-learner paradigm, in which one bat has been trained on the relative probabilities of reward given by each non-conspecific, and the learner bat can optimize their reward accrual by copying the teacher bat's flights. Using this paradigm along with high-density recording techniques, it may be possible to disentangle the neural representations of self trajectories (replay), conspecifics' trajectories, and the non-conspecifics' trajectories. This speculative 'other-replay' would reflect how temporal sequences of hippocampal neurons encode trajectories that other individuals (conspecifics and potentially non-conspecifics) execute[74].

From a computational perspective, this line of work may serve to test model predictions of how animals represent environments populated by members of other species. Models from the linear reinforcement learning literature, such as the successor representation and default representation, capture empirical properties of place cells and grid cells[48,50,51,75], and could make predictions about how dynamic agents would be represented in the environment. One computationally motivated question would extend an established model of hippocampus which posits that action sequences are preferentially replayed according to how important they are for learning an action policy[51]. Can these action sequences include those executed by species with different body schemas? In other words, is the allocentric hippocampal representation of place and its associated replay sequences separable from the animal's form of locomotion? Or are the allocentric code and replay sequences inherently tied to the motor actions that produced the action sequence? This question could be addressed using numerous cross-species experimental paradigms but would likely be most tractable using two animal models with similar resource needs and ecological niches. High-density recording methods and high-throughput preprocessing packages[76] provide a tractable methodological platform for investigating both rate and temporal codes of cross-species representation in hippocampus.

An individual's ability to negotiate ecosystems that are populated and influenced by many different species critically affects survival. And while our understanding of how the brain represents space and accomplishes navigation has matured over the past half a century, we have yet to define a singular model of the neural mechanisms that give rise to this incredible ability. Our hope is that using a combination of ethological behavior, unconventional animal models, and unique task paradigms can uncover key properties of the neural code and refine models for how the brain encodes the external world.

Chapter 5: Supplementary Materials and Methods

5.1 Supplementary materials and methods for Chapter 2

Subjects

Neural data was collected from four adult female Egyptian fruits bats (*Rousettus aegyptiacus*; ~ 110-130 g weight). All bats were housed in a humidity- and temperature-controlled room. Implanted bats were initially single housed in small cages, and subsequently, following recovery from surgery, co-housed in large cages. Lights in the housing room were maintained on a 12 h-12 h reverse light cycle (lights off-lights on; 07:00-19:00). All experiments were performed at the same time of day during the bats' awake hours (dark cycle). All experimental procedures were approved by the Institutional Animal Care and Use Committee of the University of California, Berkeley.

Behavioral setup

All experiments were performed in an acoustically, electrically and radio-frequency shielded room (5.6 m x 5.2 m x 2.5 m) with high precision lighting control[61], under uniform illumination (luminance level 5 lux). To minimize acoustic reverberation and dampen noise from outside the room, the walls and ceiling of the flight room were covered with a thick layer of acoustic foam. A layer of acoustically absorbing black felt was placed on top of the acoustic foam, and on the floors, to prevent the bats from damaging the foam or the floors and provide additional acoustic dampening. A layer of black netting was placed on top of the felt on the walls for the bats to hang. In addition to the bats, two adult humans, one male and one female, were also present in the room during experiments. Both humans gave informed consent to participate in the experiment.

The 3D spatial position of the bats and humans was recorded using a modified version of a commercial Real-Time-Location-System (RTLS, Ciholas Inc.), similar to that used previously[32]. The system was composed of mobile tags (DWTAG100) that were identified and localized at 100 Hz sampling rate by 16 static anchors (DWETH101) placed on the walls and ceiling of the room, providing reference locations for the system. Anchors and tags communicated through Ultra-Wideband pulses. An additional anchor (custom DWETH101) was used to record an external synchronization signal (see below). Each lightweight (~2.9 g) transceiver tag was powered with a LiPo battery (~15 g total). For bats, the transceiver tag was directly mounted on the neural implant. For humans, one tag was placed in the right lab coat pocket and one each on the left and right wrists, for a total of three tags per human (Supplementary Fig. 1). The system communicated with a computer outside the experiment room through UDP protocol and was configured and operated through a web-based user interface running on Ubuntu 18.04 Bionic. Data were recorded and saved with custom scripts in Python. The spatial resolution of the system was measured on a subset of the experimental sessions where one bat was simultaneously tracked with two recording systems: the RTLS and a precise marker-based motion capture system (Cortex Motion Analysis (6.2.13.1751); Matlab 2021a)[32,62] . The spatial resolution on tracked bats and humans was in the range of 10-20 cm. Periodic clock pulses generated by a Master-9 device (A.M.P.I.) were used to create a timing signature that

served as a common frame of reference for all the recording systems (tracking and neural recordings).

Four tripods were positioned around the room to demarcate the possible locations of the human experimenters. The tripods were all set to the same height and did not change positions across the entire experiment. Video of the room at all tripod locations and resting locations was acquired using IR cameras at 25FPS (Basler ace acA800-510um; Basler Pylon image acquisition software (6.2.0.8205)). Both humans wore the same standard personal protective equipment, which included a white laboratory coat, a blue hair bonnet, a blue surgical mask, blue gloves, blue shoe covers, clear protective glasses, and a protective yellow leather glove on the left hand. When standing at a tripod location, each human placed their left hand palm up on the tripod and used their right hand to dispense 0.3 ml of banana smoothie via wireless manually activated motorized feeder, when appropriate (Arduino Mega Rev3; Adafruit Motorshield 1438; Arduino IDE 1.8.19). Experimenter hand sizes and gloves were highly similar, which served as structurally and visually indistinguishable landing platforms for the bat. All bats were mildly food-restricted (> 90% of their baseline weight) before the task sessions. Prior to the start of the neural recording, the bats were introduced to the experimental setup, trained on the behavioral task described below, and were familiar with both experimenters.

Behavioral Task

Two experiments were performed in each recording session. In experiment #1 (~90-minute duration), bats were trained to freely fly to either human for reward. In experiment #2 (~30-minute duration), bats hung in their preferred rest locations while the humans approached the bats to feed or handle them. Experiment #1 was composed of several 15-minute blocks. During each block, the experimenters picked a pair of tripod locations to stand at for five minutes, then swapped locations for the next five minutes, and returned to their original locations for the final five minutes of the block. The blocks were counterbalanced such that each human spent an equal amount of time at each tripod location over the course of the session. To control for potential glove-specific cues from the yellow "landing platform" gloves, the experimenters swapped yellow gloves every block. Each time the humans changed locations they walked radially inwards from their locations to the center of the room, and radially outwards to their new locations. If a bat happened to fly while the humans were walking, the humans paused their movement. The bats could freely fly to any tripod in the room, but they were only rewarded if they landed on the experimenter's hand on the tripod. When a bat landed on an experimenter's hand, a single reward was dispensed, and the next feed could only be triggered by the bat flying away and returning. If the second bat happened to land on the same experimenter before the first bat left, reward was dispensed only to the second bat. For two of the four bats, two additional tripod locations were available (six locations total) for the humans to stand at, and human #1 gave 0.3 ml of reward, while human #2 gave 0.1 ml of reward. This difference in reward did not significantly impact the ratio of visits to each human (Supplementary Fig. 2b, Bat 3 and Bat 4). The ratio of the number of visits to human #1 versus human #2 was calculated for all sessions for all bats within an experimental paradigm (n = 20 sessions for the four-tripod paradigm and n = 11 sessions for the six-tripod paradigm. Two-tailed t-test, $p = 0.1$).

Experiment #2 immediately followed experiment #1. During experiment #2, the humans stood together at the center of the room, and randomly took turns performing traverses along a fixed, arced path to either feed or handle the bats hanging at their preferred rest location. Handling consisted of a standard mild restraining grasp while the bats were hanging that lasted

the same amount of time as the reward delivery. All traverses were performed when both bats were hanging in the preferred rest location, and each human rewarded the same bat across all sessions (their 'designated bat'). During each traverse, one experimenter walked from the center of the room in an arced path towards the bats, paused below the bats, fed their designated bat and handled the other bat, and walked an arced path back to the center of the room. A slight variant of this experimental paradigm was performed for two of the four bats, in which the humans waited at tripods instead of the center of the room, but still performed the same traverse from the center of the room to the bats, and back to the center of the room. In this variant the humans did not have a designated bat to handle/feed, and instead randomly chose which bat to reward each trial (n = 20 sessions for the designated-bat paradigm and n = 11 sessions for the random paradigm).

Microdrive Implant Procedure

Surgical procedures for electrophysiology implants were performed similarly to those described previously for Egyptian fruit bats[32,62,77,78]. A lightweight four-tetrode microdrive (Harlan 4 drive; Neuralynx, MT, USA) was implanted over the right hemisphere of each bat. Tetrodes were made from four strands of platinum-iridium wire (17.8 μm diameter, HML-insulated) and assembled as described previously. Each tetrode was loaded into a telescoping polyamide tube assembly inside the microdrive, and each tetrode was independently manipulable (~5 mm travel). 12-16 hours before surgery, the tips of the tetrodes were cut to the same length and plated with Gold Plating Solution (Neuralynx, MT, USA), bringing the impedance of individual wires down to 0.3-0.6 MΩ. The surgical procedure was as follows. Anesthesia was induced with an injectable cocktail of ketamine, dexmedetomidine and midazolam. The bat was placed in a stereotaxic apparatus (Model 942; Kopf, CA, USA) where a continuous supply of oxygen was provided, and anesthesia was maintained by injection (~once/hour) of a cocktail of dexmedetomidine, midazolam and fentanyl. Depth of anesthesia was continuously monitored by reaction to a toe pinch test, and by measuring the bat's breathing rate. Body temperature was measured with a rectal temperature probe and kept at approximately 35˚C with a regulated heating pad. After the proper anesthetic depth was reached, the skull was exposed and surrounding skin and tissue were retracted. The skull was then cleaned of any connective tissue and scored to improve adhesion and mechanical stability. A bone screw (19010-00; FST, CA, USA), with a short piece of stainless-steel wire (.008" coated; A-M Systems, WA, USA) soldered to the screw head, was inserted into the frontal plate of the skull and served as ground for the microdrive. Four shorter bone screws (M1.59 x 2 mm, stainless steel) were placed to further stabilize the implant. A circular craniotomy of 1.8 mm was made in the skull above the right hemisphere hippocampus CA1 at 5.4 mm anterior to the transverse sinus that runs between the posterior part of the cortex and the cerebellum and 3.7 mm lateral to the midline. The craniotomy was covered with a biocompatible elastomer (Kwik-Sil; World Precision Instruments, FL, USA) to protect the brain while the skull and the base of the screws were covered with a thin layer of bone cement (C&B Metabond; NY, USA). The Kwik-Sil was then removed to perform the durotomy and lower the microdrive, with tetrodes fully retracted, into the craniotomy. The microdrive was lowered to the surface of the brain to create a tight seal, and the remaining exposed part of the brain was covered with Kwik-Sil. Dental acrylic was applied in layers to secure the microdrive to the screws and the skull. A ground wire from the microdrive was connected to the wire from the ground screw, and the whole connection was embedded in the dental acrylic. Once the acrylic was dry, all four tetrodes were lowered to their initial positions, approximately 800 μm below the

cortical surface. To conclude the surgery, reversal agents were given to counteract the dexmedetomidine (Atipamezole) and midazolam (Flumazenil). After the bat woke fully from anesthesia an oral analgesic meloxicam (Metacam; Boehringer Ingelheim, Germany) was administered. After surgery, analgesics (three days) and antibiotics (seven days) were given daily until complete recovery.

Electrophysiology data acquisition, pre-processing, and spike sorting

After microdrive implantation, tetrodes were lowered in small increments every day over a period of 1-2 weeks, advancing towards the pyramidal layer of the dorsal hippocampus (CA1). The pyramidal cell layer was initially determined by the detection of high frequency "ripples" in the local field potential (LFP) signal, together with a transient (50-100 ms) increase in multi-unit activity. All tetrode adjustments were made while the bat was swaddled in a small fabric bag. Neural activity from the tetrodes was checked every day by connecting the bats' microdrive to a wired recording system (Digital Lynx; Neuralynx, MT, USA) before and after experimental sessions. At the end of each session, one or more tetrodes were moved (20-160 μm) in order to sample a different group of neurons (upon tissue stabilization the following day). Tetrode movements were timed to ensure maximal time for stabilization of the tissue before the next day's recordings. Tetrode positions were verified posthumously with histology (see below). To record neural activity while the bats were freely flying, we used a wireless neural data-logging system ('neural-logger'; MouseLog16, vertical version, Deuteron Technologies Ltd., Israel) similar to that used previously[32,62]. The logger was housed in a custom 3D printed case, along with the RTLS tag and two LiPo batteries (one for the logger and one for the RTLS tag, minimal duration: 150 min) and connected to the electrical interface board of the microdrive at the beginning of each recording. Implanted bats used in the experiment weighed more than 110 g and could fly normally while equipped with the neural-loggers and RTLS tags, as expected from previous experiments using wireless recording systems[32]. Electrical signals from the four tetrodes (16 channels) were amplified (200x), bandpass filtered (1-7000 Hz), sampled continuously at a frequency of 31.25 kHz and stored on a SD-card memory on the logger, with a voltage resolution of 3.3 μV. Wireless communication between the neural-logger and a static transceiver ensured proper synchronization and allowed basic monitoring and configuration via software (Deuteron Technologies). At the end of the recording session, data from the loggers were extracted and saved. Spike sorting was done as described previously[32,33,62]. Briefly, recorded voltage traces were filtered (600-6000 Hz) and putative spikes were detected by thresholding (3 standard deviations) the filtered trace. Putative spike waveforms (32 samples, peak at the 8th sample) were fed into the cluster sorting software (SpikeSort 3D, Neuralynx, MT, USA). Manual sorting was performed using spike amplitude and energy as the main features. We quantified interneurons as units having a mean firing rate of > 5 Hz, and identified a total of 24 interneurons. We found similar results between principal cells and interneurons. Specifically, 70.8% (17 out of 24 putative interneurons) carried significant 2D spatial information during flight, 45.8% (11 out of 24 putative interneurons) modulated activity depending on the identity of the human landing target, and 29% (7 out of 24 putative interneurons) of units carried significant spatial information for the position of a human traversing the environment. Thus, the fractions of interneurons that carry significant 2D spatial information, are human modulated, and carry information about the position and identity of the human are representative of the fractions in the general unit population and similar to those found in the pyramidal unit population.

Histology

At the end of the electrophysiology experiments, bats were given a lethal overdose of sodium pentobarbital and perfused transcardially with 200 ml phosphate buffered saline (0.025M, pH = 7.4) followed by 200 ml of fixative (3.7% Formaldehyde in phosphate buffered saline). The microdrive and tetrodes were left in place throughout the perfusion process. Half an hour after the perfusion was complete the tetrodes were fully retracted, the microdrive was removed, and the brain was carefully dissected and stored in the fixative solution for 1-2 days. Following fixation, the brain was transferred to a 30% sucrose solution in PBS for 1-3 days. The brain was sliced into 40 μm coronal sections on a freezing stage using a microtome (HM450, Thermo Fisher Scientific). Following previously described procedures[32] sections were then stained with DAPI, PCP4 and Iba1. Briefly, sections were permeabilized in PBS + 0.3% Triton-X (PBS-X) and incubated in a blocking solution (PBS-X + 10% donkey serum) for 2 hours. The sections were then incubated overnight at 4˚C with primary antibodies (goat anti-Iba1, 1:500 dilution, ab5076 Abcam; rabbit anti-PCP4, 1:500 dilution, HPA005792, Sigma). After primary incubation, the sections were washed in PBS-X and incubated for 120 minutes at room temperature with secondary antibodies (donkey anti-goat Alexa-647, 1:1000 dilution, Invitrogen A32849; donkey anti-rabbit Alexa-488, 1:1000 dilution, Invitrogen A-21206). DAPI (1:10,000 dilution, Thermo Fisher Scientific) was added in the last 10 minutes of secondary incubation.
Sections were washed in PBS-X and cover-slipped using an aqueous mounting medium (ProLong Gold Antifade Mountant, Thermo Fisher Scientific). Fluorescent images of each section around the implant coordinates were acquired using an Axioscan Slide Scanner (Zeiss). The location of the tetrodes used for the analyses were visualized and localized to the dorsal hippocampal area CA1.

Data Analysis

All analyses were conducted using custom code in MATLAB (2022a, MathWorks).

Processing of positional data during task

Preprocessing of bat tracking data and basic analysis of positional features

The positions of all bats recorded by the RTLS were smoothed using local quadratic regression (1 s window). For three out of the four bats, a velocity threshold of 0.5 ms^{-1} was used to segment a bat's session into rest and flight epochs. The fourth bat was tracked exclusively with the marker-based motion capture system (Cortex Motion Analysis), and the same 0.5 ms^{-1} threshold was used to segment the bat's session into rest and flight epochs. To ensure precise capture of flight initiation and landing, flight epochs were manually inspected and trimmed based on the convergence of velocity in x, y, and z directions to zero. Bats tended to rest in a handful of locations, almost exclusively in two upper corners of the room (Supplementary Fig. 14). While in their rest location bats did not typically crawl to different places on the wall. Epochs when the bats were confirmed to be stationary in a preferred rest location were isolated by using a velocity threshold of < 0.4 ms^{-1} and when positional data indicated the bat was < 200 cm from the centroid of a preferred rest location for that session.

Preprocessing of human tracking data and basic analysis of positional features

Positions of humans were tracked with three RTLS tracking tags, one positioned on the right hand (reward delivery hand), one positioned on the left hand (landing pedestal hand), and one in

the right lab coat pocket. Human traverses were identified as follows. A moving median filter (2 s) was applied to the tracking data obtained from the tag in the coat pocket. The beginnings of traverse trials were defined as when the velocity of the human's lab coat tag exceeded the defined threshold (0.4 ms^{-1}), and the human was < 0.1 m from the traverse start position x, y coordinates. The end of traverse trials were defined as > 12 s after the start of a traverse trial, when the velocity of the human's lab coat tag dipped below threshold (0.4 ms^{-1}) and its distance was < 0.3m from the traverse start position x, y coordinates. Data from rare cases where humans paused mid-traverse and the velocity dipped below 0.2 ms^{-1} were discarded. Human velocity was calculated using positional data from the tag in the coat pocket, as it was unaffected by hand and arm acceleration and deceleration (Supplementary Fig. 6). All periods when the human was handling or administering reward were excluded from analysis and were identified as follows. The peaks of accelerometer movement from the tags on the right and left hands were used to identify putative reward initiations (when the humans raised their hands up to deliver reward from a syringe). Reward delivery and bat handling were further verified by manual inspection of video. Timestamps that marked the start/end of handling/reward epoch were buffered with an additional 100 positional samples to ensure no artifactual signal was included in the analysis of human traverses.

Place fields and spatial information

Spatial information in 2D during self-motion

For the analysis of spatial firing fields across all flights, we considered only active cells (n = 259 from four bats), with a minimum firing rate of 0.2 Hz, a minimum of 12 flights, and a minimum of five flights with at least 5 spikes. We focused on the spatial firing in the x, y plane (parallel to the ground), where most of the positional variance was concentrated. To compute 2D spatial firing-rate maps, we projected all positions during flight onto the x, y plane and calculated occupancy-normalized firing rates as follows. We binned the 2D area of the room into spatial bins of a fixed size (0.15 x 0.15 m^2), calculated the time spent in each bin (occupancy), and counted the number of spikes (spike-count) in each bin. We smoothed both the spike-count map and occupancy map with a Gaussian kernel (σ = 1.5 bins) and calculated their ratio, bin by bin, thus obtaining the firing rate per bin. Spatial bins in which the bat spent < 150 ms were invalidated (white pixels in rate maps; e.g. Supplementary Fig. 4c), unless surrounded by at least one valid bin. Spatial information per spike[79] was calculated by summing across all valid bins:

$$SI = \sum_i \frac{p_i \lambda_i}{\lambda} \, log_2 \frac{\lambda_i}{\lambda}$$

Where p_i is the probability of being in bin i, λ_i is the firing rate in the same bin and λ is the average firing rate across all bins. Cells were classified as significantly spatially informative via a shuffling procedure. We compared the empirical value of the spatial information to a spike-shuffled distribution, which was generated by randomly shifting the timestamps of the cell's spike-train circularly relative to behavior (after removing rest epochs), and used to calculate shuffled spatial information. The shuffle procedure was repeated 1000 times for each neuron. Significant place cells were defined as active neurons for which the empirical value of the spatial information exceeded the upper 95% confidence interval of its shuffled distribution.

Spatial information in 1D during self-motion (trajectories)

Many flights that the bats execute are idiosyncratic, repeated paths that emerge as the animal explores the room (Fig. 1b). We took advantage of this behavior and calculated spatial firing maps along tightly confined repeated trajectories. Flights were clustered into trajectories by using an analogous approach to that described previously[31,32,62]. Briefly, all trajectories were spatially down sampled to seven points per flight (first and last points corresponded to the takeoff and landing positions, respectively). The euclidean distance between down-sampled flights was used as a measure of flight similarity, and similar flights were clustered together via agglomerative hierarchical clustering. The linkage distance was set between 1.2 m and 1.4 m for each session, after manual inspection of trajectories. 1D spatial firing fields were calculated for each trajectory and neuron with at least seven flights, a minimum of four flights with spikes, and a minimum of 15 spikes across all flights (n = 247 cells from four bats). To compute the 1D-fields we used a similar procedure to the one for 2D maps, except applied in only one dimension as follows. Flights of each analyzable trajectory were rescaled and binned between takeoff and landing such that each bin's edges were defined by the distance from takeoff along the flight trajectory (bin size = 0.15 m). The amount of time spent in each bin was calculated (1D occupancy map), and the number of spikes in each bin were counted (1D spike-map). The 1D occupancy maps and 1D spike-maps were smoothed with a Gaussian window (7 samples), and spatial information was calculated across 1D-bins as described above. Similarly to what was described for the 2D rate maps, a shuffling procedure was used to assess the significance of the spatial information of each 1D-field. The shuffle distribution of spatial information values was constructed as follows. Each flight in the trajectory was rescaled (as above), the spike train was randomly circularly shifted relative to rescaled position, and the final shuffled spike-map was obtained by counting the number of spikes in each bin across all circularly shifted flights (as above). This shuffled spike-map was smoothed with a Gaussian window (7 samples), and the bin-by-bin ratio of the shuffled spike-map and 1D occupancy map produced the shuffled rate map. This shuffle was repeated 1000 times, and the resulting spatial information values built the distribution to which the empirical spatial information value was compared. Significant 1D-fields were defined as those for which the empirical value of the spatial information exceeded the upper 95% confidence interval of its shuffled distribution, after applying Bonferroni correction for the number of trajectories examined for that neuron. Stability of 1D-fields within a session (Supplementary Fig. 4) was measured by splitting each path into even and odd flights (trials), separately calculating 1D-fields on each half (Supplementary Fig. 4a), and calculating the Spearman correlation between corresponding halves (Supplementary Fig. 4b). Stability of 1D fields within a session across human landing targets was measured by splitting each path into flights to experimenter #1 and flights to experimenter #2, separately calculating 1D-fields on each set of flights (Supplementary Fig. 7a), and calculating the Spearman correlation between corresponding sets (Supplementary Fig. 7b).

<u>Correlation of flights within and across human landing targets</u>

To quantify the similarity of flights of a given trajectory within and across human landing targets, we calculated the Pearson correlation between pairs of flights from trajectories by concatenating x, y, and z coordinates (Fig. 1c). For every trajectory that had at least four repeated flights to each human, we calculated the intra-human and inter-human trajectory correlation as follows. To get the intra-human trajectory correlations we calculated the Pearson correlation of each flight of a given trajectory and human landing target to each other flight of that trajectory

and same human landing target. Correlations from all the human landing target and trajectory combinations were then pooled together. To get the inter-human trajectory correlations we calculated the Pearson correlation of each flight of a given trajectory and human landing target to each other flight of that trajectory to the *other* human landing target. Correlations from all trajectories were then pooled together.

Correlation of traverses between and across humans

To quantify the similarity of human traverses, we calculated the Pearson correlation between the concatenated x and y coordinates of pairs of traverses (Fig. 2c). To obtain a measure of similarity between traverses executed by one human, we calculated the Pearson correlation of all traverses one human performed to all other traverses that same human performed. To quantify the similarity of traverses across humans we calculated the Pearson correlation of each traverse one human performed to each other traverse that the other human performed. We quantified the similarity of the velocity profiles across humans by calculating the Pearson correlation of the velocity profiles (concatenated x, y, and z velocity) for one human's traverses to the velocity profiles of the other human's traverses (Supplementary Fig. 15).

Effect of the experimenter identity on firing modulation of hippocampal neurons in flying bats

To quantify if a neuron was significantly modulated by the identity of the human at the landing/takeoff location we calculated the difference in mean firing rate of flights that ended/started in the same location, but with different humans standing at that location. Inspection of the peak-normalized sorted plot of 1D place fields suggested that peak activity clustered around takeoff and landing (Supplementary Fig. 4a), so we chose a 2 s window at takeoff (-1.75 to +0.25 s) or at landing (-0.25 to + 1.75 s) to calculate the mean difference in firing rate. To determine if a cell was significantly modulated by the identity of the human landing target at a given landing location, we performed a permutation test as follows (this process was then done for all takeoff locations). For each landing location that had at least four trials to each human, 15 spikes across all trials in the landing time window, and at least four flights with spikes in the landing time window, we calculated the difference in mean firing rates obtained in the landing time window to each human. We then constructed a shuffled distribution of mean firing rate differences by shuffling the label of which human was the landing target for each trial, and taking the difference in mean firing rates of two subsets of the shuffled-label data with equal sizes to the empirical data. The shuffling was performed 1000 times, or for as many permutations as the number of trials per human permitted (maximum permissible permutation test resolution for inclusion was $p = 0.02$). Neurons were significantly modulated by the human landing target if the empirical value of the difference in mean firing rates exceeded the upper 95% confidence interval of the shuffled distribution, Bonferroni corrected for the number of landing/takeoff locations examined. For the analysis where we explicitly excluded any flights where the other bat in the room was present at landing, we performed the same procedure as above but only for landing locations where the inclusion criterion was met after excluding all trials when the other bat was at the landing location. The other bat was classified as present at a landing location if the Euclidean distance of the other bat's position to the coordinates of the tripod at that location was < 200 cm and the bat's velocity dipped below the flight detection threshold (0.4 ms^{-1}).

Effect of the presence of the other conspecific at landing on firing rate during flight

To quantify if a neuron was significantly modulated by the presence of the other conspecific at the landing location, we used a permutation test as was done above for the human landing target. We calculated the difference in mean firing rate in the window at landing (-0.25 to +1.75 s aligned to landing) between flights to the same locations where the other conspecific was either present or absent. We compared this empirical value to a shuffled distribution obtained by permutation test, shuffling the labels of whether the conspecific was absent or present at landing. Neurons were significantly modulated by the presence of the conspecific at landing if the empirical value of the difference in mean firing rates exceeded the upper 95% confidence interval of the shuffled distribution, after applying Bonferroni correction for the number of landing locations examined for that neuron. We classified the other bat as present at a landing location in the same manner as described above.

Spatial information for the position of the other bat in the room during recorded bat rest

To assess whether neurons carried significant spatial information about the position of the other bat in the room, we calculated the spatial information of 1D rate maps using the neural data of the stationary recorded bat and the 1D occupancy maps of trajectories (linearized and binned, described above) executed by the conspecific. We clustered the flights of the conspecific into trajectories using the agglomerative hierarchical clustering method (see above). We then excluded any flights from analysis where the recording bat was not in a preferred resting location. The recording bat was confirmed to be in a preferred rest location if velocity was below a threshold of 0.4 ms^{-1} and the Euclidean distance of the bat to the centroid of the preferred resting location was < 200 cm. Preferred resting locations were determined by k-means clustering all positional data where the velocity threshold dipped below 0.4 ms^{-1} and taking the centroids of the resulting clusters. Spatial firing was calculated for each conspecific trajectory and recording bat neuron where there were at least 7 flights, a minimum of four flights with spikes, and a minimum of 15 spikes across all flights (n = 130 cells from four bats). We computed the 1D rate maps in the same manner as the self-motion 1D trajectories above and applied a Bonferroni correction for the number of trajectories examined for that neuron. Significance of spatial information was assessed by comparing the empirical value to a shuffled distribution. The shuffled distribution was constructed in the same manner as above described for the shuffled distribution of the 1D rate maps.

Spatial information for human position during human movement and recorded bat rest

To assess whether neurons carried significant spatial information about the position of the humans in the room, we performed an analysis similar to the one for assessing 2D spatial information described above. First, we asked if neurons from the stationary recorded bat carried significant spatial information for the position of any human during the stereotyped traverse to and away from the bats hanging in a preferred rest location. During experiment #2 only one human was ever moving at a time, and we included all times where a human was moving, but was not handling or administering reward (see above for how human traverses were defined). We also excluded any times when the recorded bat was not in the preferred resting location (see above for how a bat was determined to be at a preferred resting location). Rate maps were calculated from the human 2D occupancy map and recorded bat spike data. Only sessions with at least six human traverses, at least four traverses with spikes, and at least 15 spikes over all traverses were included in the analysis. We projected all human positional data onto the x, y plane, binned the positional samples into 0.15 x 0.15 m^2 bins, and calculated the amount of time spent in each bin (occupancy map). We then counted the number of spikes from the recorded bat

that occurred in each bin to obtain the spike-map. We smoothed both the spike-map and occupancy map with a Gaussian kernel (σ = 1.5 bins) and calculated their ratio, bin by bin, thus obtaining the firing rate per bin. Spatial bins where the human spent < 1 s were invalidated (white bin in rate maps), unless surrounded by at least one valid bin. Spatial information was calculated from the 2D firing rate map and compared to a shuffled distribution. The shuffled distribution was obtained by circularly shifting the spike train of the recorded bat relative to human movement (with periods between traverses removed), counting the number of spikes in each spatial bin (shuffled spike-map), computing the bin-by-bin ratio of the shuffled spike-map to the 2D occupancy map (shuffled rate-map), and calculating the spatial information from that shuffled 2D rate map. Neurons carried significant spatial information for human movement if the empirical value of the spatial information exceeded the upper 95% confidence interval of its shuffled distribution. To assess spatial information for each human's movement independently, we performed the same analysis as above but with occupancy maps for traverses of either experimenter #1, or experimenter #2, Bonferroni corrected for the number of experimenters examined per neuron (Fig. 2e). Only traverses with at least six trials for a given human, at least four trials with spikes, and 15 spikes total across all traverses were included in the analysis. For all neurons that carried significant spatial information for just one human, we compared the normalized spatial information for the human for which spatial information was significant (preferred human) to the normalized spatial information of the other human (non-preferred human) (Wilcoxon signed rank test, n = 43 neurons, $p = 1.1 \times 10^{-8}$; Fig. 2f). Normalized spatial information is the empirical spatial information divided by the mean of the spatial information values calculated from spike shuffled trials[80]. Then, for each neuron we compared the normalized spatial information value to the normalized spatial information value calculated from the rate map that excluded all epochs where the other conspecific was flying (Wilcoxon signed rank test; n = 43 neurons, $p = 0.44$; Supplementary Fig. 16b). Flight epochs were determined using the method described above for identifying periods of flight in the bats.

Conjunctive code for space and experimenter identity during self-motion

To quantify the extent to which neurons significantly modulated their activity during flight depending on the human landing target at multiple different locations in the room, we first identified which neurons had at least four locations with enough flights to/from each human to be analyzed. We then counted the number of locations for which each neuron significantly modulated its activity depending on the identity of the human (Fig. 1g). Then, to quantify how factors of human identity and location contributed to the firing rate of a neuron at landing, we used a simple linear model to predict the mean firing rate around landing by using three predictors: a non-ordinal categorical variable encoding the identity of the human at landing, a non-ordinal categorial variable encoding the landing location, and their interaction term (*lmfit* Matlab; Supplementary Fig. 9a). The landing location categorical variable is the assigned number of the tripod the bat landed at. This was determined by calculating the Euclidean distance of the bat's position at the end of each rewarded flight to every possible tripod landing location (1-4) and taking the tripod with the minimum distance. Model comparison was performed to identify, for each neuron, which variables significantly improved the prediction of firing rate upon landing (*anova* Matlab, significance threshold $p < 0.05$). This model allowed us to disambiguate a purely additive coding for human and location from a conjunctive coding of human and location. In total 134 neurons were modeled, and 7 neurons were not included in further analysis because there were no significant variables that improved prediction of firing rate at landing (n = 127

neurons). Each neuron was classified as 'additive', 'conjunctive', 'human only', or 'location only'. 'Additive' neurons had significant Human and Location variables, but not significant interaction terms. 'Conjunctive' neurons had significant Human and/or Location terms, as well as a significant interaction term. 'Human only' neurons had a significant Human term, but not significant Location or interaction terms. 'Location only' neurons had a significant Location term, but not significant Human or interaction terms. We then compared these results to those obtained via permutation test classifying a neuron as modulated by the human identity upon takeoff/landing (see above; Supplementary Fig. 9b).

Effect of the reward quantity on unit modulation at landing

To examine whether there was a global effect of reward quantity on neural responses around landing on different human targets, we calculated the peak firing rate change around landing, the mean firing rate change immediately upon landing (0 to +1.75 landing at 0), and the Spearman correlation between average firing rates to different human landing targets for a given unit and landing location (Supplementary Fig. 13). Peak firing rate change was calculated by dividing the peak firing rate in the same window as used previously (-0.25 to +1.75 around landing) by that unit's baseline firing rate. Mean firing rate change was calculated by dividing the mean firing rate in the window immediately after landing by that unit's baseline firing rate. We used the same inclusion criteria as in previous analyses, including only units x landing locations x humans with at least four flights with spikes and at least 15 spikes across all flights.

Remapping analysis

Remapping on specific trajectories

We calculated the correlation, distance between peaks, and remapping scores for the 1D linearized rate maps of a given trajectory to different human landing targets (Supplementary Fig. 6). For a pair (trajectory x unit) to be included in the analysis it had to meet the same criteria as for examining 1D spatial information above (at least four flights with spikes, at least 15 spikes across all flights), and had to carry significant 1D spatial information. Linearized rate maps were computed in the same manner as described for calculating 1D spatial information above. The correlation was the Pearson correlation between 1D rate maps to different human landing targets. The distance between peaks was the distance between maximum values of the linearized rate maps. The remapping score was calculated as follows[81]: for a given unit and trajectory we obtained the mean firing rates during the 1D linearized rate maps to different human landing targets; the score was defined as the unsigned difference between those rates, divided by their sum. A score of 0 indicates no rate change, while a score of 1 indicates that one rate value dominates the other. The empirical distributions of the correlation, distance between peaks, and remapping scores were compared to their respective null distributions, which were constructed as follows. The null correlations were calculated by taking the Pearson correlation between 1D linearized rate maps of non-paired units (one per unit) for a given trajectory to different human landing targets. The null distance between peaks measure was calculated by taking the distance between maximum values of the linearized rate maps of non-paired units for a given trajectory to different human landing targets. The null remapping score was calculated by shuffling the human landing target labels between flights of a given trajectory and calculating the rate maps for paired units across the trial-shuffled rate maps. It is important to note that the remapping score null distribution represents no rate remapping, as the trials are randomly chosen across human landing targets. On the contrary, the correlation and distance between peaks null distributions

represent global remapping, as they compare the rate maps of non-paired units (random movement of place fields). If the spatial profile of the responses to different experimenters is much more similar (high correlation, low distance between peaks) than those predicted by global remapping, this suggests the absence of global remapping. If the difference in firing rates (remapping score) is significantly higher than predicted by the null hypothesis, this suggests a phenomenon resembling rate remapping.

Remapping on 2D rate maps between contexts

Classical remapping analyses compare the rate maps across contexts in an experiment. In the present study humans stood at alternating locations in the room for extended periods of time, creating "contexts" where the humans were standing in a given configuration (i.e. context 1 is experimenter #1 at location A and experimenter #2 at location B, while context 2 is experimenter #1 at location B and experimenter #2 at location A; Supplementary Fig. 6). To compute remapping metrics across these contexts, we defined a context as all the occupancy and spikes that occurred when the humans were standing in a given configuration in the room. If there were multiple contexts in which sufficient flights and spikes occurred, the top two contexts with the most occupancy were used. For a pair (unit x contexts) to be included, the fraction of pixels shared between the two contexts' rate maps had to be at least 0.3, there had to be at least 20 spikes total within a context, and the unit had to carry significant spatial information. The 2D rate maps for each context were computed as described above in the section detailing 2D rate map calculation. The correlation, distance between rate map centroids, and remapping scores were then computed between rate maps. The remapping score was calculated similarly to the 1D case, dividing the unsigned difference in mean firing rates of the 2D rate maps by their sum. The center of mass movement was the euclidean distance between the center of mass of each rate map, as identified by the Matlab *regionprops* function. The correlation was simply the Pearson correlation between rate maps. The null distributions for correlation and center of mass movement were constructed similarly to the 1D case, by taking the correlation or distance between centers of mass between two rate maps of non-paired units (one per unit) from each context. The null distribution for the remapping score was also constructed similarly to the 1D case: a random subset of flights from each context was used to construct the rate maps and the remapping score was computed across trial-shuffled maps for paired units. As explained for the remapping analysis on specific trajectories, the remapping score null distribution represents no rate remapping, whereas the correlation and distance between peaks null distributions represent the presence of global remapping.

Temporal stability of human modulated units

To determine if the modulation associated with the human landing target was present from the first trial or emerged as the session progressed, we calculated the correlation between mean firing rates of the first and second halves of flights along each 1D linearized trajectory to a given human (Supplementary Fig. 8). This distribution of correlations was compared to a null distribution constructed from the correlation between randomly chosen subsets of flights from that trajectory and human. The null represents what would be expected if the modulation were present from the first trial and did not evolve over time.

Statistical Analysis

No formal methods were applied to predetermine sample sizes and adopted sample sizes were similar to those used by similar studies. No randomization of experimental sessions was performed and no blinding to experimental conditions was implemented during the analysis. All statistical comparisons were performed using nonparametric tests (Permutation test, Wilcoxon signed rank test, Kolmogorov-Smirnov, or bootstrap tests) unless otherwise stated. The tests were two-tailed. Where appropriate, adjustments for multiple comparisons were performed using the Bonferroni correction.

5.2 Supplementary materials and methods for Chapter 3

Subjects, experimental design, and behavioral tasks

Imaging data were collected from the hippocampal dorsal CA1 area of $n = 7$ adult (2-3 years old) male, laboratory born Egyptian fruit bats (*Rousettus aegyptiacus*; ~ 160 gr weight) engaged in aerial spatial foraging[61]. Prior to the experiments, bats were housed in a large, environmentally enriched colony room where they were able to fly freely and socialize. Bats were naive to the experimental flight room prior to the start of flight experiment training[61]. When not in the flight room, experimental animals were socially housed in cages (31 cm x 36 cm x 45 cm or 47 cm x 77 cm x 93 cm) in a separate communal housing room. The lights in the housing room were maintained on a 12-hour reverse light cycle (lights on/lights off; 7 am/7 pm). All flight experiments were performed at the same time of day during their awake hours (dark cycle). All experimental procedures were approved by the Institutional Animal Care and Use Committee of the University of California, Berkeley.

All experiments were performed in an acoustically, electrically and RF- shielded room (5.6 m x 5.2 m x 2.5 m) with high precision lighting control[61]. The flight room walls and ceiling were covered with black acoustic foam to dampen noise from outside of the experimental room and reduce acoustic reverberation. An additional layer of acoustically absorbing black felt was used to protect the acoustic foam from being damaged by the bats while maintaining the intended acoustic environment[61,62]. The flight room floor was also covered with the same acoustically absorbing black felt. The 3D spatial position of the bat was tracked at millimeter resolution using 16 motion capture cameras (Raptor-12HS) distributed across the ceiling (Motion Analysis, CA), as described previously[61]. Each camera tracked six to eight reflective markers that were attached to the wireless microscope cover carried by the bat and the video was sampled at a frame rate of 120 Hz. The 3D position of the marker set was computed and saved using a proprietary commercially available software specifically designed for the motion tracking hardware (Cortex-64; Motion Analysis, CA). Marker positions were processed with custom-written Matlab (MathWorks, MA) functions as previously described[61]. Finally, the resulting tracking data was smoothed by 10 samples (83ms). Calibration of the video tracking system was done daily (using the calibration wand and by placing 14 reflective markers on the same reference places) prior to each recording session in order to assure reliable reconstruction accuracy of 3D position and day-to-day registration of the coordinate system.

Foraging experiment

The foraging experiment consisted of three sessions: pre-behavioral rest (5 min), foraging (~ 50

min), and post-behavioral rest (5 min). For all experiments, bats were food restricted to no less than 80% of their baseline body weight to motivate their foraging behavior during the experiments. Neural activity was imaged continuously during all sessions and the bat remained in the flight room for the entire duration of the experiment. During the pre-behavioral rest session, the bat was kept in a small cage (25 cm x 32 cm x 46 cm) within an opaque enclosure (40 cm x 46 cm x 65 cm) inside the flight room. After the pre-behavioral rest session, the bat was taken out of the enclosure, released from the cage and allowed to forage freely from the feeders. This was followed by the post-behavioral rest session, which was performed in the same manner as the pre-behavioral rest session.

Details of the basic behavioral experimental setup have been described previously[61]. Four automated feeders were placed on the wall at one end of the room, with two on each side of the wall (Fig. 3d). Two of the feeders (one each on the far sides of the wall) were active during the behavioral sessions (Fig. 3d). Each feeder had an infrared beam break sensor to detect when a bat landed on the feeder and a motor driven reward system that administered a pureed fruit (~ 0.3 ml/reward). The feeders were all independently controlled by an Arduino (Uno Rev3) and Adafruit Motorshield (1438; Adafruit, NY) interfaced with a computer placed outside of the experimental room. Positional tracking (Motion analysis, CA) was used to monitor crossings of a virtual 2D boundary four meters away from the feeders. The bat was required to fly across the virtual boundary in order to bait the feeders. Once the bat received reward at a feeder, that feeder was deactivated to encourage the bat to cross the invisible boundary and re-bait the feeders. Bats could return to any feeder after re-baiting. Our dataset was collected when bats were experienced in flying for reward in the flight room (after at least five to ten foraging sessions in this environment) and had begun to reliably and spontaneously fly repeated flights. On average, bats flew 76 $\pm$ 20 flights per session, which yielded a total of 4,731 flights. 73.4% of all flights (3,472 of 4,731) occurred along repeated flight paths.

Lights-on vs. lights-off foraging experiment

Two of the seven bats also participated in the lights-on:lights-off:lights-on' foraging experiment. These experiments were similar to those described above but consisted of five sessions: pre-behavioral rest (5 min), lights-on foraging (20 min), lights-off foraging (20 min), lights-on foraging' (20 min) and post-behavioral rest (5 min). Egyptian fruit bats can alternate between two sensory modalities that enable high resolution distal sensing: echolocation when flying in the dark[82–84] and vision when navigating in light[85,86]. Calcium responses were recorded continuously and the bat remained in the flight room throughout the entire experiment without disruption from the experimenters. As described above, the bat was kept in a small cage (25 cm x 32 cm x 46 cm) within an opaque enclosure (40 cm x 46 cm x 65 cm) inside the flight room during all the pre- and post-behavioral sessions. After the pre-behavioral rest session, the bat was released into the room to begin the self-directed foraging task with the room light panels turned on (4.95 $\pm$ 0.07 lux; mean $\pm$ SD; measured at the floor level in the center of the room using ILT-1700 illuminance meter; International Light, MA). Automated lighting was controlled using arrays of ceiling-mounted LEDs (5% Lumos; C3 Lighting, CA) with a timer (Q Light Controller+) that turned off the lights (0.08 $\pm$ 0.02 lux; mean $\pm$ SD; residual light from the near-IR [750 nm peak] positional tracking system) for the lights-off portion of the experiments and turned them back on to the same lighting levels for the second iteration of the lights-on portion of the session.

Microscope design

We used a custom miniature microscope (miniscope) made of 3D printed material (black resin; Formlabs, MA) (Fig 3a)[60] similar to previously described designs[15,87–89]. This microscope is open source and the design files, part numbers and software are publicly available: https://github.com/gardner-lab/FinchScope and https://github.com/gardner-lab/video-capture. In brief, a blue LED produced excitation light (470 nm peak; LUXEON Rebel). A drum lens (#45-549; Edmund Optics) collected the LED emission, which passed through an excitation filter (3.5 mm X 4 mm x 1 mm, ET470/40x; Chroma), deflected off a dichroic mirror (4 mm x 6 mm x 1 mm, T495lpxr; Chroma) and entered the imaging pathway via a ~ 0.25 pitch gradient refractive index (GRIN) objective lens (GT-IFRL-200; GRINTech, Germany). Fluorescence from the sample returned through the objective, the dichroic, an emission filter (4 mm x 4 mm x 1 mm, ET525/50m; Chroma) and an achromatic doublet lens (#45-207; Edmund Optics) that focused the image onto an analog CMOS sensor with 640 × 480 pixels (MB001; 3rd Eye CCTV). The frame rate of the camera was 30 Hz and the field of view was approximately 700 μm along the diagonal axis. Video was broadcast at ~ 2.37 GHz via a wireless transmitter (TX24019, 100 mW). The entire system was powered with a lightweight consumer grade 3.7 V, 300 mAh Lithium Polymer (LiPo) battery, which provided stable recording for over an hour at average imaging LED intensities (< 100 μW post-objective power). The NTSC video and a synchronization signal were both digitized through a USB frame grabber. Custom software written in the Swift programming language running on the macOS operating system (version 10.10) leveraged native AVFoundation frameworks to communicate with the USB frame grabber and capture the synchronized analog video stream. The video and sync signals were written to disk in MPEG-4 container files. The video was encoded at full resolution using either H.264 or lossless MJPEG Open DML codecs and the sync signal was encoded using the AAC codec with a 48 kHz sampling rate.

Surgical Procedure

General surgical and anesthesia procedures were similar to those previously described for Egyptian fruit bats[33,62] and the GRIN lens implant procedure was adopted from work in rodents[89,90]. Analgesics were given for three days after surgery and antibiotics were given for one week after surgery.

Anesthesia for all procedures was induced with a subcutaneous injection cocktail of ketamine, dexmedetomidine and midazolam. The bat was then placed in a stereotax (Model 942; Kopf, CA) where the level of anesthesia was monitored by toe pinch reflex and breathing rate. A rectal probe measured the bat's body temperature continuously and a heating pad was used to maintain the bat's body temperature stable at ~ 34.5 °C. Anesthesia was maintained throughout surgery by successive injections (roughly once per hour) of an anesthesia maintenance cocktail consisting of dexmedetomidine, midazolam and fentanyl. Lactated Ringer's solution was subcutaneously administered to maintain hydration.

While the bat was under anesthesia, the skull was exposed and cleaned, and the surrounding skin and tissue was retracted. The coordinates above dorsal CA1 (dCA1) were measured on the outside of the skull from a common reference point at the confluence of sinus. A circular craniotomy (1.2 mm diameter) was made through the skull over the left hemisphere. The center of the craniotomy was positioned 5.8 mm anterior to the transverse sinus that runs between the posterior part of the cortex and the cerebellum, and 2.8 mm lateral to the midline. The brain surface

was exposed but the dura was left intact. A NanoFil syringe (36 GA beveled needle; WPI, FL) was attached to the stereotax and slowly lowered into the dorsal CA1. After waiting for three minutes, 1.2 µL of pAAV9.hSyn.GCaMP6f.WPRE.SV40 was injected (titer 1.40e+13, Lot# 100837; V20744; Addgene, MA) at a rate of 4 nl/sec using a microinjection pump (UMP3; WPI, FL). Genetic expression driven by the hSYN promoter has been shown to express in both excitatory and inhibitory neural cell types in the mammalian hippocampus[91]. Five to ten minutes after completing the injection, the needle was slowly retracted out of the brain. The craniotomy was then filled with a biocompatible elastomer (Kwik-Sil; WPI, FL) and the tissue was closed with sutures.

One week after the injection, the bat was placed under anesthesia using the same procedures for the lens implantation procedure. The skin was retracted in the same manner as the injection surgery to re-expose the craniotomy and the biocompatible elastomer was removed from craniotomy. A GRIN lens (1 mm diameter x 9 mm height, 0.5 pitch; 1050-002177; Inscopix, CA) was placed inside the same craniotomy directly dorsal to CA1. The surface of the skull was carefully cleaned and scored to facilitate cement bonding to the skull. Three bone screws (19010-00; FST, CA) were inserted into the skull to provide anchor points for the cement. A thin layer of bone cement (C&B Metabond; Parkell, NY) was applied onto the surface of the skull and around the base of the bone screws. Kwik-Sil was then removed from the craniotomy to expose the brain surface. The cortex above dorsal CA1 was aspirated using a vacuum pump attached to a 30 GA blunt needle. Ice cold sterile lactated ringer solution along with pressure from an absorbable sponge (Gelfoam; Pfizer, NY) was applied to the brain to prevent bleeding during the aspiration. Aspiration continued slowly until the parallel fibers of the hippocampal oriens were visually identified. The relay GRIN lens was held by a custom-built 3D printed lens holder attached to a vacuum pump. The lens was slowly lowered and positioned dorsal to the CA1 region of the hippocampus (~ 2.5 mm below the surface of the brain). After implanting the lens, Kwik-Sil was applied to the base of the craniotomy to protect the brain at the interface of the lens and the skull. Carbon powder was mixed with dental acrylic to create an opaque black acrylic that was applied around the surface of the skull and above the bone screws to hold the implanted lens in place. The top of the GRIN lens was covered with Kwik-Sil elastomer and a small plastic cap to protect it from mechanical damage while the bat recovered.

Two to three weeks after lens implantation, the miniaturized microscope was aligned with the GRIN lens. While under anesthesia, the Kwik-Sil elastomer protection was removed from the relay lens and the surface of the lens was cleaned with 70% ethanol. A cable from the imaging DAQ was attached above the CMOS to control the LED power and stream video data, which was acquired using custom video capture software (https://github.com/gardner-lab/video-capture)[60]. The miniscope was attached to a stereotax arm using a custom CNC machined clamp and moved above the implanted relay lens to find the best field of view with the maximal number of fluorescent cells visible. In order to account for the settling of the dental acrylic after drying, the miniscope was raised approximately 50 µm above the ideal focal plane before anchoring it above the relay lens with the dental acrylic. A custom 3D printed protective housing case was optically glued (Flow-It ALC; Pentron, CA) onto the 3D printed protective base cone. One to three days after attachment, the miniscope was focused to an optimal field of view (by rotating the CMOS along the threaded exterior of the microscope body) and secured to the protective case with a thick layer of optical glue to prevent any further movement for the rest of the experiment.

Histology

At the end of the experiment, bats were administered an overdose of pentobarbital and perfused transcardially using a flush of 250 ml of phosphate buffered saline (PBS, pH 7.4) spiked with 0.5 ml heparin (1,000 USP units/ml) followed by 250 ml of fixative (3.7% formaldehyde in PBS). The brain was carefully removed and post-fixed overnight in the same fixative. To avoid over-fixation, the brain was moved after 24 hours from the fixative into a 30% sucrose solution for cryoprotection. After approximately two days, or once the brain had sunk to the bottom of the solution, 40 μm coronal sections were made using a microtome (HM450; Thermo Fisher Scientific, MA) with a freezing stage. The sections were floated in PBS, stained for DAPI ([1:10,000]; Thermo Fisher Scientific, MA) and cover-slipped with aqueous mounting medium (ProLong Gold Antifade Mountant; Thermo Fisher Scientific, MA). Fluorescent images of each section surrounding the implant were taken using an Axioscan Slide Scanner (Zeiss, Germany). Subsequently, these images were used to identify GCaMP6f-labeled cells and verify lens implant location above dCA1.

Data analysis

All analyses were conducted using custom code in Matlab (MathWorks, MA), which can be found online: https://github.com/WALIII/ImBat.

Flight segregation and behavioral analysis

Position coordinate vectors (X, Y and Z of the center of mass of the markers on the head) for each bat were concatenated across sessions and flight was identified via a velocity threshold of 0.2 m/s. As in other bat species, many flights followed along the same paths[92]. Similar flight paths were typically traversed in only one direction. Flights were clustered into paths via agglomerative hierarchical clustering, where flight trajectories were downsampled to six points per flight (first and last points corresponded to the take-off and landing positions, respectively). Intermediate points were calculated through spline interpolation. 18-dimensional (6 *x* 3D) vectors representing different flights were clustered into 'paths' according to their Euclidean distance using the linkage and cluster functions in Matlab. The linkage distance was set to 1.2 m after manual inspection of flight groupings and we enforced a minimum of three flights per cluster across all sessions. All of the remaining flights that did not belong to a path cluster were considered 'unique,' which accounted for 26.6% (1,259 of 4,731) of all flights. Flight tuning stability was determined by taking all flights from the same path and comparing the mean 1D correlation of the X, Y and Z positions, aligned to takeoff, to their respective mean path on the first session.

Artifact rejection, motion correction

Raw video frames from the wireless microscope were acquired at 30 frames per second and then spatially downsampled by a factor of two. Wireless transmission artifacts impacted individual frames and were detected by taking the standard deviation of the detrended time series vector of the median intensity of all pixels on the boundary (first and last rows and columns) of each frame. Values that exceeded 2x SD were treated as dropped frames, which comprised <0.01% of all frames. Data was then motion corrected using subpixel image registration[93] and temporally median filtered by four frames. Periodic clock pulses generated by a Master-9 device (A.M.P.I; Israel) were used to create a timing signature that served as a common frame of reference for the flight tracking system and the microscope recording software in order to align and synchronize the

motion tracking and the imaging systems offline[60,62].

Region of interest segmentation and multi-day alignment

Region of interest (ROI) identification, segmentation and alignment across days was performed similarly to previously published approaches[15,17,88,94–96] and are therefore briefly described below. To detect regions of interest corresponding to putative neurons, we used an adaptation of a constrained non-negative matrix factorization approach designed for single photon calcium imaging data (CNMF-E)[95,96]. This approach identifies, detrends and removes an estimate of the local fluctuating background from each ROI. The following parameters were used for all bats on all days: mean subtracted 2D gaussian smoothing kernel (gSig) = 8 μm, maximum soma diameter (gSiz) = 34 μm, minimum pixel-to-noise ratio for seeding a neuron (PNR) = 2.5, minimum local correlation = 0.85. A ring model was used to estimate a background signal for each neuron (ring_radius = 46 μm). Calcium traces were deconvolved using an autoregressive model (OASIS) with order p = 1 and using the 'constrained' method, which gives a frame-resolution (33 ms at 30 fps) timing estimation of the underlying spiking-related burst event[94,97]. Finally, identified ROIs were manually inspected to remove duplicates and inappropriate merges.

ROI alignment across days was performed using a combination of statistically driven and supervised approaches. Tracking confidence can be influenced by a number of factors such as damage or replacement of the microscope, experimenter refocusing or slow drift of the field of view (FOV) associated with day-to-day brain movement. Given the possibility that methodologically driven tracking instability can be conflated with biologically driven tuning instability, we only considered adjacent sessions where manual inspection indicated that the imaging plane was highly stable. This involved evaluating the consistency of anatomical features such as blood vessels, as well as static persistent features with high fluorescence background such as neuropil. After this assessment is satisfied, we then evaluate the sharpness and consistency of the constellation of cells in a max projection image for blurriness or lateral displacement which also serve to indicate a change in imaging focal plane.

Once stable adjacent FOVs were manually verified, CNMF-E identified ROI spatial footprints were aligned across days using a previously published algorithm (CellReg)[96]. After rigid registration of ROI masks across days, this approach uses a combination of spatial correlation of ROI spatial footprints and the distance between ROI centroids to build a distribution of potentially same or different cell pairs within a radius of 10 μm. These cell pairs do not need to be on adjacent days. We further restricted our analysis to CNMF-E identified ROIs that could be unambiguously identified in at least two independent, but not necessarily consecutive, sessions in order to further guarantee that cells we could not confidently track were not attributed to biological tuning instability. This restriction criteria almost exclusively removed ambiguous ROIs that were either very low signal to noise (SNR) or at the very edges of the field of view. Nevertheless, cells that fired extremely rarely (i.e., in only a few sessions out of the whole experiment) were still included and assessed in our analysis.

In addition, we performed a manual annotation of ROIs from the full session maximum projections. This serves as an alternative approach to evaluating neural activity per session in a way that is independent of the deconvolution ability of CNMF-E or CellReg's registration accuracy across days. Given that our viral expression is sparse, our data contains numerous examples of well isolated, high SNR neurons within a region of 50 – 100 μm^2. We can leverage this sparsity to independently estimate the proportion of cells that are unambiguously transient from one day to the next (i.e., where ROI tracking was abruptly lost or gained over an adjacent session, due to a

complete loss or gain of both flight tuning and spontaneous activity). This analysis is predicated on the fact that cells that are most easily and unambiguously identified on any day should occur equally likely to drop in/out compared to low SNR cells (which are more susceptible to methodological issues). Considering a subset of 36 flight sessions with the clearest maximum intensity projections, we were able to identify only a few rare examples of drop-in/out in high SNR ROIs over a single day relative to nearby ROIs (Supplementary Fig. 23). Specifically, out of 1,038 hand labeled, clearly identified regions of interest, we found that the majority (97.4%; 1,011/1,038) corresponded to a set of unique pairs that were clearly visible on adjacent sessions. Of the remaining 2.6%, we find that 1.15% (12/1,038) visibly 'drop-in' and 0.87% (9/1,038) visibly 'drop-out' from one session to the next, and an additional 0.57% (6/1,038) are 'transient' (i.e., they are not active on the proceeding or following session). This finding is consistent with previous studies in mice which find that most cells in the hippocampus are active on most days and neural tracking is predominantly limited by imaging plane instability rather than by previously active cells falling completely silent[17]. Likewise, the majority of our tracking loss across days occurs when the sharpness and intensity of a well-isolated ROI slowly fades over time, which is best explained by residual day-to-day plane instability. We estimated the discrete tracking loss (from the initial identification to the point where an ROI can no longer be detected or confidently matched on an adjacent session) to be about 2% of CNMF-E identified ROIs per day under ideal conditions where there is no noticeable change in the stability in the imaging plane (Supplementary Fig. 22a). Our final imaging data set consisted of 63 daily sessions from seven bats (9 ± 3 sessions per bat), with 562 unique regions of interest (i.e., ROIs that we believe to be independent and confidently tracked for at least one session). The numbers of unique ROIs imaged from each of the seven bats were 101, 187, 20, 70, 39, 101 and 44 (see Supplementary Fig. 22a-b for tracking statistics of ROIs used in this dataset). In the two bats tested in the alternating lights-on vs lights-off foraging experiment, a total of 131 unique ROIs (59 and 72 ROIs from bat #1 and bat #2, respectively) were imaged across 2,313 total flights (mean of ~ 152 and 79 flights/day, respectively) for 10 consecutive days each.

Region of interest significance and stability

Significance of flight path tuning for each ROI was determined by comparing the 1D *Spatial Information* ('inferred spikes'/sec) of the mean path-aligned deconvolved neural activity for any paths with at least 10 flights. Flight-aligned neural activity was concatenated across sessions in which ROIs were reliably detected and aligned. To calculate spatial information, we used the following equation derived from mutual information[33,79]

$$SI = \sum_i p_i (r_i/r)\, log_2(r_i/r)$$

where p_i is the probability of the animal to be in the i^{th} time-bin (relative to flight takeoff) and r_i is the 'deconvolved' firing rate of the neuron in the i^{th} voxel. Here, r is the average firing rate computed as:

$$r = \sum_i p_i r_i$$

Significance was determined by comparing the observed SI value to a shuffled distribution (1000 shuffles per ROI), which was computed by circularly shifting the burst event time by a random amount for each path-aligned flight. To calculate significance during flight, we circularly shuffled only the periods of flight. Bonferroni correction was used for each neuron based on the total

number of flight paths considered in order to correct for multiple comparisons. An ROI was considered 'flight-tuned' if its activity contained significantly more information than chance ($p < 0.05$ after correcting for multiple comparisons) during flight for any of the three most common flight paths. For all significantly tuned ROIs, tuning stability across days was determined by taking the Pearson correlation of the mean flight-aligned ROI $\Delta f/f_0$ time series either across days (e.g., Fig. 4b) or across lights-on and lights-off conditions.

To calculate neural variability (e.g., Supplementary Fig. 24a-b), we first obtained the peak of the mean, flight path-aligned, deconvolved time series for all significantly flight tuned ROIs. To account for multiple firing fields per flight path, in this analysis we also considered peaks during flight that were separated by at least one second and had a prominence that exceeded 1.5x SD (standard deviation of the mean time series over the entire session). We then took the distribution of intensity values at these peak times across all flight-aligned, smoothed (by three frames, i.e., ~ 100 ms), deconvolved neural activity traces for the three most common flight paths, as long as they contained at least ten flights on any given session. Finally, we calculated the coefficient of variation (CoV) of this distribution. To calculate flight position variability, we took the X, Y, and Z positional coordinates at the peak times identified in the neural time series, and then computed the Euclidian distance to the mean X, Y, and Z coordinate for the corresponding flight path. Next, we compared neural activity variability (normalized CoV of neural activity over flights) to flight variability (i.e., the mean Euclidian distance of the points in space when a neuron was active, relative to the mean flight path) for every firing field and flight path pair.

Some flight paths are composed of behavior that is more variable from flight to flight. We reasoned that tuning fields would appear to be less stable for flight paths with greater behavioral variability because of a decrease in spatial specificity and repeatability from flight to flight, which will compromise our ability to measure the tuning fields. For ROIs that were significantly tuned to more than one flight path, we compared the difference in the distributions of ROI stability for the firing field for more vs. less variable flights, using the same process and logic described above.

Analysis of positional tuning at overlapping flight segments and goal-vector tuning

To further assess positional tuning of hippocampal neurons, we compared ROI tuning for pairs of flight paths with similar velocity profiles and durations that were either overlapping or non-overlapping in space (Supplementary Fig. 20a-g). 1D tuning profiles for each ROI were constructed by taking the mean of the deconvolved activity trace for each ROI aligned to takeoff for each flight path. Correlation scores were then calculated by taking the Pearson correlation of these ROI tuning profiles across either spatially similar flight paths (that are partially spatially overlapping) or spatially dissimilar flight paths (that are non-spatially overlapping). We then also calculated within flight-path tuning similarity by comparing the ROI tuning profiles between even/odd trials of a given flight path. Further, we re-calculated all correlation scores after restricting comparisons to the spatially overlapping portions of the two most similar flights (portions in which the within flight path positional variability is equal or greater than the across flight path variability).

To assess vectorial goal tuning of hippocampal neurons[63], we analyzed angle and distance tuning along different flight trajectories (Supplementary Fig. 21). 1D tuning profiles for each ROI were made by binning the deconvolved activity trace relative to either the distance to the goal location (using 50 cm bins) or by the angle between an animals' heading and the goal (using

18 degree bins) for each flight path and normalizing relative to their occurrence in behavior. These 1D distance and angle tuning profiles were then compared across flight paths by taking their pairwise Pearson correlation. Comparisons were made between (1) flight path pairs that terminated in the same goal location but did not overlap in space, as well as between (2) flight path pairs with highly similar trajectories where one path did not terminate in the same goal location. Suitable flight behavior for this analysis could be found in a subset of our dataset (334 ROI across 12 flight paths n = 4 bats). To create a null distribution for comparison, we re-computed the pairwise correlation scores after shuffling ROI identity.

The bat's position co-varies with angle and distance relative to the goal location during flight behavior which can lead to egocentric tuning misattribution (e.g., goal-vector tuning). Therefore, we considered what percentage of ROIs have similar, statistically significant distance tuning across different, non-spatially overlapping flight paths that end in the same goal location. First, a shuffled distribution was created for each ROI by rigidly time-shifting deconvolved neural activity during flight in a circular manner and recalculating goal-distance tuning. This procedure was repeated 10,000 times to create a null distribution for each ROI. We first identified a subset of ROIs where the peak of their distance tuning curves exceeded the 95th percentile compared to shuffle for both non-overlapping flight paths. ROIs were then deemed 'significantly tuned' if their tuning was also similar across flight paths (i.e., no statistical difference in tuning profiles via Wilcoxon Rank Sum test $p > 0.05$). Taking this approach, we found that 4.1% (14/335) of ROIs were significantly tuned to distance across different trajectories. We further did the same analysis for angle tuning and found that 3.9% of the ROIs (13/335) had the same tuning across different trajectories. Finally, we assessed the stability across days of this small subset of significantly tuned angle or distance to goal neurons and found no differences with the stability of the larger population ($p > 0.5$ Wilcoxon Rank Sum).

Decoding analysis

We devised a constrained naïve Bayesian decoder[98] to predict the flight path membership from neural activity, using the *fitcnb* function in Matlab (Supplementary Fig. 20h-i). A classifier was trained for each bat by taking the peak height and time of the deconvolved neural activity for all ROIs relative to takeoff. We only considered data from flight paths that contained at least 10 flights on any given session to avoid biases due to low samples (approximately five to six flight clusters per bat, for a total of n = 40 flight path clusters across all animals (n = 7)). We then predicted the flight path membership for all flight trajectories, relative to their actual groupings (i.e., ground truth). Decoding accuracy was determined using 10-fold cross validation by withholding flights randomly both within and across sessions.

2D rate map calculations and firing fields simulations

2D (X,Y) rate map projections were computed by binning the deconvolved firing rates for each ROI during flight periods in 10 x 10 cm^2 bins and collapsing across the Z dimension. We additionally calculated a 2D occupancy map of the time spent in each of these bins. Bins with an occupancy of three or less frames of imaging data (i.e., < 120 ms) were removed from both the rate and occupancy maps. Both rate and occupancy maps were then smoothed by Gaussian kernel with a radius of 1.5 bins. Next each firing rate map was divided by its corresponding occupancy map to create a normalized 2D rate map[28]. Finally, we calculated the 2D correlation of these rate maps across days and conditions.

Firing fields were simulated in a flight room sized space, with tuning characteristics that

were empirically derived from both our calcium imaging dataset and previously published literature of hippocampal tuning in bats[33]. Specifically, we used a field size between 700 – 1,300 cm^3 and a low spontaneous event probability that increases exponentially within the field. Fields were uniformly distributed in 3D space[33,62] and 50% were randomly given an azimuthal direction tuning between 90 – 180 degrees. These simulated firing fields are always present but will only be revealed if a field's pre-determined tuning criteria (place + heading) is met. This gives us an estimate of the detection limitations of traditional rate map analysis (binning spikes in 2D and normalizing by occupancy) given certain statistics of behavior. The behavioral data on each day were used to generate a surrogate dataset of 10,000 estimated tuning fields (obtained by convolving the bat's trajectories with the latent fields) and we then compared these simulated fields across days in the same manner as described above. 2D rate maps were constructed as described above, allowing us to calculate the 2D correlation of these simulated rate maps across days and conditions. For our simulated dataset, in order to exclude unobservable fields that would not be revealed by flight behavior (e.g., in an untraveled corner of the environment), comparisons were only made for simulated fields that had a total of 2.5x more simulated spikes than chance on at least one day. Our simulations were repeated 10,000 times to generate a distribution for comparison.

Statistical analysis

No formal methods were used to predetermine sample sizes; chosen sample sizes were similar to those used in the field. No randomization of experimental sessions was performed and no blinding to experimental conditions was implemented during the analysis. All statistical comparisons were performed using nonparametric tests (Wilcoxon Rank Sum test, Wilcoxon signed rank test, bootstrap, or randomization tests). Named tests were two-tailed unless otherwise stated. Where appropriate, multiple comparisons were controlled using Holm-Bonferroni step-down procedure.

Chapter 5: Supplementary Figures

5.1 Supplementary figures for Chapter 2

Supplementary Figure 1

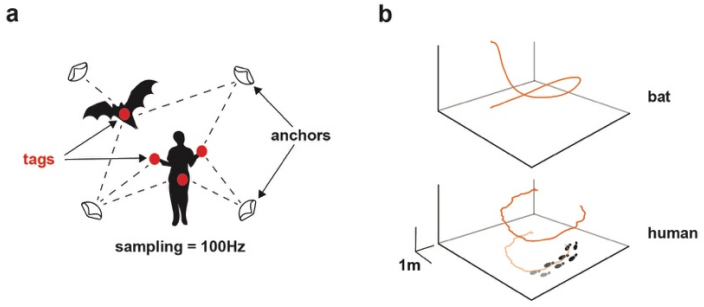

Supplementary Fig. 1 | Real-Time-Location-System for tracking the positions of bats and humans, and behavioral stability
a. Schematic of the Real-Time-Location-System. A set of static anchors communicate with a wireless tag (red dots) for 3D position localization. A total of eight tags are used in the experiment: one tag per bat, two tags are attached to the wrists of the two humans, and one tag is carried in each of the humans' right coat pockets. **b.** Example flight executed by a bat (*top*) and example traverse executed by a human (*bottom*) tracked with the RTLS system (Chapter 2 Supplementary Methods). For the human, a projection on the floor is also shown.

Supplementary Figure 2

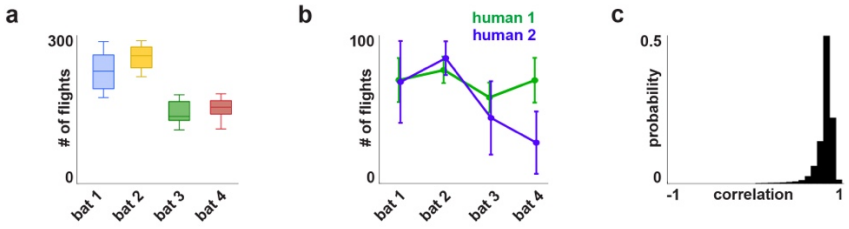

Supplementary Fig. 2 | Stability and reproducibility of bat flight behavior.
a. Distribution of the total number of flights executed by each bat over all analyzable recording sessions (n = 31 sessions). Box centers indicate the median number of flights, box bounds indicate 25th and 75th percentiles, error bars extend to minima and maxima. **b.** Average number of flights to human #1 (green) and human #2 (blue) for each bat over all analyzable recording sessions (n = 31 sessions). Error bars indicate standard deviation. **c.** Pearson correlation of the velocity profiles (concatenated x, y, and z velocity) between all pairs of flights of the same trajectory with sufficient flights to each human, across all analyzable sessions and bats (n = 37,521 flight pairs).

Supplementary Figure 3

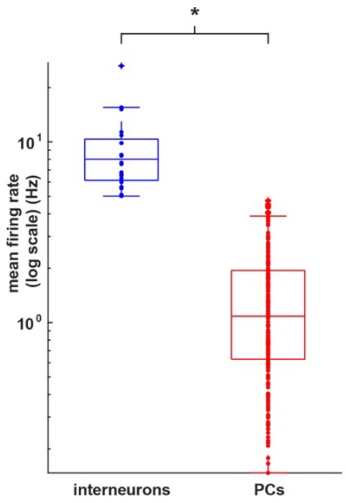

Supplementary Fig. 3 | Distribution of mean firing rates for putative interneurons v.s. principal units. A total of 24 putative interneurons were identified based on a threshold of > 5Hz mean firing rate over the course of the session. Blue boxplot indicates median firing rates (log scale) of interneurons (n = 24). Red boxplot indicates median firing rates (log scale) of putative principal cells (n = 251). Box bounds indicate 25th and 75th percentiles, error bars indicate minima and maxima, outliers indicated with a cross. Single asterisk indicates significant difference in firing rates between putative interneurons and principal cells by two-sided Wilcoxon rank sum test (p = 1.7×10^{-16}).

Supplementary Figure 4

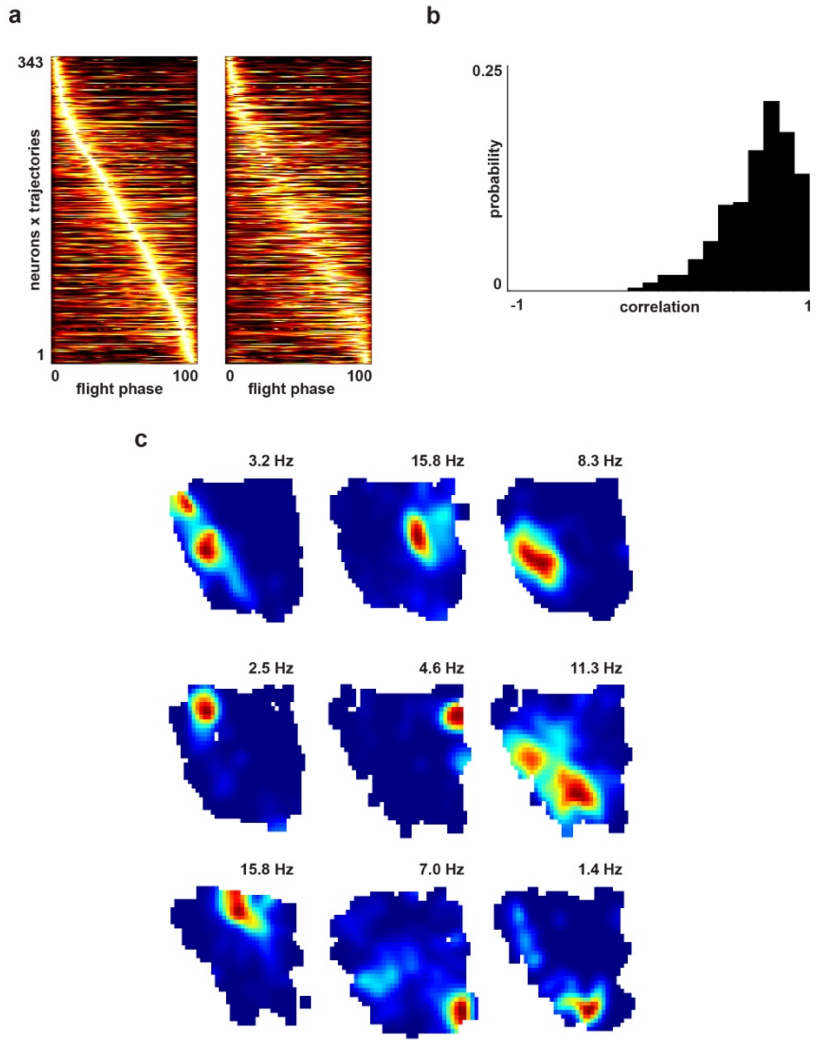

Supplementary Fig. 4 | Stability and selectivity of firing fields.
a. Left: Peak-normalized 1D rate maps for all spatially significant neurons x trajectories (even trials) sorted by peak activity over time (n = 343 neurons x trajectories). Right: 1D rate maps of all spatially significant neurons x trajectories (odd trials), sorted according to the even trials. **b.** Distribution of Spearman correlations between pairs of 1D rate maps constructed from even and odd trials, for each neuron x trajectory (n = 343 neuron x trajectory pairs). **c.** Representative 2D rate maps of significantly spatially selective neurons. Peak firing rate is indicated.

Supplementary Figure 5

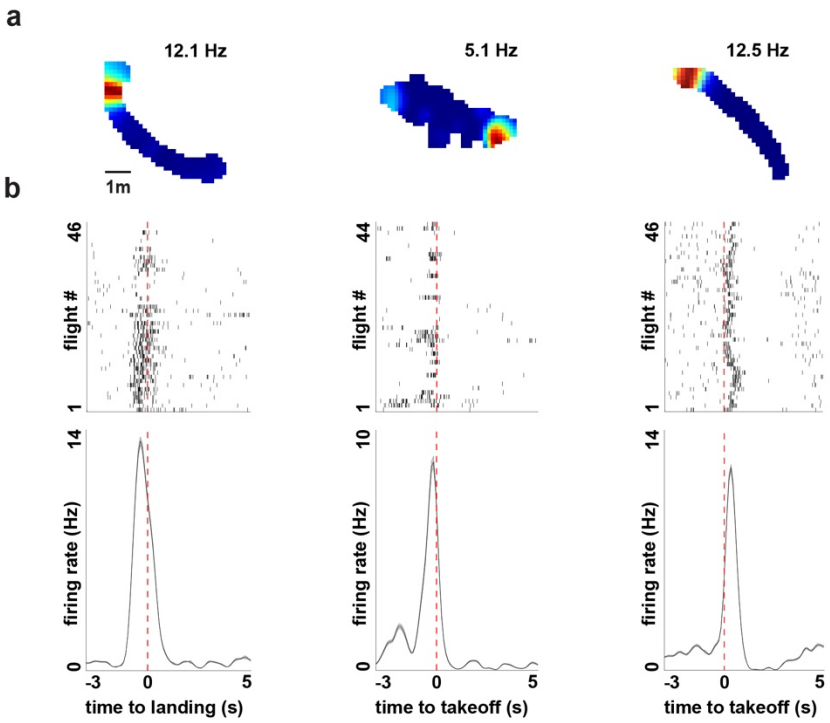

Supplementary Fig. 5 | Representative examples of trial-to-trial variability in the firing of spatially selective neurons.
a. Three example units. Same units as in Fig. 1d. First row shows 2D rate map constructed from all flights that share the same landing/takeoff location. Peak firing rate indicated. **b.** Raster plots (*top*) and PSTH (*bottom*) for all flights of that landing/takeoff location, aligned to landing (*left*), takeoff (*middle*), and takeoff (*right*) (red dotted line) and sorted by time of execution in the session. Shaded area of PSTH indicates standard error of the mean.

Supplementary Figure 6

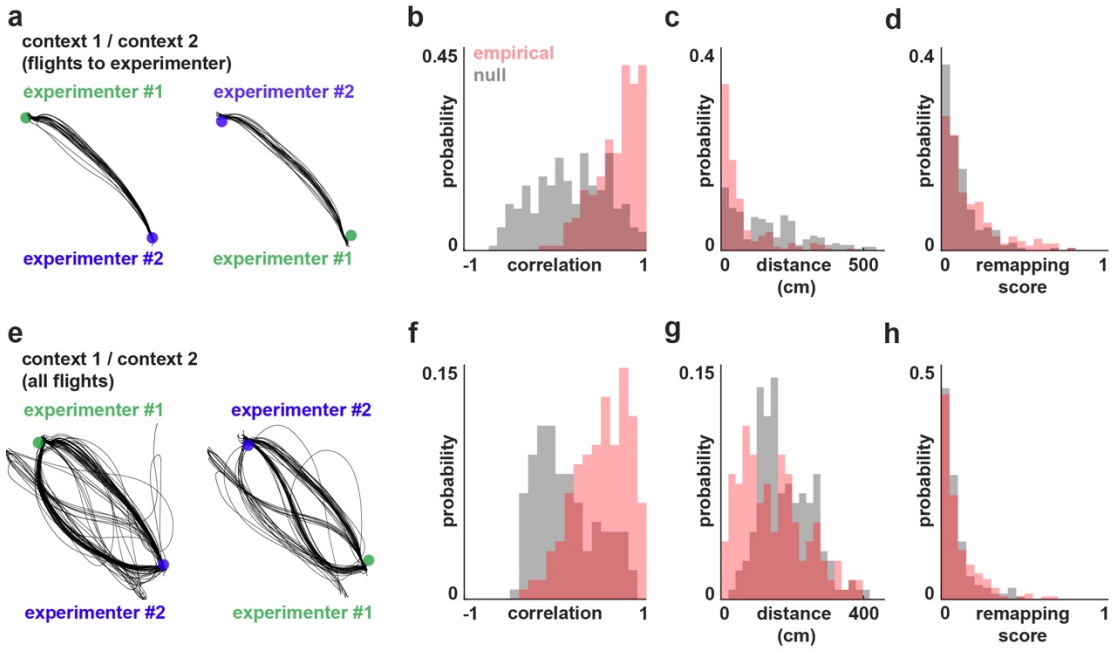

Supplementary Fig. 6 | Rate remapping on 1D and 2D rate maps.
a. Example flights along a single trajectory, during a single session, to experimenter #1 (shown in green; dot indicates mean human position during included flights) and experimenter #2 (shown in blue). **b.** Distribution of Pearson correlations between 1D linearized rate maps of trajectories to different human landing targets (n = 219 neurons x trajectories). Significant difference between empirical (red) and null (grey) distributions ($p = 6.0 \times 10^{-30}$, two-sided Wilcoxon signed rank test). **c.** Distribution of distance between peaks of 1D linearized rate maps of trajectories to different human landing targets (same neurons x trajectories as in subpanel '**b**'). Significant difference between empirical (red) and null (grey) distributions ($p = 1.2 \times 10^{-15}$, two-sided Wilcoxon signed rank test). **d.** Distribution of remapping scores for 1D linearized rate maps of trajectories to different human landing targets (same units x trajectories as in subpanel '**b**'). Significant difference between empirical (red) and null (grey) distributions ($p = 0.002$, two-sided Wilcoxon signed rank test). **e.** Example session of flights included in 2D rate maps for classical rate remapping analysis (included are all flights in a given context (Chapter 2 Supplementary Methods)). **f.** Distribution of Pearson correlations between 2D rate maps of different contexts (n = 162 neurons x contexts). Significant difference between empirical (red) and null (grey) distributions ($p = 5.0 \times 10^{-8}$, two-sided Wilcoxon signed rank test). **g.** Distribution of center of mass movements between rate maps of different contexts for same units as in subpanel '**f**'. Significant difference between empirical (red) and null (grey) distributions ($p = 4.7 \times 10^{-5}$, two-sided Wilcoxon signed rank test). **h.** Distribution of remapping scores between rate maps of different contexts for same units as in subpanel '**f**'. No significant difference between empirical (red) and null (grey) distributions ($p = 0.056$, two-sided Wilcoxon signed rank test).

Supplementary Figure 7

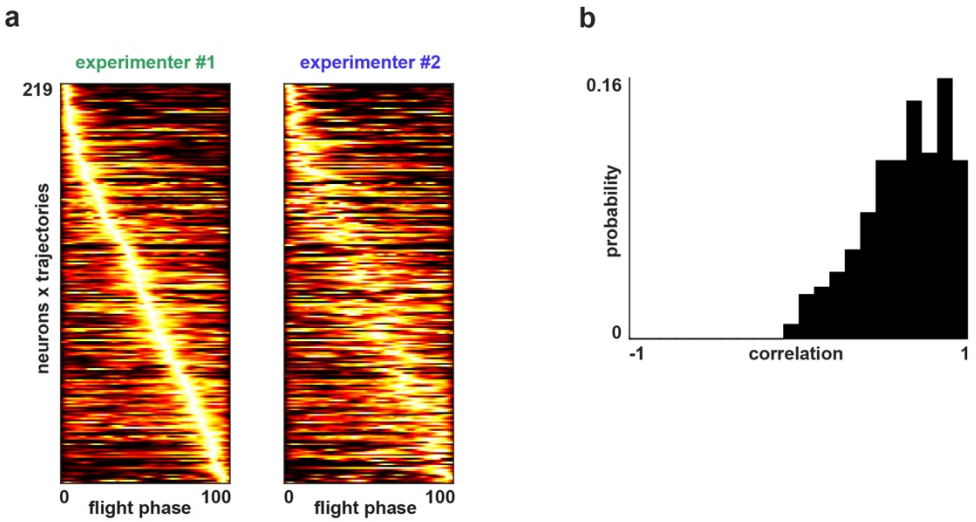

Supplementary Fig. 7 | Stability of place fields across human landing targets.
a. Left: Peak-normalized 1D rate maps for all spatially significant neurons x trajectories (trials to human landing target #1) sorted by peak activity over time (n = 219 neurons x trajectories). Right: 1D rate maps of all spatially significant neurons x trajectories (trials to human landing target #2), sorted according to the order of trials to human landing target #1. **b.** Distribution of Spearman correlations between pairs of 1D rate maps constructed from trials to human landing target #1 and #2, for each unit x trajectory (n = 219 neuron x trajectory pairs).

Supplementary Figure 8

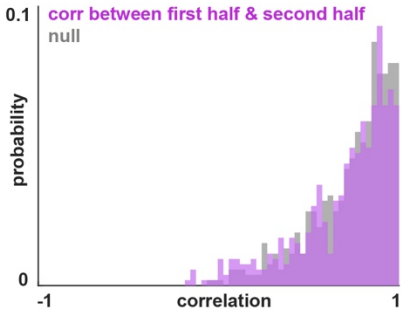

Supplementary Fig. 8 | Distribution of correlations between first and second halves of trajectories to each human.
Distribution of correlations between 1D linearized mean firing rates for first and second halves of a given trajectory to a given human (purple) versus the null (grey) (n = 527 analyzable neurons x trajectories). No significant difference between empirical and null distributions (p = 0.37, two-sample Kolmogorov-Smirnov test).

Supplementary Figure 9

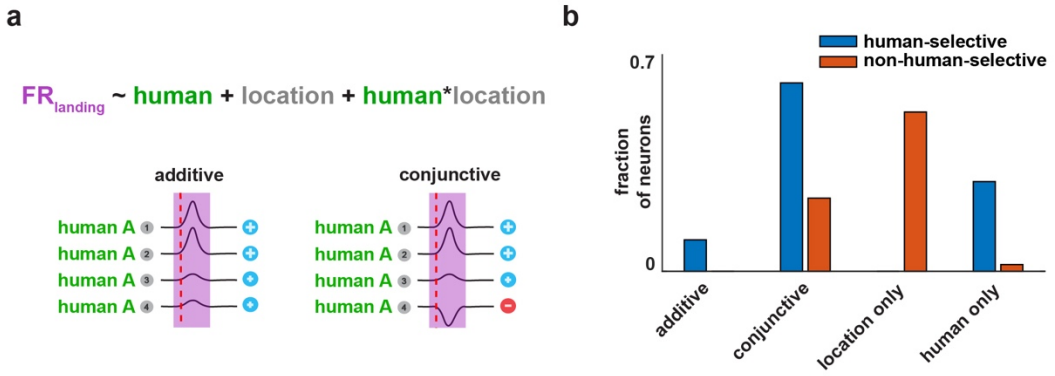

Supplementary Fig. 9 | Linear model predicting firing rate at landing based on human identity, location and their interaction.
a. Schematic of the linear model using one non-ordinal categorical variable for human identity, one non-ordinal categorical variable for landing location, and their interaction term (Chapter 2 Supplementary Methods). The grey circles with numbers represent possible locations, the red dotted line indicates landing, the purple boxes indicate the period used to calculate the firing rate, and the cartoon neural traces and corresponding plus and minus signs illustrate the difference in neural modulation that results from a strictly additive code versus a conjunctive code (Chapter 2 Supplementary Methods). In this cartoon example the neuron is modulated differently at the intersection of Human A and Location 4 than would be expected in an additive code. For brevity only one example experimenter (Human A) is included in this example. **b.** Model comparison was performed to determine if a given variable significantly (model comparison using anova test; $p < 0.05$) improved the prediction of a neuron's firing rate at landing (Chapter 2 Supplementary Methods). Neurons classified as 'additive' had significant Human and Location terms in model comparison, but not significant interaction terms. 'Conjunctive' neurons had significant Human and/or Location terms, as well as a significant interaction term. 'Human only' neurons had a significant Human term, but not significant Location or interaction terms. 'Location only' neurons had a significant Location term, but not significant Human or interaction terms. These categories of neurons were then split according to whether they modulated their activity depending on the human at takeoff/landing (via permutation test, Chapter 2 Supplementary Methods). Bar plot shows the split in the fraction of neurons for each category (n = 127 neurons). Note the fractions of additive, conjunctive, and human-only neurons that were also classified as modulated by the human (via permutation test) are larger than the fractions that were not modulated, and there are no neurons in the location-only category that were also classified as modulated by the human (via permutation test).

Supplementary Figure 10

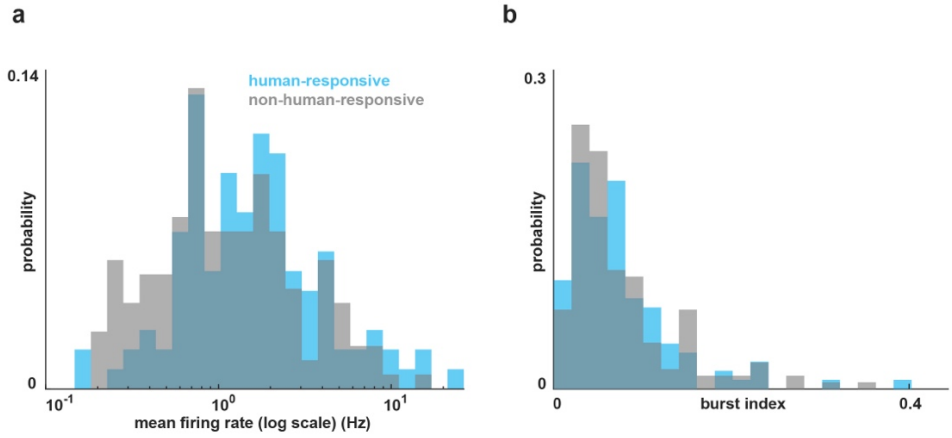

Supplementary Fig. 10 | Units properties for human-responsive v.s. non-human-responsive units.
a. Distribution of mean firing rates (log scale) of human responsive units (blue) (n = 117) and non-human-responsive units (grey) (n = 158). Significant difference between two distributions (p = 0.02, two-sample Kolmogorov-Smirnov test). **b.** Distribution of burst index of human responsive units and non-human-responsive units. No significant difference between the two distributions (p = 0.47, two-sample Kolmogorov-Smirnov test).

Supplementary Figure 11

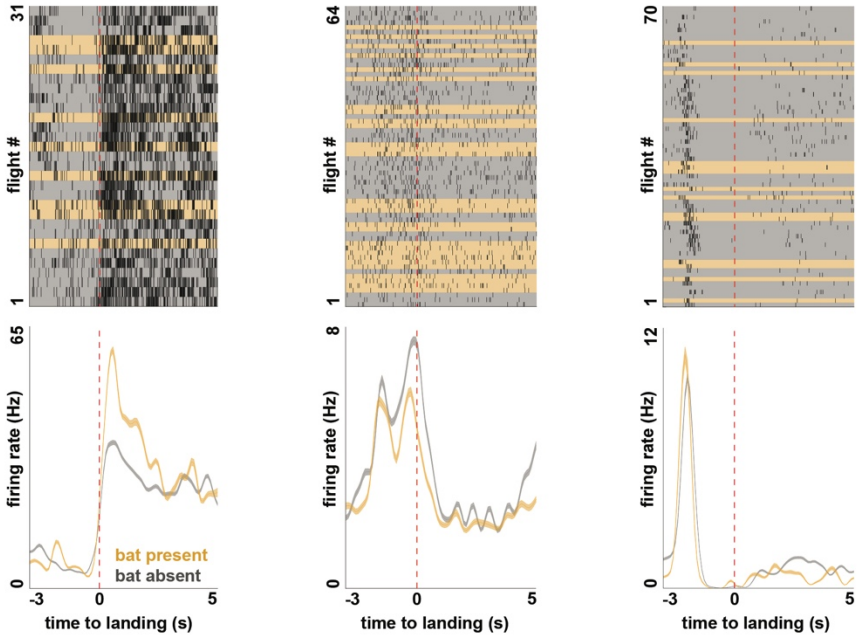

Supplementary Fig. 11 | Firing rate modulation during flight by the presence of another other bat at the landing location.
Shown are raster plots and PSTHs' for three example units that modulate (or not) their activity depending on whether there is another bat present at the landing target, aligned to landing (red dotted line). Colored rows on the raster plots indicate on which flights the other bat was present (orange) or absent (grey) at the landing target.

Colored lines on the PSTH plots indicate which PSTH was calculated from flights that landed on another conspecific (orange) or not (grey). Shaded lines indicate standard error of the mean.

Supplementary Figure 12

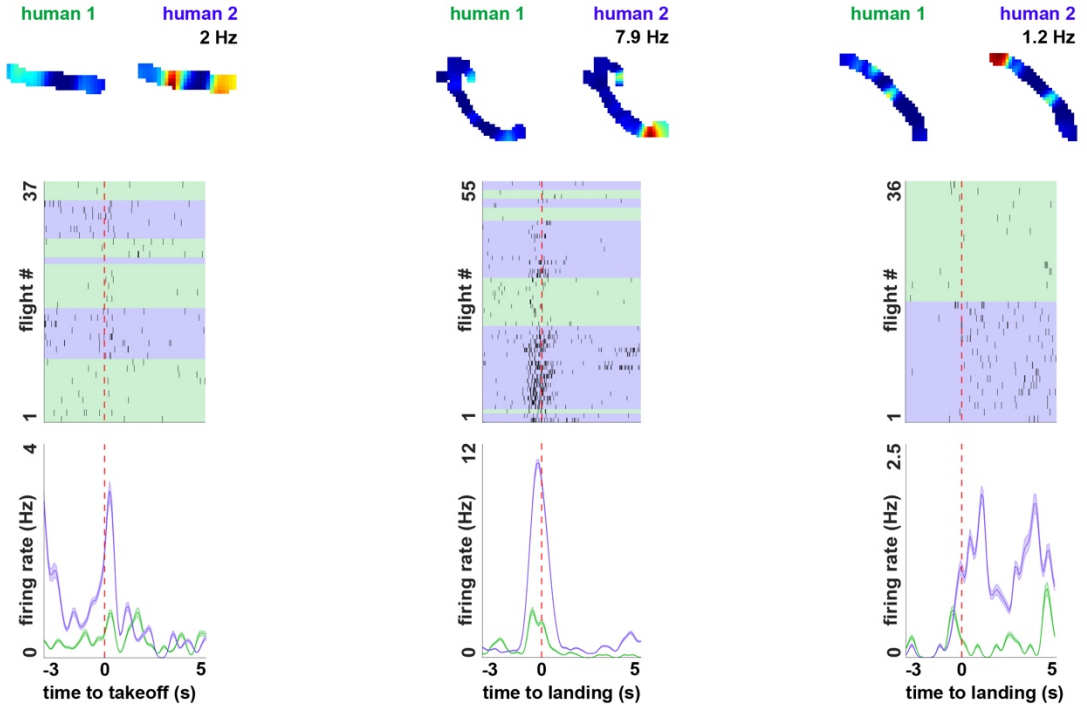

Supplementary Fig. 12 | Modulation of firing by human identity in the absence of another bat at the landing target.
Top row shows 2D rate maps of three example units that modulate their activity on flights to the same location but different humans. No flights included here had another bat present at landing. Second and third rows show raster plots and PSTH plots of the above units. Colored rows on the raster plots indicate which flights landed on human #1 (green) versus human #2 (blue). Colored lines on PSTH plots indicate which PSTH was calculated from flights that landed on human #1 (green) versus human #2 (blue). Shaded areas indicate standard error of the mean.

Supplementary Figure 13

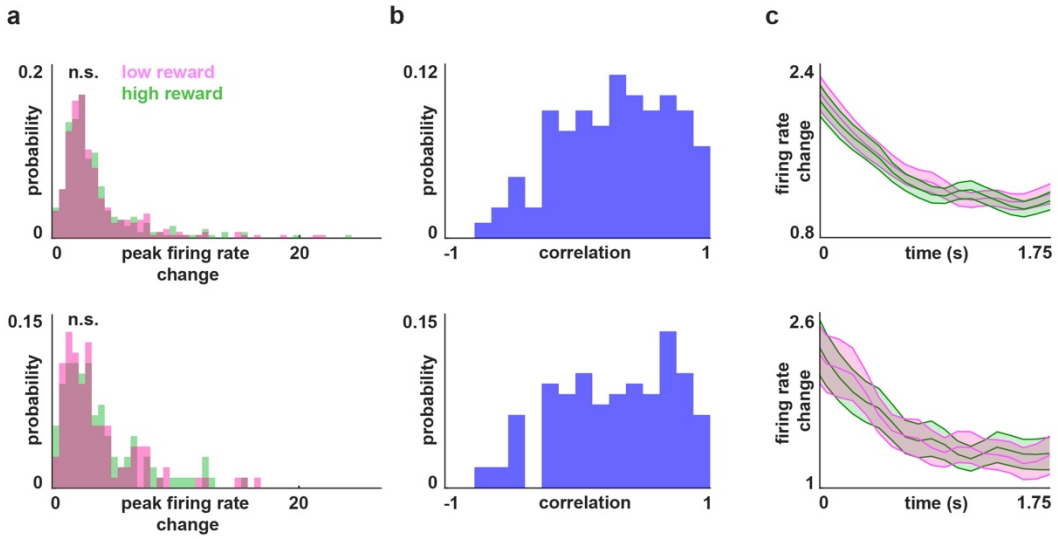

Supplementary Fig. 13 | Firing rate properties with unequal reward quantities.
a. (*top*) Distribution of peak firing rates in 2 s interval around landing for all analyzable neurons x landing locations in experiment #1, variant #2 – where different humans were stationary and provided different quantities of reward (Chapter 2 Supplementary Methods; n = 284 analyzable neurons x landing locations). No significant difference in distributions of peak firing rate change between high reward and low reward landings ($p = 0.94$, two-sided Wilcoxon signed rank test). (*bottom*) Same as the top but only including the neurons that were human-modulated (n = 111 neurons x landing locations). No significant difference in distributions of peak firing rate change between the different amounts of reward ($p = 0.77$, two-sided Wilcoxon signed rank test). **b.** (*top*) Spearman correlation between average firing rates around landing at high versus low reward locations for all analyzable neurons x landing locations, same as in subpanel '**a**'. (*bottom*) Same as the top but only including the neurons that were human-modulated, same as in the bottom of subpanel '**a**'. **c.** (*top*) Grand average firing rate changes after landing (around reward consumption) at high versus low reward locations (0 to +1.75 s, landing is 0). Shaded region indicates standard error. (*bottom*) Same as the top but only including the units that were human-modulated, same as in the bottom of subpanel '**a**'. Note that different rewards quantities by different experimenters were only provided on a subset of experiment #1 (humans are stationary while bats are flying) yet the modulation by human identity was observed irrespective of whether both humans provided different or similar reward quantities.

Supplementary Figure 14

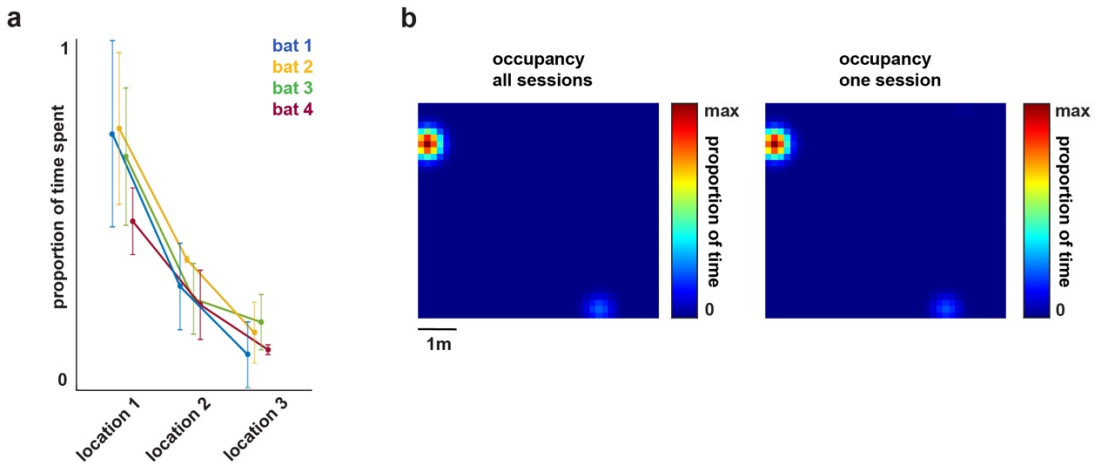

Supplementary Fig. 14 | Distribution of bats' rest locations during human traversals.
a. Mean proportion of total roost time each bat spent at self-selected rest locations during experiment #2 (human movement while bats were stationary), ordered from most preferred rest location to least preferred rest location. Shown are top three rest locations for each bat across all analyzable sessions (n = 31 sessions), which explain an average of 84% of the roost time. Error bars indicate standard deviation. **b.** Left: occupancy (color bar) of one bat's roosting locations across all sessions (n = 8 sessions) of experiment #2, smoothed with gaussian kernel (σ = 1.5 bins). Right: occupancy of one bat's roosting locations across a single example session of experiment #2, smoothed with gaussian kernel (σ = 1.5 bins).

Supplementary Figure 15

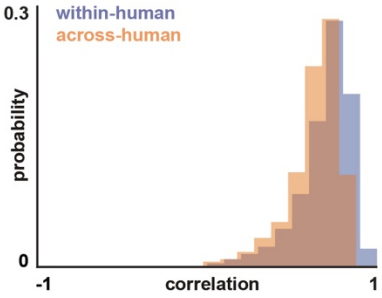

Supplementary Fig. 15 | Correlation of velocity profile for all human traverses.
Correlation of the velocity profile between all traverses of the same human (blue), and between all traverses across different humans (orange), for all sessions (n = 15 sessions; n = 5,904 traverse pairs within human, n = 5,829 traverse pairs across humans).

Supplementary Figure 16

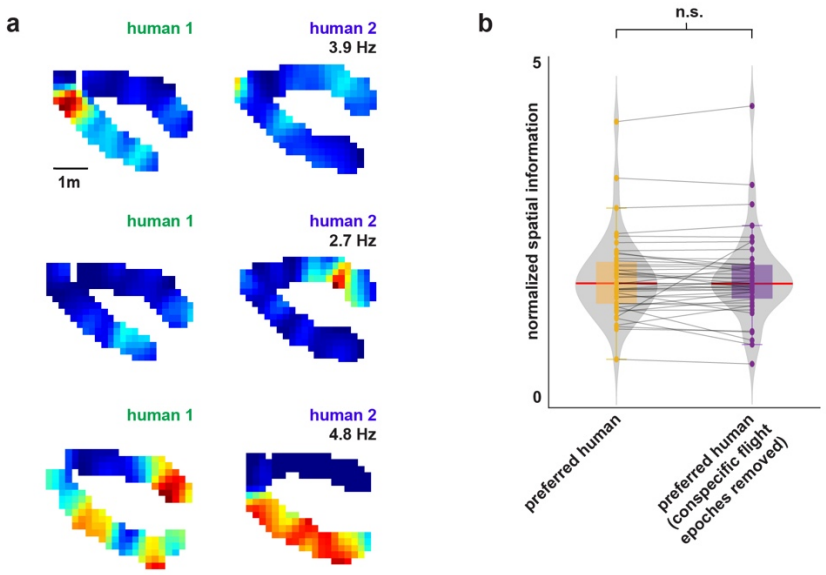

Supplementary Fig. 16 | Neurons with significant spatial information for human position and identity, excluding all bouts when the other bat was flying.
a. 2D rate maps of the same example neurons shown in Fig. 2d but excluding all times when the other bat was flying. **b.** For all neurons that carried significant spatial information for just one human, we compared the normalized spatial information (Chapter 2 Supplementary Methods) for the 'preferred' human (for which spatial information was significant) before (*left*) and after (*right*) removing all epochs when the conspecific bat was flying. Note that there was no significant difference (n.s.) between these two conditions (n = 43 neurons, two-sided Wilcoxon signed rank test, $p = 0.44$). Box plots indicate median normalized spatial information, box bounds indicate 25th and 75th percentiles, error bars extend to minima and maxima. Violin plots show kernel density estimation.

5.2 Supplementary figures for Chapter 3

Supplementary Figure 17

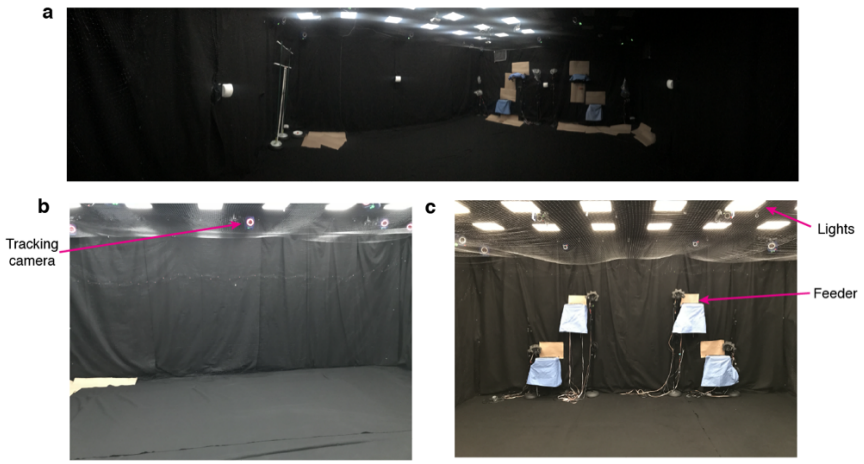

Supplementary Fig. 17 | The automated, human-free, flight room.
a Panoramic perspective of the automated flight room showing the feeders, adjustable ceiling lights, foam walls and motion tracking cameras. **b.** View towards one of the interior walls of the flight room. Motion tracking camera is indicated. **c.** View of the feeders. Note that the ceiling lights (white squares) and tracking system are visible on the ceiling for all images. The ceiling lights were set to specific illumination levels during the flight experiments (Chapter 3 Supplementary Methods) and are shown here at maximum brightness level for visualization purposes.

Supplementary Figure 18

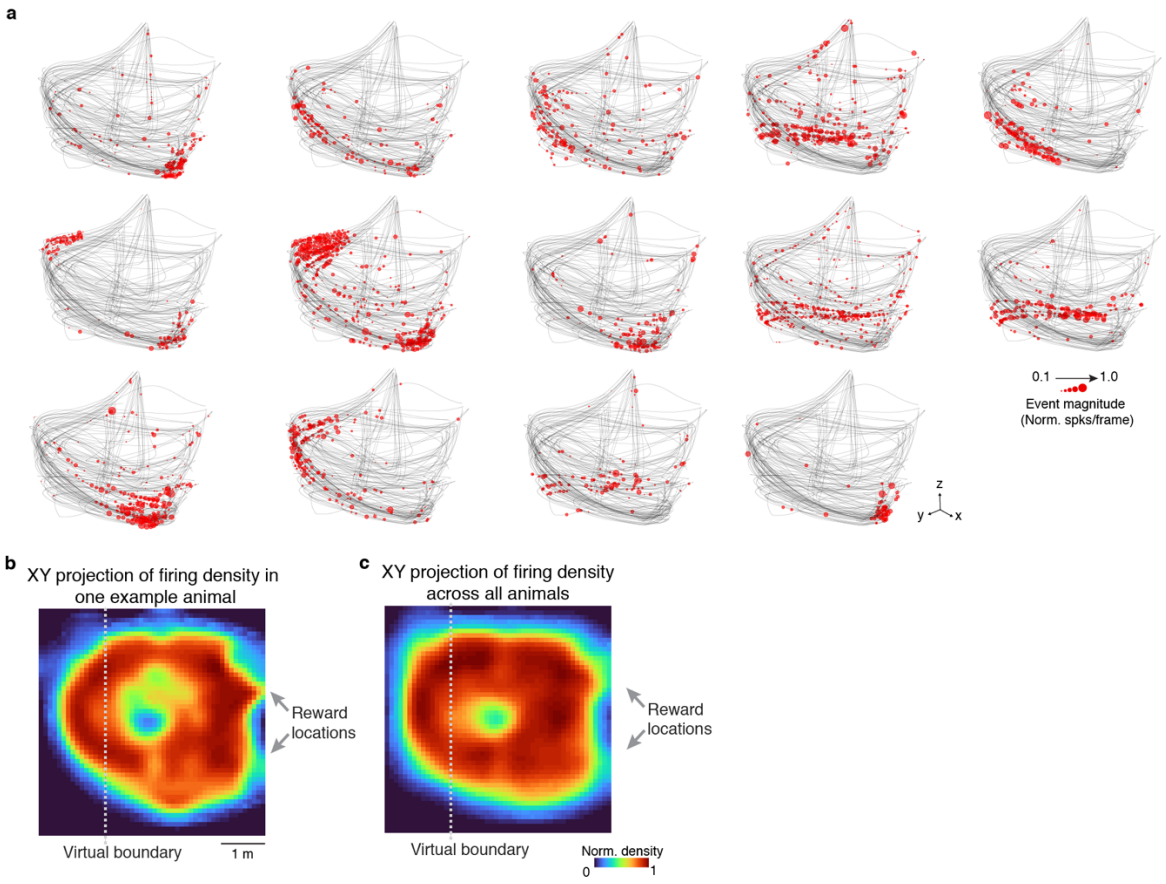

Supplementary Fig. 18 | Imaged hippocampal neurons are spatially selective and collectively span the available environment.
a. 14 simultaneously recorded ROIs during a single free-foraging session from one bat. Red dots represent estimated burst events superimposed on the flight trajectories (gray; Chapter 3 Supplementary Methods). The size of each dot indicates the relative size of the deconvolved burst event per imaging frame (per 33 ms bin; Chapter 3 Supplementary Methods). **b-c.** Firing density is not increased around the virtual boundary and the spatial activity recorded across neurons spans the available environment. **b.** Example spatial firing density for one animal. The virtual boundary that bats had to cross in order to rebait reward feeders is indicted by a dashed line. **c.** Spatial firing density of deconvolved neural activity (i.e., 'spikes') for all animals (n = 7). Reward locations are indicated. Images in b-c are displayed from a top-down (XY) perspective. There was no significant difference in firing density within 1m of this boundary vs. other locations in the room ($p > 0.5$ for all bats, two-tailed Wilcoxon Rank Sum).

Supplementary Figure 19

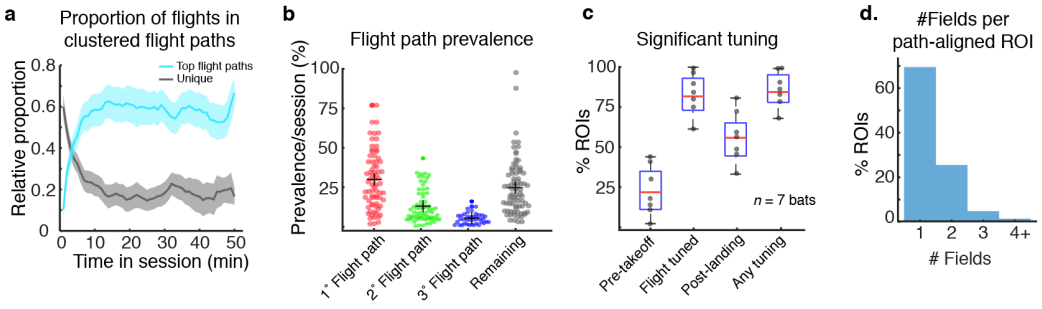

Supplementary Fig. 19 | Spatial behavior and hippocampal neural tuning along structured flight paths. **a-b.** Flights predominantly occur along a few highly repeated paths. **a.** After an initial period of exploration, a few common flight paths dominate the distribution of trajectories during the free-foraging session (n = 63 sessions from 7 bats). Blue and black lines are the mean proportion of flights over time for the three most common flight paths and the unique flight paths, respectively. Shading is 95% confidence interval around the mean. 73% of all recorded flights (3,472/4,731 flights from 7 bats) occur along repeated flight paths, 54% are flown across the three most common routes (1,877/3,472 flights from 7 bats) and 70% are in the top five most common routes (2,429/3,472 flights from 7 bats). **b.** Percentage of the top three flight paths and all other flights in each session across all animals, with the mean and SEM indicated. Each point is the prevalence of the top three flight paths on each session in which they occur. Points are jittered to ease visualization. **c.** Percentage of significantly tuned ROIs for all bats (n = 7; Chapter 3 Supplementary Methods). Each dot represents a single animal, the red line represents the mean for all seven bats, boxes are first and third quartiles and bars represent maximum and minimum across all bats. **d.** Percentage of ROIs with one or more fields per flight path (Chapter 3 Supplementary Methods).

Supplementary Figure 20

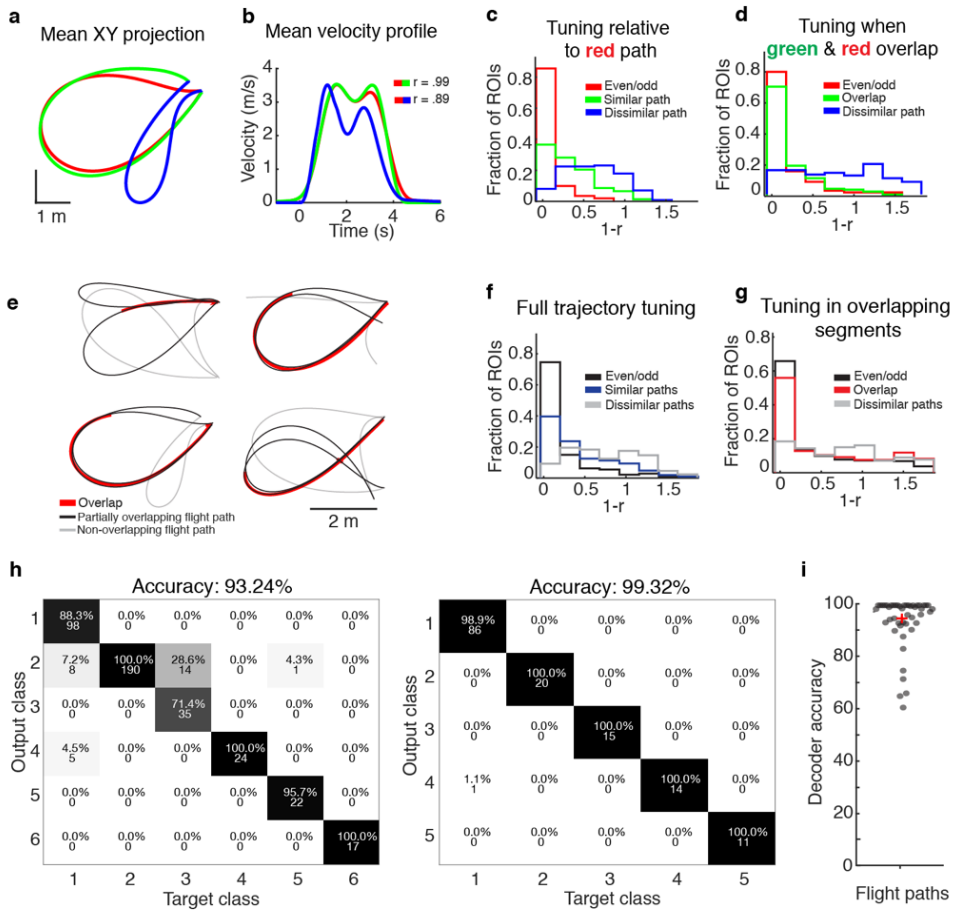

Supplementary Fig. 20 | Neural tuning is distinct for different trajectories but is highly similar in overlapping portions.
a. 2D projection (top-down view) of the mean flight path for the three most common flight paths for one bat. Note that the green and red trajectories are highly overlapping compared to the blue trajectory. **b.** Mean velocity profile for the same top three flight paths, with colors corresponding to those in (a). **c.** Distribution of correlation scores (shown here as 1-r for ease of comparison to Fig. 6 in the main text) for all ROIs, relative to the red flight path. The red distribution is calculated by comparing even/odd flights of the red flight path shown in (a). **d.** Same as (c) but only for the timeframe in which red and green flights overlap in space. **e.** Additional examples of overlapping flight paths. Overlapping paths are colored black and non-overlapping paths are gray. Overlapping regions are colored red. **f.** The black distribution is calculated by comparing neural tuning relative to even/odd flights that comprise a flight path; the blue distribution is the comparison of neural tuning across distinct flight paths that partially overlap in some segments. The gray distribution compares neural tuning across flight paths that are similar in duration but do not overlap in space. **g.** Same as (f) but only comparing neural activity for the timeframe in which similar flight paths overlap in space. The red distribution is the comparison of neural tuning during the overlapping portions of distinct flight paths and the gray distribution is a time matched control for trajectories that do not overlap in space. For (g-f), the black distribution is calculated by comparing neural tuning relative to even/odd flights that comprise a flight path; and red indicates a comparison of overlapping portions of distinct flight paths. **h-i.** Different flight paths can be accurately decoded using neural activity. **h.** Prediction accuracy for two bats (left and right confusion matrixes, respectively) where each class is a flight cluster. The percent accuracy and the number of classified flights is listed within each block (Chapter 3 Supplementary Methods). **i.** Decoder prediction accuracy for all bats and all flight paths with n > 10 flights. Points are jittered for ease of visualization.

Supplementary Figure 21

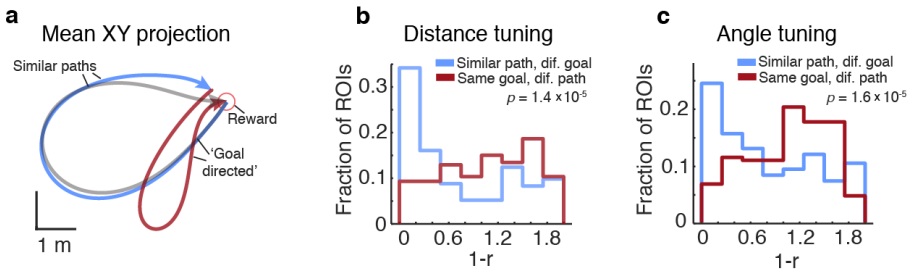

Supplementary Fig. 21 | Neural tuning is better explained by spatial rather than goal-vector tuning. **a.** Example of the analysis approach. Shown is a 2D projection (top-down view) of the mean flight paths for three flights of one bat. In this example, ROI distance and angle tuning for the gray flight path can be directly compared to a dissimilar flight path that terminates at the same goal location (in red, where shared angle/distance tuning is expected in the case of goal-vector tuning[63]) and to a similar flight path that ends in a different goal location (in blue, where goal-vector tuning is not expected, but shared angle/distance tuning might artefactually result from an overlap in spatial position). **b.** Distribution of correlation scores (shown here as 1-r for ease of comparison to Fig. 6 in the main text) for all ROIs binned by distance to goal (Chapter 3 Supplementary Methods) between pairs of similar flights (in blue) or pairs of dissimilar, goal terminating flight paths (in red). **c.** Same as (b) but binned by angle to the goal location. For (b-c), neural tuning is significantly more similar across pairs of overlapping flight paths (distance: $p = 1.4 \times 10^{-5}$ two-tailed Wilcoxon Rank Sum; angle: $p = 1.6 \times 10^{-5}$ two-tailed Wilcoxon Rank Sum); for dissimilar paths towards the same goal location, both goal and distance tuning distributions are not significantly different from what would be expected by chance (performing the same comparison after shuffling ROI identity, $p > 0.05$ two-tailed Wilcoxon Rank Sum). The percent of ROIs that have the same significant tuning across two non-spatially overlapping flights to the same goal location is 4.1% (14/335 ROIs) for distance and 3.9% (13/335 ROIs) for angle (Chapter 3 Supplementary Methods). Therefore, we did not observe pronounced goal-vector tuning independent of spatial position. This differs from a previous report in CA1 of flying bats[63] and could be due to increased false positive rates related to uncontrolled behavioral covariates in agreement with a recent report. (Carpenter, 2021 [https://www.abstractsonline.com/pp8/#!/10485/presentation/22193]).

Supplementary Figure 22

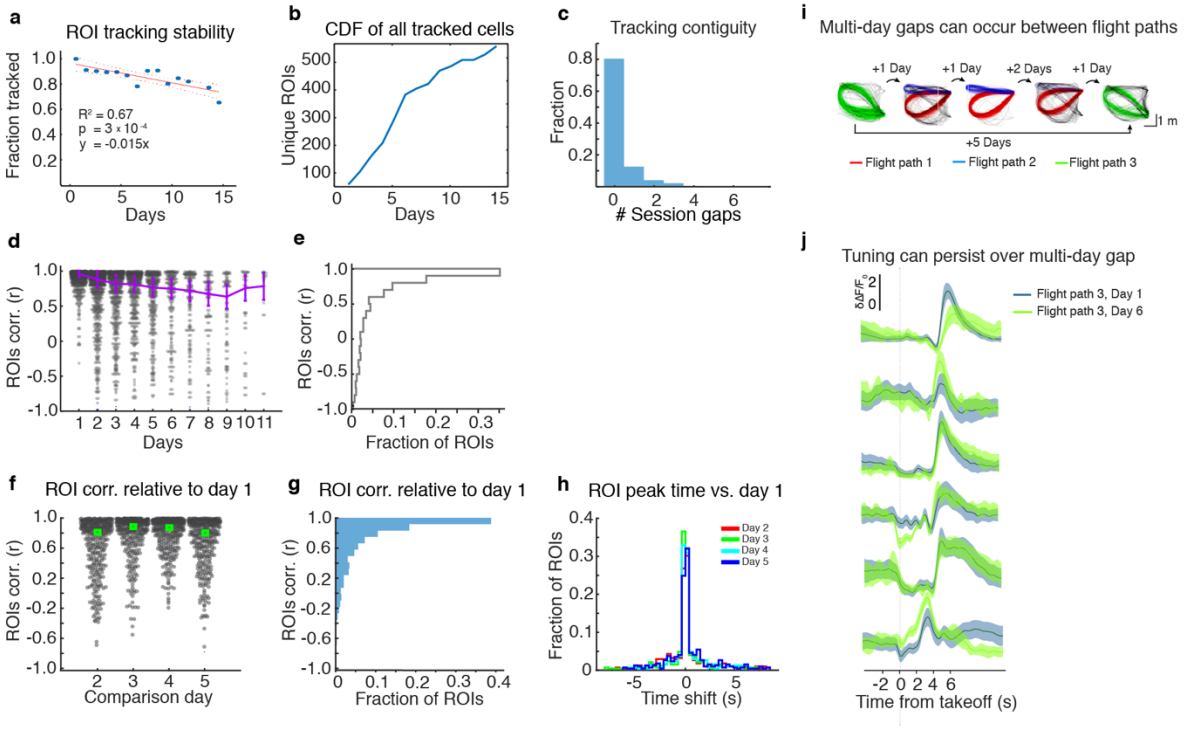

Supplementary Fig. 22 | Tuning stability for neurons tracked over days.
a. The fraction of ROIs that can be confidently tracked, under ideal conditions (no experimenter refocusing or noticeably large change in field of view) as a function of days. Each dot represents the fraction of ROIs tracked for all bats. Tracking loss occurred at a rate of about 2% of ROIs per day (linear fit, $R^2 = 0.67$, $p = 3\text{x}10^{-4}$). Dotted lines indicate 95% coefficient confidence intervals of the linear regression line in red. **b.** The cumulative distribution function (CDF) of unique ROIs that were included in the analysis, considering that some bats were tracked over longer intervals than others. **c.** Tracking contiguity showing the number of session gaps that exist between confidently tracked and aligned unique ROIs across days. **d.** Replotting the data in main text Fig. 4b, showing all underlying data points as a scatterplot. Error bars are 99% confidence intervals of the mean. Points are jittered for ease of visualization. Note that the number of ROI/flight-pair comparisons over days is decreasing (n = 914, 635, 490, 367, 208, 167, 117, 92, 45, 11). **e.** Tuning stability plot/histogram of all points in panel d (n = 3046 possible ROI/flight path pairs). Note the lack of a pronounced second peak where tuning stability equals 0, as would be expected if a prominent subset of neurons were to lose or gain tuning. **f.** Scatterplot distribution of ROI correlations compared to day '1' for the subset of consecutively tracked, flight path aligned ROIs (n = 360 ROIs). Green box indicates the distribution median. **g.** Histogram of correlation values for all points in panel (f). Note the lack of a pronounced second peak where tuning stability equals 0, as would be expected if a prominent subset of neurons were to lose or gain tuning. **h.** Distributions of the mean ROI peak times relative to the first day for all points in panel (f), separated by day (colors). **i-j.** CA1 tuning persists despite a multi-day gap in flight path behavior. **i.** The dominant three flight paths are colored in red, green and blue. Note the five-day interval between sessions with green flight paths. **j.** Six example ROI timeseries aligned to the green flight path on day 1 (dark green) and day 6 (light green). Shading is the standard deviation of the mean fluorescent time series. Note the high similarity in the ROIs' timeseries that persists after a multi-day gap during which this flight path was not flown.

Supplementary Figure 23

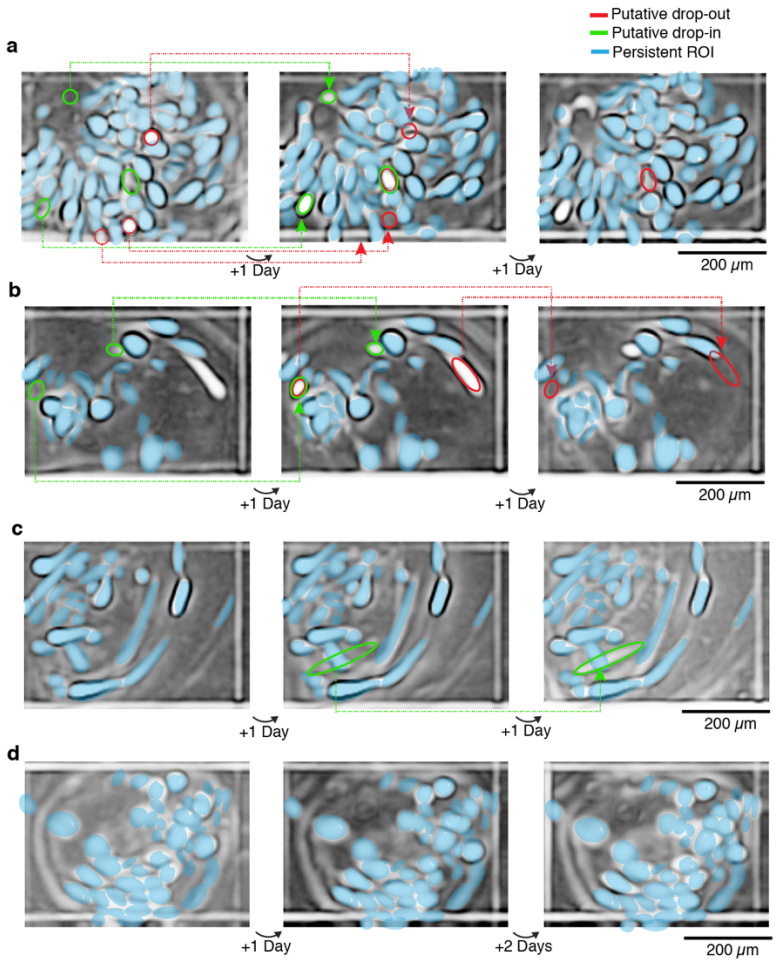

Supplementary Fig. 23 | Examples of abrupt, possibly biologically-driven, changes in neural participation over days.
Maximum intensity projections of adjacent flight sessions that show several compelling examples of sharp in focus ROIs that could be unambiguously identified on one day but are clearly absent in the proceeding or following imaging session. Several of these examples are less likely to be a result of a slow change in imaging plane across days, which explains the majority of our tracking loss (i.e., a slow change of ROI sharpness and intensity over consecutive sessions, as may be seen in some panels). Examples of abrupt changes in neural participation are sparse; panels **a-d** show different examples with panel (a) being the most obvious example found in our data set. Blue markers identify ROIs that are easily tracked on adjacent sessions. Red circles indicate an ROI that putatively 'drops-out' and green circles indicate an ROI that putatively 'drops-in.' Note that this phenomenon is uncommon and shown here to demonstrate the conservative approach: only 2.6% of clearly isolated ROIs identified on any given day show this effect (Chapter 3 Supplementary Methods).

Supplementary Figure 24

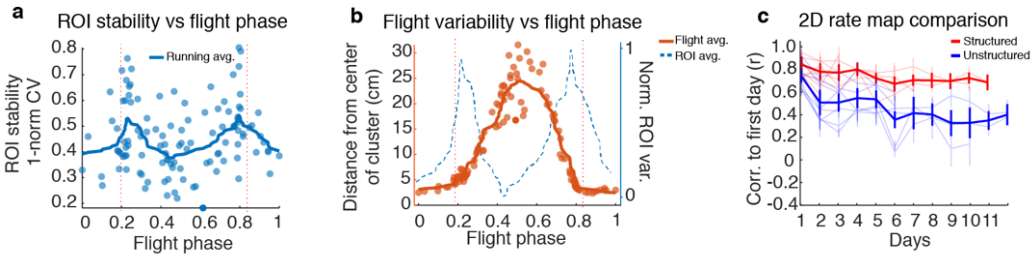

Supplementary Fig. 24 | ROI tuning stability and flight consistency.
a. Flight-to-flight consistency varies along the phase of flight (representative example for all ROIs tuned to the flight path shown in Fig 5a-b). Red dotted lines indicate takeoff and landing times. Each point represents a significantly tuned ROI's stability (i.e., one minus the normalized coefficient of variation [CV]) at the flight phase it is tuned to (determined by the peak of the mean flight-aligned deconvolved activity trace). The solid blue line is the running average of all points. **b.** Flight variability as a function of flight phase, sampled on the same interval as in (a). Flight variability was highest in the middle of the flight and lowest during the takeoff and landing. Y-axis units are the mean Euclidean distance of all individual flights from the center of the mean flight path. The blue dotted line is the same as the blue solid line from (a), normalized from 0-1. **c.** More structured behavior in freely flying bats results in the estimation of a more stable CA1 hippocampal responses over days. Longitudinal stability of hippocampal neural responses when considering either the most common structured flight path (i.e., the flight path comprised of the largest number of flights, in red) and all non-repeated (i.e., unstructured) flights in the same session (in blue) for n = 7 bats. Correlation is computed for 2D rate-maps relative to the first day of the experiment. Thin lines are different bats/flight paths and thick lines are the average across animals. Error bars represent 95% confidence intervals of the mean.

Supplementary Figure 25

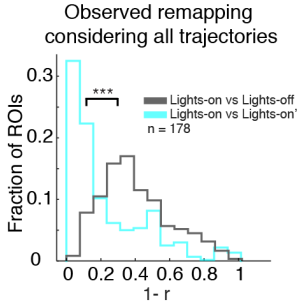

Supplementary Fig. 25 | Apparent sensory-based remapping when considering all flight trajectories before controlling for flight behavior variability across lights-on and lights-off conditions.
Shown is the distribution of 2D rate map correlation scores for all ROIs when considering all flight paths between either the two lights-on sessions (teal) or lights-on vs. lights-off conditions (gray). These distributions are significantly different (n = 178 ROIs, p = 7.04 x 10^{-55}, two-tailed Wilcoxon Rank Sum test).

Supplementary Figure 26

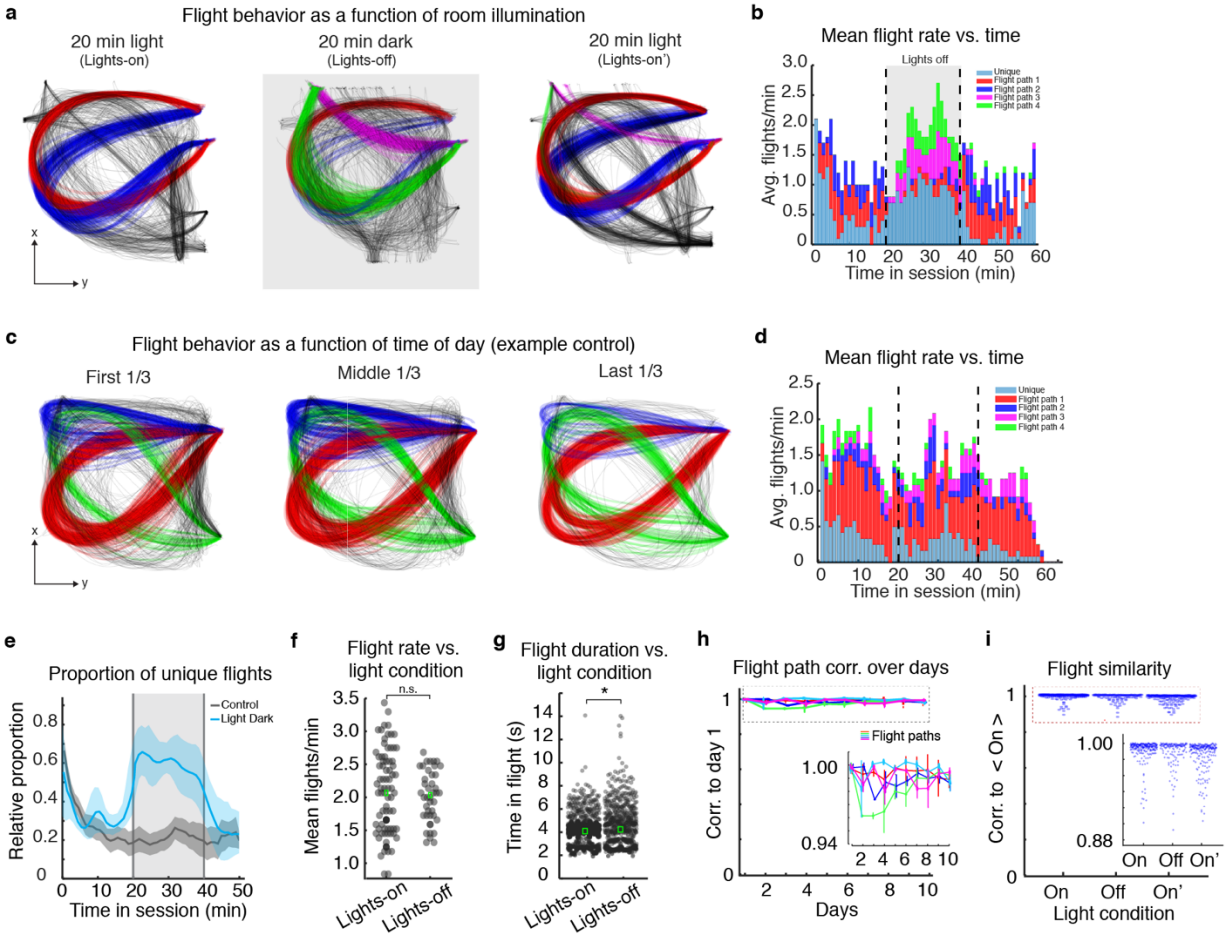

Supplementary Fig. 26 | Similarities and differences in flight behavior between the lights-on vs. lights-off cue conditions.

a. Aggregated flight paths that occurred across 10 consecutive days of experiments for one example bat, divided into successive lights-on, lights-off and lights-on' periods (ordered from left to right). Colored are the top four flight paths that persisted across both conditions. The red and blue flight paths occurred predominantly in lights-on and lights-on' sessions. The green and magenta paths occurred predominantly in the lights-off condition. **b.** Distribution of the occurrence of the four most prevalent flight paths, colored according to (a), during different phases of the experiment across lights-on and lights-off sessions. Flight preference changed dramatically during each period. **c.** Aggregated flight paths across 10 consecutive days for one representative bat divided into chronological thirds of each session where light levels were held constant. Shown are the top three clustered flight paths in red, blue and green. **d.** Distribution of the occurrence of the four most prevalent flight paths (colors) during different phases of the experiment across each third of 10 sessions. **e.** Proportion of unique (i.e., unstructured) flight paths increases on average in the lights-off cue condition (dark) compared to when the lights are kept on for the duration of the session. The blue line indicates the mean relative proportion of unique flights flown in the lights-on/off experiment. The dark gray line is the mean proportion of unstructured flights for bats where the light is kept on for the duration of the experiment. Shading for both plots represent 95% confidence intervals of the mean. **f.** The mean number of flights per minute is not significantly different in the light or dark conditions ($p > 0.05$ two-tailed Wilcoxon Rank Sum Test, n= 80 and 40 binned minutes in the lights-on and lights-off periods respectively). **g.** Flight duration as function of cue condition. Flight duration is significantly longer in the lights-off condition, ($p = 0.0038$, two-tailed Wilcoxon Rank Sum Test) although the effect size is small (i.e., the distributions are highly overlapping; n = 1567 and 746 flights in the lights-on and lights-off periods respectively). **h-i.** Across-day and across-condition behavioral stability

for the lights-on vs lights-off experiments. **h.** Average correlation of repeated paths relative to day one for each bat (n = 5 flight paths). Each color indicates a different flight path. Bars indicate 95% confidence intervals of the mean correlation on each day. **i.** Correlation values of shared flights to the mean of their flight path in the first lights-on period. Flights along the same path were not significantly different between the light and dark cue condition (p = 0.21 two-tailed Wilcoxon Rank Sum Test n = 268, 150, 267 flights for lights-on, lights-off and lights-on conditions respectively).

References

1. Tolman, E. C. Cognitive maps in rats and men. *Psychol Rev* **55**, 189–208 (1948).
2. O'Keefe, J. & Nadel, L. *The hippocampus as a cognitive map*. (Clarendon Press ; Oxford University Press, 1978).
3. Moser, E. I., Kropff, E. & Moser, M.-B. Place Cells, Grid Cells, and the Brain's Spatial Representation System. *Annu. Rev. Neurosci.* **31**, 69–89 (2008).
4. Davis, H., Taylor, A. A. & Norris, C. Preference for familiar humans by rats. *Psychon. Bull. Rev.* **4**, 118–120 (1997).
5. Van Driel, K. S. & Talling, J. C. Familiarity increases consistency in animal tests. *Behav. Brain Res.* **159**, 243–245 (2005).
6. Sorge, R. E. *et al.* Olfactory exposure to males, including men, causes stress and related analgesia in rodents. *Nat. Methods* **11**, 629–632 (2014).
7. Faraji, J. *et al.* Sex-specific stress and biobehavioral responses to human experimenters in rats. *Front. Neurosci.* **16**, (2022).
8. Georgiou, P. *et al.* Experimenters' sex modulates mouse behaviors and neural responses to ketamine via corticotropin releasing factor. *Nat. Neurosci.* **25**, 1191–1200 (2022).
9. Kaźmierowska, A. M. *et al.* Rats respond to aversive emotional arousal of human handlers with the activation of the basolateral and central amygdala. *Proc. Natl. Acad. Sci.* **120**, e2302655120 (2023).
10. Omer, D. B., Maimon, S. R., Las, L. & Ulanovsky, N. Social place-cells in the bat hippocampus. *Science* **359**, 218–224 (2018).
11. Danjo, T., Toyoizumi, T. & Fujisawa, S. Spatial representations of self and other in the hippocampus. *Science* **359**, 213–218 (2018).
12. Muller, R. U., Kubie, J. L. & Ranck, J. B. Spatial firing patterns of hippocampal complex-spike cells in a fixed environment. *J. Neurosci.* **7**, 1935–1950 (1987).
13. Mankin, E. A., Diehl, G. W., Sparks, F. T., Leutgeb, S. & Leutgeb, J. K. Hippocampal CA2 Activity Patterns Change over Time to a Larger Extent than between Spatial Contexts. *Neuron* **85**, 190–201 (2015).
14. Thompson, L. T. & Best, P. J. Long-term stability of the place-field activity of single units recorded from the dorsal hippocampus of freely behaving rats. *Brain Res.* **509**, 299–308 (1990).
15. Ziv, Y. *et al.* Long-term dynamics of CA1 hippocampal place codes. *Nat. Neurosci.* **16**, 264–6 (2013).
16. Rubin, A., Geva, N., Sheintuch, L. & Ziv, Y. Hippocampal ensemble dynamics timestamp events in long-term memory. *eLife* **4**, e12247 (2015).
17. Gonzalez, W. G., Zhang, H., Harutyunyan, A. & Lois, C. Persistence of neuronal representations through time and damage in the hippocampus. *Science* **365**, 821–825 (2019).

18. Hainmueller, T. & Bartos, M. Parallel emergence of stable and dynamic memory engrams in the hippocampus. *Nature* **558**, 292–296 (2018).
19. Levy, S. J., Kinsky, N. R., Mau, W., Sullivan, D. W. & Hasselmo, M. E. Hippocampal spatial memory representations in mice are heterogeneously stable. *Hippocampus* **31**, 244–260 (2021).
20. Kinsky, N. R. *et al.* Trajectory-modulated hippocampal neurons persist throughout memory-guided navigation. *Nat. Commun.* **11**, 2443 (2020).
21. O'Keefe, J. & Dostrovsky, J. The hippocampus as a spatial map. Preliminary evidence from unit activity in the freely-moving rat. *Brain Res.* **34**, 171–175 (1971).
22. Moser, E. I., Moser, M.-B. & McNaughton, B. L. Spatial representation in the hippocampal formation: a history. *Nat. Neurosci.* **20**, 1448–1464 (2017).
23. Grieves, R. M. & Jeffery, K. J. The representation of space in the brain. *Behav. Proc.* **135**, 113–131 (2017).
24. Ferbinteanu, J. & Shapiro, M. L. Prospective and retrospective memory coding in the hippocampus. *Neuron* **40**, 1227–1239 (2003).
25. Ainge, J. A., Tamosiunaite, M., Wörgötter, F. & Dudchenko, P. A. Hippocampal place cells encode intended destination, and not a discriminative stimulus, in a conditional T-maze task. *Hippocampus* **22**, 534–543 (2012).
26. Gothard, K. M., Skaggs, W. E., Moore, K. M. & McNaughton, B. L. Binding of hippocampal CA1 neural activity to multiple reference frames in a landmark-based navigation task. *J. Neurosci* **16**, 823–835 (1996).
27. Knierim, J. J. & Rao, G. Distal landmarks and hippocampal place cells: Effects of relative translation versus rotation. *Hippocampus* **13**, 604–617 (2003).
28. Geva-Sagiv, M., Romani, S., Las, L. & Ulanovsky, N. Hippocampal global remapping for different sensory modalities in flying bats. *Nat. Neurosci.* **19**, 952–958 (2016).
29. Ulanovsky, N. & Moss, C. F. Hippocampal cellular and network activity in freely moving echolocating bats. *Nat. Neurosci.* **10**, 224–233 (2007).
30. Sun, C., Yang, W., Martin, J. & Tonegawa, S. Hippocampal neurons represent events as transferable units of experience. *Nat. Neurosci.* **23**, 651–663 (2020).
31. Liberti, W. A., Schmid, T. A., Forli, A., Snyder, M. C. & Yartsev, M. M. A stable hippocampal code in freely flying bats. *Nature* **604**, 98–103 (2022).
32. Forli, A. & Yartsev, M. M. Hippocampal representation during collective spatial behaviour in bats. *Nature* **621**, 796–803 (2023).
33. Yartsev, M. M. & Ulanovsky, N. Representation of three-dimensional space in the hippocampus of flying bats. *Science* **340**, 367–372 (2013).
34. Sutherland, C. J. & Bilkey, D. K. Hippocampal coding of conspecific position. *Brain. Res.* **1745**, 146920 (2020).
35. Lang, S. D. J. & Farine, D. R. A multidimensional framework for studying social predation strategies. *Nat. Ecol. Evol.* **1**, 1230–1239 (2017).
36. Headland, T. N. & Greene, H. W. Hunter–gatherers and other primates as prey, predators, and competitors of snakes. *Proc. Natl. Acad. Sci.* **108**, E1470–E1474 (2011).
37. Bshary, R., Hohner, A., Ait-el-Djoudi, K. & Fricke, H. Interspecific communicative and coordinated hunting between groupers and giant moray eels in the red sea. *PLoS Biol* **4**, e431 (2006).

38. Detrain, C., Verheggen, F. J., Diez, L., Wathelet, B. & Haubruge, E. Aphid-ant mutualism: how honeydew sugars influence the behaviour of ant scouts. *Physiol. Entomol.* **35**, 168–174 (2010).
39. Hebshi, A., Duffy, D. & Hyrenbach, K. Associations between seabirds and subsurface predators around Oahu, Hawaii. *Aquat. Biol.* **19**, 89–98 (2008).
40. Yartsev, M. M. The emperor's new wardrobe: Rebalancing diversity of animal models in neuroscience research. *Science* **358**, 466–469 (2017).
41. Shriner, W. M. Yellow-bellied marmot and golden-mantled ground squirrel responses to heterospecific alarm calls. *Anim Behav* **55**, 529–536 (1998).
42. León, J., Thiriau, C., Crockford, C. & Zuberbühler, K. Comprehension of own and other species' alarm calls in sooty mangabey vocal development. *Behav. Ecol. Sociobiol.* **77**, 56 (2023).
43. Zhao, Z.-D. *et al.* Neurocircuitry of Predatory Hunting. *Neurosci. Bull.* **39**, 817–831 (2023).
44. Nougaret, S., Ferrucci, L. & Genovesio, A. Role of the social actor during social interaction and learning in human-monkey paradigms. *Neurosci. Biobehav. Rev.* **102**, 242–250 (2019).
45. Waran, N., McGreevy, P. & Casey, R. A. Training Methods and Horse Welfare. in *The Welfare of Horses* 151–180 (Springer Netherlands, Dordrecht).
46. Vieira de Castro, A. C., Araújo, Â., Fonseca, A. & Olsson, I. A. S. Improving dog training methods: Efficacy and efficiency of reward and mixed training methods. *PLoS One* **16**, e0247321 (2021).
47. Zhang, K., Yang, Z. & Başar, T. Multi-Agent Reinforcement Learning: A Selective Overview of Theories and Algorithms. in 321–384 (2021).
48. Stachenfeld, K. L., Botvinick, M. M. & Gershman, S. J. The hippocampus as a predictive map. *Nat. Neurosci.* **20**, 1643–1653 (2017).
49. Liu, W., Dong, L., Niu, D. & Sun, C. Efficient Exploration for Multi-Agent Reinforcement Learning via Transferable Successor Features. *IEEE/CAA Journal of Automatica Sinica* **9**, 1673–1686 (2022).
50. Piray, P. & Daw, N. D. Linear reinforcement learning in planning, grid fields, and cognitive control. *Nat. Commun.* **12**, 4942 (2021).
51. Mattar, M. G. & Daw, N. D. Prioritized memory access explains planning and hippocampal replay. *Nat. Neurosci.* **21**, 1609–1617 (2018).
52. Payne, H. L., Lynch, G. F. & Aronov, D. Neural representations of space in the hippocampus of a food-caching bird. *Science* **373**, 343–348 (2021).
53. Wohlgemuth, M. J., Yu, C. & Moss, C. F. 3D Hippocampal Place Field Dynamics in Free-Flying Echolocating Bats. *Front. Cell. Neurosci.* **12**, 270 (2018).
54. Geva-Sagiv, M., Las, L., Yovel, Y. & Ulanovsky, N. Spatial cognition in bats and rats: from sensory acquisition to multiscale maps and navigation. *Nat. Rev. Neurosci.* **16**, 94–108 (2015).
55. Harten, L., Katz, A., Goldshtein, A., Handel, M. & Yovel, Y. The ontogeny of a mammalian cognitive map in the real world. *Science (1979)* **369**, 194–197 (2020).
56. Toledo, S. *et al.* Cognitive map–based navigation in wild bats revealed by a new high-throughput tracking system. *Science* **369**, 188–193 (2020).
57. Tsoar, A. *et al.* Large-scale navigational map in a mammal. *Proc. Natl. Acad. Sci.* **108**, E718–E724 (2011).

58. Lütcke, H., Margolis, D. J. & Helmchen, F. Steady or changing? Long-term monitoring of neuronal population activity. *Trends Neurosci.* **36**, 375–84 (2013).
59. Clopath, C., Bonhoeffer, T., Hübener, M. & Rose, T. Variance and invariance of neuronal long-term representations. *Philos. Trans. R. Soc. B Biol. Sci.* **372**, 20160161 (2017).
60. Liberti, W. A., Perkins, L. N., Leman, D. P. & Gardner, T. J. An open source, wireless capable miniature microscope system. *J. Neural Eng.* **14**, 045001 (2017).
61. Genzel, D. & Yartsev, M. M. The fully automated bat (FAB) flight room: A human-free environment for studying navigation in flying bats and its initial application to the retrosplenial cortex. *J. Neurosci. Methods* **348**, 108970 (2021).
62. Dotson, N. M. & Yartsev, M. M. Nonlocal spatiotemporal representation in the hippocampus of freely flying bats. *Science* **373**, 242–247 (2021).
63. Sarel, A., Finkelstein, A., Las, L. & Ulanovsky, N. Vectorial representation of spatial goals in the hippocampus of bats. *Science* **355**, 176–180 (2017).
64. Mallory, C. S. & Giocomo, L. M. Heterogeneity in hippocampal place coding. *Curr. Opin. Neurobiol.* **49**, 158–167 (2018).
65. McNaughton, B. L., Barnes, C. A. & O'Keefe, J. The contributions of position, direction, and velocity to single unit activity in the hippocampus of freely-moving rats. *Exp Brain. Res.* **52**, (1983).
66. Wood, E. R., Dudchenko, P. A., Robitsek, R. J. & Eichenbaum, H. Hippocampal Neurons Encode Information about Different Types of Memory Episodes Occurring in the Same Location. *Neuron* **27**, 623–633 (2000).
67. Rubin, A., Yartsev, M. M. & Ulanovsky, N. Encoding of Head Direction by Hippocampal Place Cells in Bats. *J. Neurosci.* **34**, 1067–1080 (2014).
68. Kentros, C. G., Agnihotri, N. T., Streater, S., Hawkins, R. D. & Kandel, E. R. Increased Attention to Spatial Context Increases Both Place Field Stability and Spatial Memory. *Neuron* **42**, 283–295 (2004).
69. Muzzio, I. A. *et al.* Attention Enhances the Retrieval and Stability of Visuospatial and Olfactory Representations in the Dorsal Hippocampus. *PLoS Biol* **7**, e1000140 (2009).
70. Dupret, D., O'Neill, J., Pleydell-Bouverie, B. & Csicsvari, J. The reorganization and reactivation of hippocampal maps predict spatial memory performance. *Nat. Neurosci.* **13**, 995–1002 (2010).
71. Tchernichovski, O., Benjamini, Y. & Golani, I. The dynamics of long-term exploration in the rat. *Biol. Cybern.* **78**, 423–432 (1998).
72. Krakauer, J. W., Ghazanfar, A. A., Gomez-Marin, A., MacIver, M. A. & Poeppel, D. Neuroscience Needs Behavior: Correcting a Reductionist Bias. *Neuron* **93**, 480–490 (2017).
73. Widloski, J. & Foster, D. J. Flexible rerouting of hippocampal replay sequences around changing barriers in the absence of global place field remapping. *Neuron* **110**, 1547-1558.e8 (2022).
74. Mou, X., Pokhrel, A., Suresh, P. & Ji, D. Observational learning promotes hippocampal remote awake replay toward future reward locations. *Neuron* **110**, 891-902.e7 (2022).
75. Fang, C., Aronov, D., Abbott, L. & Mackevicius, E. L. Neural learning rules for generating flexible predictions and computing the successor representation. *elife* **12**, (2023).
76. Pachitariu, M., Sridhar, S., Pennington, J. & Stringer, C. Spike sorting with Kilosort4. *Nat. Methods* **21**, 914–921 (2024).

77. Rose, M. C., Styr, B., Schmid, T. A., Elie, J. E. & Yartsev, M. M. Cortical representation of group social communication in bats. *Science* **374**, eaba9584 (2023).
78. Zhang, W. & Yartsev, M. M. Correlated Neural Activity across the Brains of Socially Interacting Bats. *Cell* **178**, 413-428.e22 (2019).
79. Skaggs, W., McNaughton, B. & Gothard, K. An information-theoretic approach to deciphering the hippocampal code. *Adv. Neural Inf. Process. Syst.* **5** (1992).
80. Aronov, D., Nevers, R. & Tank, D. W. Mapping of a non-spatial dimension by the hippocampal–entorhinal circuit. *Nature* **543**, 719–722 (2017).
81. Leutgeb, S., Leutgeb, J. K., Barnes, C. A., Moser, E. I., McNaughton, B. L., Moser, M. B. Independent codes for spatial and episodic memory in hippocampal neuronal ensembles. *Science* **309**, 619-623 (2005).
82. Yovel, Y., Geva-Sagiv, M. & Ulanovsky, N. Click-based echolocation in bats: not so primitive after all. *J. Comp. Physiol. A* **197**, 515–530 (2011).
83. Holland, R. A., Waters, D. A. & Rayner, J. M. V. Echolocation signal structure in the Megachiropteran bat *Rousettus aegyptiacus* Geoffroy 1810. *J. Exp. Biol.* **207**, 4361–4369 (2004).
84. Lee, W.-J. *et al.* Tongue-driven sonar beam steering by a lingual-echolocating fruit bat. *PLOS Biol.* **15**, e2003148 (2017).
85. Danilovich, S. & Yovel, Y. Integrating vision and echolocation for navigation and perception in bats. *Sci. Adv.* **5**, (2019).
86. El-Mansi, A. A., Al-Kahtani, M. A., Al-Sayyad, K. M., Ahmed, E. A. & Gad, A. R. Visual adaptability and retinal characterization of the Egyptian fruit bat (Rousettus aegyptiacus, Pteropodidae): New insights into photoreceptors spatial distribution and melanosomal activity. *Micron* **137**, 102897 (2020).
87. Groot, A. D., Genderen, R. M. V., Coppens, J., Zeeuw, I. D. & Hoogland, T. M. NINscope : a versatile miniscope for multi-region circuit investigations. 1–32 (2019).
88. Shuman, T. *et al.* Breakdown of spatial coding and interneuron synchronization in epileptic mice. *Nat. Neurosci.* **23**, 229–238 (2020).
89. Cai, D. J. *et al.* A shared neural ensemble links distinct contextual memories encoded close in time. *Nature* **534**, 115–118 (2016).
90. Ghosh, K. K. *et al.* Miniaturized integration of a fluorescence microscope. *Nat. Methods* **8**, 871–878 (2011).
91. Kügler, S., Kilic, E. & Bähr, M. Human synapsin 1 gene promoter confers highly neuron-specific long-term transgene expression from an adenoviral vector in the adult rat brain depending on the transduced area. *Gene Ther.* **10**, 337–347 (2003).
92. Barchi, J. R., Knowles, J. M. & Simmons, J. A. Spatial memory and stereotypy of flight paths by big brown bats in cluttered surroundings. *J. Exp. Biol.* **216**, 1053–1063 (2013).
93. Guizar-Sicairos, M., Thurman, S. T. & Fienup, J. R. Efficient subpixel image registration algorithms. *Opt. Lett.* **33**, 156 (2008).
94. Huang, L. *et al.* Relationship between simultaneously recorded spiking activity and fluorescence signal in GCaMP6 transgenic mice. *elife* **10**, (2021).
95. Sheintuch, L. *et al.* Tracking the Same Neurons across Multiple Days in Ca2+ Imaging Data. *Cell Rep.* **21**, 1102–1115 (2017).
96. Zhou, P. *et al.* Efficient and accurate extraction of in vivo calcium signals from microendoscopic video data. *elife* **7**, (2018).

97. Pnevmatikakis, E. A. *et al.* Simultaneous Denoising, Deconvolution, and Demixing of Calcium Imaging Data. *Neuron* **89**, 285–299 (2016).
98. Zhang, K., Ginzburg, I., McNaughton, B. L. & Sejnowski, T. J. Interpreting Neuronal Population Activity by Reconstruction: Unified Framework With Application to Hippocampal Place Cells. *J. Neurophysiol.* **79**, 1017–1044 (1998).